

Discovery of carbon monoxide emission from five debris disks around young A-type stars

A. Moór¹, P. Ábrahám^{1, 2, 3}, Á. Kóspál^{1, 2, 4}, G. Cataldi⁵, A. M. Hughes⁶, S. Marino⁷, Q. Kral⁸, J. Milli⁹, and N. Pawellek^{3, 1}

¹ HUN-REN Research Centre for Astronomy and Earth Sciences, Konkoly Observatory, MTA Centre of Excellence, Konkoly-Thege Miklós út 15-17, H-1121 Budapest, Hungary
e-mail: moor.attila@csfk.org

² ELTE Eötvös Loránd University, Institute of Physics and Astronomy, Pázmány Péter sétány 1/A, H-1117 Budapest, Hungary

³ Department of Astrophysics, University of Vienna, Türkenschanzstraße 17, 1180, Vienna, Austria

⁴ Max-Planck-Institut für Astronomie, Königstuhl 17, D-69117 Heidelberg, Germany

⁵ National Astronomical Observatory of Japan, Osawa 2-21-1, Mitaka, Tokyo 181-8588, Japan

⁶ Astronomy Department and Van Vleck Observatory, Wesleyan University, 96 Foss Hill Drive, Middletown, CT 06459, USA

⁷ Department of Physics and Astronomy, University of Exeter, Stocker Road, Exeter, EX4 4QL, UK

⁸ LIRA, Observatoire de Paris, Université PSL, Sorbonne Université, Université Paris Cité, CY Cergy Paris Université, CNRS, 92190 Meudon, France

⁹ Univ. Grenoble Alpes, CNRS, IPAG, F-38000 Grenoble, France

Received September 15, 1996; accepted March 16, 1997

ABSTRACT

Context. Over the past fifteen years, surveys mainly at millimeter wavelengths have led to the discovery of ~ 20 gas-bearing debris disks, most of them surrounding young intermediate-mass stars. Exploring the properties and origin of this gas could be fundamental to better understanding the transition between the protoplanetary and debris disk phases, the evolution of icy planetesimal belts, and the formation of planetary atmospheres.

Aims. To expand the list of known CO-bearing debris disks and to improve our knowledge of the environmental conditions under which they can form, we targeted twelve dust-rich debris disks around young (< 50 Myr) intermediate-mass stars.

Methods. Using the ALMA 12-m Array we performed millimeter continuum and CO line observations to search for dust and gas and to measure their quantity and spatial distribution.

Results. We discovered CO gas in five disks. Two of them have a low CO content of a few times $10^{-5} M_{\oplus}$, similar to that of β Pic. The other three disks, however, are CO-rich with $M_{\text{CO}} > 10^{-3} M_{\oplus}$. By combining our results with those of other studies we concluded, in agreement with previous findings, that the detection rate of CO gas is significantly higher for disks around stars with $6.5 L_{\odot} < L_{*} < 21.9 L_{\odot}$ (\sim A8–A0 spectral type) than for disks around less luminous stars ($0.18 L_{\odot} < L_{*} < 6.4 L_{\odot}$, K7–A9). A comparison of the measured CO masses and the estimated mass loss rates of solids in disks with low CO content ($< 10^{-4} M_{\oplus}$) suggests that collisions may play a role in CO gas production in such systems. Interestingly, however, the estimated mass loss rates of CO-rich debris disks are not higher than those of systems with low CO content. In light of this finding, we speculate on what could lead to the formation of CO-rich debris disks.

Key words. circumstellar matter – submillimeter: planetary systems – techniques: interferometric

1. Introduction

Circumstellar debris dust rings, identified mainly based on their excess emission at infrared (IR) wavelengths, are common components of exoplanetary systems around main-sequence stars (Hughes et al. 2018). Their presence indicates that the system contains a belt or belts of planetesimals, whose erosion through mutual collisions, continuously replenishes the dust particles that are removed on short timescales by interactions with radiative forces (Wyatt 2008; Krivov 2010). Planetesimals are the

remnants of the epoch of planet formation that took place in gas-rich, massive protoplanetary disks in an earlier stage of evolution. If formed in a cold enough region far from the star, these small bodies can contain significant amounts of ice alongside rocky material. This means that the erosion processes in the debris disk phase can release not only dust particles, but also gases (Kral et al. 2017).

While the study of the dust component has been at the forefront of research since the discovery of the first debris disks

(Aumann et al. 1984), more extensive studies of the potential gaseous material were delayed until the 2010s due to the lack of sufficiently sensitive instruments, and were given a major boost mainly by the inauguration of the ALMA interferometer. While before 2010 only one debris disk with millimeter CO emission was identified (49 Cet, Zuckerman et al. 1995), the number of such systems has increased to ~ 20 in the last 15 years (Dent et al. 2014; Moór et al. 2011a, 2015a, 2017; Greaves et al. 2016; Lieman-Sifry et al. 2016; Marino et al. 2016; Matrà et al. 2017b, 2019; Kral et al. 2020b; Lovell et al. 2021b; Rebollido et al. 2022). Additional atomic gas components in emission have also been detected in some of these disks (Riviere-Marichalar et al. 2012, 2014; Roberge et al. 2013; Cataldi et al. 2018, 2020, 2023; Kral et al. 2019; Worthen et al. 2024; Samland et al. 2025). As high angular resolution ALMA images show, in most of these systems the bulk of the detected CO gas lies at radial distances of tens of au, more or less co-located with the outer planetesimal belts. The estimated CO masses show a large variety and their distribution implies two well distinguishable groups within the sample. Some of them contain an unexpectedly large amount of CO gas of $> 10^{-3} M_{\oplus}$, the most gas-rich ones have CO content comparable to that of protoplanetary disks (Moór et al. 2017). These so-called CO-rich disks are dust-rich as well ($f_d = L_{\text{disk}}/L_* > 5 \times 10^{-4}$), and all are found around A-type stars younger than 50 Myr. For the rest of the sample, the estimated CO gas content is $< 10^{-4} M_{\oplus}$. In addition to A-type stars, this subsample also includes later spectral type host stars, and although these systems are also typically young, two of them, Fomalhaut and η Crv, are substantially older than 50 Myr (Marino et al. 2018; Matrà et al. 2017b).

The detection of gas in exosolar systems is not limited to the outer planetary regions. Hot gas, derived from the sublimation of minor bodies approaching their host stars, has been detected as various absorption features in the spectra of dozens of stars including some that also host colder CO gas (e.g. Ferlet et al. 1987; Welsh & Montgomery 2013; Kiefer et al. 2014; Iglesias et al. 2018; Rebollido et al. 2020). This phenomenon is also most commonly associated with young early-type (A and B) stars (Rebollido et al. 2020; Bendahan-West et al. 2025).

It is not surprising that debris disks contain not only secondary dust but also gas, as planetesimals heated by mutual collisions, stellar irradiation, and possibly decay of radioactive nuclides can outgas their volatiles (Zuckerman et al. 2012; Kral et al. 2017; Davidsson 2021; Bonsor et al. 2023). Since the tenuous, optically thin dust material of these disks does not provide significant shielding, the stellar and interstellar UV photons reach the released molecules without any hindrance, causing their photodissociation. This limits the lifetime of even the most resistant molecule, CO, to ~ 120 yr (even considering only the interstellar UV field, Visser et al. 2009; Heays et al. 2017). Despite this very short lifetime, the amount of gas observed in low CO content disks ($< 10^{-4} M_{\oplus}$) can persist for a very long time, because the secondary gas production mechanisms mentioned above are able to ensure a sufficient rate of continuous replenishment (Kral et al. 2017; Marino et al. 2020a).

However, this is not the case for CO-rich systems, whose long-term survival - over millions or even tens of millions of years - would require unfeasibly high gas production rates. Their existence can be explained if there is some material in these systems that effectively shields the CO molecules from UV photons, thereby significantly prolonging their photodissociation lifetime. There are two proposals for the shielding, which can be attributed to very different gas origins. According to the shielded secondary gas scenario, assuming sufficiently high, but still real-

istic CO production rates, neutral carbon atoms produced by the photodissociation of mainly CO and CO₂ can become optically thick for the UV photons that threaten CO molecules. The increased lifetime allows the pile up of molecules to such an extent that, after a while, CO self-shielding can also begin to manifest, further reducing the photodissociation rate and thereby increasing the efficiency of the accumulation process (Kral et al. 2019; Moór et al. 2019; Marino et al. 2020a).

However, because of the young age of CO-rich systems, it cannot be excluded that their gas disk is predominantly composed of long-lived primordial gas, in which case the unseen H₂ molecules can provide efficient shielding for CO (Kóspál et al. 2013; Péricaud et al. 2017; Di Folco et al. 2020; Nakatani et al. 2021). Since dust is considered to be of secondary origin, such disks would be hybrid in nature. Indeed, recent theoretical results suggest that primordial disks, especially those around A stars, which are depleted in small dust particles (making far-UV photoevaporation less efficient), may persist for tens of millions of years (Nakatani et al. 2021, 2023; Ooyama et al. 2025). For the sake of completeness, we note that although the gas disk in this model is dominantly primordial, the observed CO could be partly or even largely of second generation origin.

The primordial and secondary gas scenarios predict very different gas compositions for CO-rich disks, with H₂ molecules being the dominant component in the former case, and CO molecules together with photodissociation end products (H, C, C⁺, and O) of the most common molecules released from icy bodies (mainly H₂O, CO, and CO₂, in analogy to Solar System comets) being the main constituents in the latter case. This may have interesting implications for the evolution of the planets in the system as they can accrete this gas material leading to significant changes in the composition of their atmospheres (Kral et al. 2020a).

At present, we do not know for sure which scenario might prevail for CO-rich disks, or what the ratio of primordial-to-secondary systems is within this sample. Constraining the amount of H₂ could clarify the situation, as little of this component is expected in secondary gas disks, but due to the difficulty of detecting this molecule in the typically low temperature environment of debris disks, this is not a viable option. Recent observations of C I in CO-rich debris disks have revealed less carbon gas than current secondary models would require for sufficient shielding (Cataldi et al. 2023; Brennan et al. 2024). Furthermore, it has been suggested that if the vertical mixing of the gas is sufficiently strong, the shielding efficiency of carbon gas may be substantially weaker than suggested by the model (Cataldi et al. 2020; Marino et al. 2022). These do not rule out a secondary origin, but indicate that the current model needs refinement. The development of the hybrid disk model is ongoing, but further improvements, for example the inclusion of thermochemistry, is needed to allow a direct comparison with observations (Ooyama et al. 2025).

Despite the observational and theoretical results achieved so far, we still do not clearly understand all aspects of the CO-rich, or alternatively the shielded, debris disk phenomenon. For further in-depth studies and to refine the proposed formation scenarios, it would be important to clarify the type of systems in which these disks can form, and under what environmental conditions. This requires not only detailed studies of known systems, but also the search for additional gas-rich debris disks in systems that may represent different environments than those we have explored so far. For example, the current sample may be biased, as previous surveys have typically focused on systems where earlier far-IR measurements have revealed the presence

of cold ($\lesssim 130$ – 140 K) debris disks (e.g. Moór et al. 2017). As a result, although population synthesis of secondary gas around A-type stars predicts that warmer planetesimal rings at 10–30 au can also form CO-rich shielded disks (Marino et al. 2020a), currently this cannot be tested due to the sparse observations of such targets.

With the motivation to discover new CO-rich debris disks and to better explore the possible environmental conditions favorable for their formation, we initiated an ALMA mini-survey to observe a sample of 12 carefully selected, dust-rich ($f_d > 5 \times 10^{-4}$), young debris disks (Sect. 2). Here we present the outcomes of the observations, in which we discovered five new CO-bearing debris disks including three CO-rich systems. After presenting the observations (Sect. 3) and analysing the continuum and line data (Sect. 4–5), we merge our results with existing literature data to investigate the detection rate of CO gas in dust-rich young debris disks and to compare the newly identified CO-bearing disks with the previously known ones. Using the new, unified sample, we investigate the possible origin of the CO gas by confronting the results with the predictions of both secondary and primary models (Sect. 6). For those systems from our sample whose continuum emission was spatially resolved, the position of the planetesimal belt can be estimated. Using this information we discuss the possible mechanisms for the dynamic excitation of these disks and whether the result of this analysis could indicate the presence of larger planet(s) in these systems (Sect. 6.6). The paper is closed with a summary of our results and conclusions.

2. Sample selection

In our survey, we focus on dust-rich debris disks around intermediate-mass stars with spectral types between F1 and B9.5. The choice of the lower limit of the spectral range was motivated by the fact that while previous observations well established that stars later than F1-type are unlikely to possess CO-rich debris disks (Lieman-Sifry et al. 2016; Moór et al. 2017), the F1–A7 spectral range has been poorly sampled, making the lower threshold for the existence of such disks unclear. Candidates were selected using data from the Gaia DR2 catalog (Gaia Collaboration et al. 2018; Lindegren et al. 2018). The spectral type was estimated based on the $B_p - R_p$ color index, using the updated online database¹ of stellar parameters of dwarf stars (Pecaut & Mamajek 2013). The $B_p - R_p$ colors were dereddened using data from the Stilism 3D database² (Capitanio et al. 2017; Lallement et al. 2018).

We selected stars located within 200 pc, thus extending the outer range with respect to previous surveys, which typically focused on objects within 150 pc (Moór et al. 2017). To ensure good observability from the ALMA site, we constrained declination between -78° and $+32^\circ$ and we removed those targets for which ALMA observations of sufficient quality are already available, and also those that are classified in the literature as Herbig Ae systems with protoplanetary disks. To identify systems showing excess at mid- and/or far-infrared (far-IR) wavelengths we used data from the point source catalogs of the *IRAS*, *AKARI*, *WISE*, *Spitzer*, and *Herschel* space telescopes (Moshir et al. 1990; Ishihara et al. 2010; Yamamura et al. 2010; Wright et al. 2010; Marton et al. 2017). We fitted the observed excess by one or two modified blackbody components to derive

the characteristic dust temperatures and fractional luminosities of the disks. In contrast to previous strategies, no criteria for dust temperature were applied in the target selection, but we restricted the sample to disks with $f_d > 5 \times 10^{-4}$, as this proved to be a good indicator of the presence of CO gas (e.g., Moór et al. 2017). After these steps we were left with a list of 28 dust-rich debris disks.

In the framework of our ALMA project (2021.1.01487.S, PI: A. Moór) observations were performed for 12 of the 28 targets³. Table 1 lists their main parameters including the fundamental stellar properties as well as the ages of these 12 systems. Appendix A describes in more detail how these parameters were obtained. The sample includes 11 A-type and 1 F-type stars, whose distances range between 93 and 188 pc. The ages of the selected systems range from 2.5 to 44 Myr. For 11 of the targets, there were already previous indications in the literature regarding their IR excess (see Table 1), but the disk of HD 152989 is a new discovery.

3. Observations and data reduction

All observations of our targets were carried out with the ALMA 12-m Array in Cycle 8. An important lesson from previous observations of CO-bearing debris disks is that not only ^{12}CO but even the ^{13}CO line can be optically thick. Thus, reliable CO mass estimate requires the measurement of ^{12}CO , ^{13}CO , and C^{18}O lines. Considering the typical CO excitation temperatures of 8–30 K, measured in known gas-bearing debris disks (Kóspál et al. 2013; Matrà et al. 2017a; Higuchi et al. 2020; Di Folco et al. 2020), the J=2–1 transition of CO is the best choice for gas detection, that is observable for all three isotopologs in Band 6. Therefore, we performed both our line and continuum measurements in this band. The correlator setup included six spectral windows. Two time division mode (TDM) spectral windows, each providing a total bandwidth of 2.0 GHz, split into 128 channels and centered at frequencies of 216.5 and 234 GHz, were used to probe the dust continuum. Three frequency division mode (FDM) spectral windows centered at 219.45, 220.399, and 230.538 GHz, each with 960 channels, were tuned to cover the C^{18}O , ^{13}CO , and ^{12}CO lines, respectively. The ^{12}CO line was observed with spectral resolution of 244.14 kHz (0.32 km s $^{-1}$), while for the other two lines, we applied the coarsest spectral resolution of 976.56 kHz (1.33 km s $^{-1}$). An additional FDM window – in the same baseband as the ^{12}CO measurement – centered at 232 GHz and having a bandwidth of 0.234 GHz and 960 channels was utilized to observe the continuum. Table 2 summarizes the main parameters of our observations including their dates, the number of antennas (N_{ant}), the baseline ranges of the array configurations (L_B), as well as the name of the sources used as flux, bandpass, and phase calibrators. Assuming a source with a Gaussian brightness distribution, with the shortest baseline length of 15 m, our observations have a maximum recoverable scale (MRS) of $\sim 8''$ at a 50% flux level, i.e. for a Gaussian source with such a full width at half maximum (FWHM), 50% of the true peak flux is expected to be lost (Wilner & Welch 1994, Appendix A, eq. A8). If we assume a uniform disk instead, we obtain an MRS of $8.9''$ for the same flux loss level (Wilner & Welch 1994, Appendix A, eq. A11).

All data sets were calibrated and flagged using the Common Astronomy Software Applications package (CASA;

¹ https://www.pas.rochester.edu/~emamajek/EEM_dwarf_UBVIJHK_colors_Teff.txt

² <https://stilism.obspm.fr>

³ Since our ALMA program received a C-grade priority, only a fraction of the requested observations were ultimately carried out.

Table 1: Overview of the sample.

Target name	SpT	Distance (pc)	v_{rad} (km s $^{-1}$)	Group	T_{eff} (K)	L_{\ast} (L $_{\odot}$)	M_{\ast} (M $_{\odot}$)	Age (Myr)	Mult.	Ref.	Label
HD 9985	A2	158.2 $^{+1.0}_{-1.0}$	+10.2 \pm 3.7	...	8900 \pm 200	14.18 \pm 0.61	1.88 \pm 0.04	44 $^{+31}_{-16}$...	3	1
HD 31305	A3	142.6 $^{+2.6}_{-2.7}$	-2.1 \pm 3.3	TAU	8600 \pm 170	16.95 \pm 0.64	1.97 $^{+0.06}_{-0.07}$	2.5 $^{+3.8}_{-1.5}$	Y	1	...
HD 112532	A2	119.5 $^{+0.4}_{-0.4}$	+12.4 \pm 4.4	LCC	8850 \pm 200	13.87 \pm 0.62	1.87 \pm 0.04	15 \pm 3	...	2	2
HD 131960	F1	146.6 $^{+0.5}_{-0.5}$	+2.58 \pm 1.47	UCL	7000 \pm 150	4.22 \pm 0.18	1.41 \pm 0.04	16 \pm 2	...	2	...
HD 141960	A9	142.5 $^{+0.5}_{-0.4}$	+0.90 \pm 0.72	US	7400 \pm 130	6.46 \pm 0.23	1.57 \pm 0.04	10 \pm 3	...	2	3
HD 144277	A3	143.4 $^{+0.6}_{-0.7}$	+1.72 \pm 0.49	UCL	8550 \pm 170	11.83 \pm 0.47	1.80 \pm 0.05	16 \pm 2	Y	2	...
HD 145101	A6	137.7 $^{+0.8}_{-0.9}$	-5.07 \pm 0.35	US	7950 \pm 200	18.58 \pm 0.68	1.89 $^{+0.14}_{-0.05}$	6.7 \pm 0.5	...	2	4
HD 152989	A6	114.9 $^{+0.4}_{-0.5}$	-7.49 \pm 0.80	UCL	7950 \pm 150	7.21 \pm 0.22	1.59 $^{+0.02}_{-0.03}$	16 \pm 2	Y	4	5
HD 155853	A4	136.1 $^{+0.7}_{-0.6}$	+0.39 \pm 1.51	UCL	8250 \pm 150	11.24 \pm 0.41	1.79 $^{+0.03}_{-0.04}$	16 \pm 2	...	2	6
HD 159595	A3	93.0 $^{+0.5}_{-0.2}$	-9.08 \pm 0.65	BPMG?	8450 \pm 140	10.58 \pm 0.35	1.75 \pm 0.03	21 $^{+4}_{-5}$...	2	7
HD 170116	A4	187.8 $^{+0.8}_{-0.8}$	-17.83 \pm 1.33	...	8250 \pm 250	11.63 \pm 0.60	1.79 \pm 0.04	31 $^{+9}_{-7}$...	3	8
HD 176497	A4	153.3 $^{+0.6}_{-0.6}$	-5.14 \pm 1.64	UCRA	8200 \pm 170	8.90 \pm 0.37	1.68 \pm 0.03	10	...	2	9

Notes. Distance estimates are taken from Bailer-Jones et al. (2021) using their geometric approach that is based only on the Gaia EDR3 parallaxes. Where available, the listed heliocentric radial velocity (v_{rad}) data were taken from the Gaia DR3 catalogue. For HD 9985 the quoted v_{rad} is from Gontcharov (2006), while for HD 31305 and HD 112532 we list the optimal radial velocities provided by the BANYAN Σ tool (Gagné et al. 2018), assuming that the star is indeed a member of the stellar association determined from astrometric data alone (Appendix A.3). For a more detailed description of how the listed stellar properties (T_{eff} , L_{\ast} , M_{\ast} , group membership, age, and multiplicity) are determined, see Appendix A. Abbreviations in the group column are as follows – COL: Columba moving group; LCC: Lower Centaurus Crux association; TAU: Taurus; UCRA: Upper CrA; UCL: Upper Centaurus Lupus association; US: Upper Scorpius association. Spectral type are derived from the obtained T_{eff} estimates using the updated online table^a of stellar parameters compiled by Pecaut & Mamajek (2013). The listed references show those studies in which the infrared excess of the stars was first reported: (1): Clark (1991); (2): Cotten & Song (2016); (3): McDonald et al. (2012); (4): this work. The last column shows which label we use to mark the given object in Figs. 7–9.

^a https://www.pas.rochester.edu/~emamajek/EEM_dwarf_UBVIJHK_colors_Teff.txt

Table 2: Observational parameters

Target	Obs. date	N _{ant}	L _B (m)	Calibrators	
				Flux/Bandpass	Phase
HD 9985	2022-09-01	46	15–784	J0238+1636	J0152+2207
HD 9985	2022-09-07	43	15–784	J0006-0623	J0112+2244
HD 31305	2022-08-08	42	15–1302	J0510+1800	J0438+3004
HD 112532	2022-09-03	43	15–784	J1427-4206	J1315-5334
HD 131960	2022-08-13	47	15–1302	J1517-2422	J1457-3539
HD 141960	2022-08-29	45	15–784	J1517-2422	J1554-2704
HD 141960	2022-09-04	46	15–784	J1517-2422	J1553-2422
HD 144277	2022-09-07	44	15–784	J1517-2422	J1610-3958
HD 145101	2022-08-28	43	15–909	J1517-2422	J1553-2422
HD 152989	2022-08-23	43	15–1302	J1517-2422	J1700-2610
HD 155853	2022-08-29	45	15–784	J1617-5848	J1717-3342
HD 155853	2022-08-30	45	15–784	J1617-5848	J1717-3342
HD 159595	2022-06-03	42	15–784	J1924-2914	J1717-3342
HD 170116	2022-09-01	46	15–784	J1924-2914	J1851+0035
HD 170116	2022-09-01	46	15–784	J1924-2914	J1851+0035
HD 170116	2022-09-04	45	15–784	J1924-2914	J1851+0035
HD 176497	2022-08-13	46	15–1302	J1924-2914	J1937-3958
HD 176497	2022-08-13	46	15–1302	J1924-2914	J1937-3958

McMullin et al. 2007) and the standard pipeline scripts provided by the ALMA Observatory. For data processing, we used the default CASA versions specified in the pipeline: for the observations of HD 9985, HD 144277, and HD 170116, which were performed during the last period of the project, the CASA software version 6.4.1.12 was used, while for the earlier measurements the version 6.2.1.7 was employed for data processing. No additional flagging was performed beyond the standard ALMA pipeline process. For objects that were observed at more than

one epoch (Table 2), the resulting measurement sets were concatenated using the CONCAT task. To ensure the relative weights between the different data sets are correct we recalculated the data weights with the CASA STATWT task. For the analysis of line emission in the FDM spectral windows, we used the UVCONTSUB routine to fit a first-order polynomial to the line-free regions (Sect. 5) in the uv space and subtracted the continuum from the obtained data.

4. Analysis of continuum data

4.1. Imaging

To construct continuum images, we used the TCLEAN task with the *multiscale* deconvolution algorithm, setting a list of scale sizes of 0 (point source), 5, 15, and 25 pixels (corresponding roughly to 1, 3, and 5 times the beam size). In this process, we used data from all of the spectral windows except for the channels where line emission was detected (Sect. 5). Figure 1 presents the obtained 1.33 mm continuum images showing the immediate (4" \times 4") environment of the targeted systems. The beam sizes range between 0.25 to 1.16" and have a mean value of 0.5". With the exception of HD 144277 and HD 176497, where natural weighting was used, all other images were compiled with Briggs weighting where the robust parameter was set to 0.5. The panels in the top three rows of the figure show those nine cases where we detected significant (peak $> 3\sigma$) signal at or near the position of the star. Six of them show clearly resolved disk structure, four with more edge-on (HD 152989, HD 155853, HD 170116, and HD 176497), and two with more face-on geometry (HD 9985 and HD 159595). The other three (HD 112532, HD 141960, and HD 145101) are only marginally resolved or point-like.

No significant continuum emission is found to be associated with HD 144277. This conclusion is not changed either by using natural weighting or by applying Gaussian tapers with size of 1" or 2" to look for possible extended emission. In the case of HD 131960, neither the Briggs nor the natural weighted images show any source. However, by applying a taper of 1", the resulting image (Fig. 1) shows a point source, located 0.02" from the position of the star, with a peak signal-to-noise ratio (S/N) of 2.6, just below the detection limit. Although this observation is treated as a non-detection, this result suggests that a future deeper measurement may reveal a faint extended disk around this star.

HD 31305 was not detected either, but at a separation of 0.59" from the star there is a very bright source, whose position coincides well with that of HD 31305 B, a K-type companion of our target (Appendix A.2). The latter object, probably a protoplanetary disk around the companion star, is discussed separately in Appendix C.

Table B.1 summarizes the relevant imaging properties, including the size and position angle of the synthesized beam and the achieved 1σ rms noise levels.

4.2. Modeling of the continuum emission

To model the spatial structure of the dust emission and to estimate the flux density of the disks at 1.33 mm, we used the `uv-MULTIFIT` tool developed by Martí-Vidal et al. (2014) to fit the observed visibilities. Only channels free of line emission were considered in the fits. For the six spatially well resolved sources (HD 9985, HD 152989, HD 155853, HD 159595, HD 170116, and HD 176497), two surface brightness profile models were tested: an elliptical Gaussian and an azimuthally symmetric Gaussian ring model. The former source model has six free parameters: the offsets with respect to the phase center in right ascension and declination, the flux density, the diameter of the major axis, the ratio of the sizes of the minor and major axes, and the position angle. In the latter model, there is an additional parameter which gives the width of the Gaussian describing surface brightness profile of the ring. In the modeling of the faint disk around HD 176497, this width parameter (the FWHM of the Gaussian) was fixed to be 0.7 of the ring radius (i.e. $W_{\text{disk}} = 0.7R_{\text{disk}}$, a typical value for debris disks Matrà et al. 2025). For the other five objects, the ring width was also a free parameter. To evaluate which of the best-fitting models obtained for the two different profile types has better quality, we used the Bayesian Information Criterion (BIC), which favored the Gaussian ring approach in all cases. We note that, motivated by the system's CO measurements, for HD 152989 we also developed a continuum disk model with two narrow rings (see Sect. 5.3). For the other three disks, we added a point source model to the profile types to be tested, and in the case of ring models the width parameter was always tied to the radius as $W_{\text{disk}} = 0.7R_{\text{disk}}$. Using the BIC for HD 112532, HD 141960, and HD 145101, we found the elliptical Gaussian, the Gaussian ring, and the point source models to be the best solution, respectively. The results are presented in Table 3.

We note that the derived parameters refer to the radial profile of the surface brightness and those of the surface density profile are slightly different. Considering that the 1.3 mm emission comes predominantly from large grains acting as blackbodies, the temperature dependence as a function of radius is $T(r) \propto 1/r^{0.5}$, and thus the peak of the surface density profile is found further away from the star. In addition, the width of the ring – defined as the half-width of the maximum of the obtained

profile – also changes slightly compared to that inferred from the analysis of the surface brightness profile. However, in our cases these deviations are always smaller than the 1σ uncertainty of the estimated R_{disk} and W_{disk} parameters.

Of the non-detected objects, for HD 131960 and HD 144277, their SEDs imply the presence of copious amount of warm (150–180 K, Appendix A.5) circumstellar dust. However, the available measurements limited to wavelengths shortward of 25 μm do not allow us to rule out that colder grains, located further away from the star, are also present in these systems. Taking this into account, for these objects we provide 3σ upper limits for flux density derived from the noise measured in their 1" tapered imaging, where the achieved beam size corresponds to 160–170 au (we assumed that if they had a disk at all, then it would be a point source at this spatial resolution). Although the SED of HD 31305 is much better sampled, with both good quality mid- and far-infrared data available, it is likely that a significant fraction or even all of the observed excess of the system actually comes from the disk around the late-type companion, HD 31305 B, which is probably protoplanetary in nature (Appendix C). Due to the presence of the nearby stellar companion (whose projected separation is ~ 70 au), if there is a disk around HD 31305A at all, it may be strongly truncated, thus in this case the 3σ upper limit on the flux density was derived from the noise of the Briggs weighted map that has a spatial resolution of ~ 50 au. The obtained flux density upper limits are also shown in Table 3.

4.3. Dust masses

Using the obtained 1.33 mm flux densities ($F_{1.33\text{mm}}$) we estimated the mass of grains smaller than a few millimeters. Since the thermal emission of debris disks at millimeter wavelengths is optically thin, the dust mass can be estimated as

$$M_{\text{dust}} = \frac{F_{1.33\text{mm}} d^2}{B_{\nu}(T_{\text{BB}}) \kappa_{\nu}}, \quad (1)$$

where d is the distance, $B_{\nu}(T_{\text{BB}})$ is the Planck function at 1.33 mm for a temperature of T_{BB} , and κ_{ν} is the dust opacity at the given frequency. For the dust opacity we adopt $\kappa_{\nu} = 2.3 \text{ cm}^2 \text{ g}^{-1}$ (Andrews et al. 2013). At such long wavelengths the radiation is dominated by large grains ($\gtrsim 100 \mu\text{m}$) which act as blackbodies. For spatially resolved disks, the characteristic blackbody temperature of large grains has been estimated using the derived disk radii (Table 3) and the luminosity of the star (Table 1), by applying the following formula: $T_{\text{BB}}(\text{K}) = 278 (L_*/L_{\odot})^{0.25} (R_{\text{disk}}/\text{au})^{-0.5}$. The T_{BB} values obtained this way range from 37 K (for HD 170116) to 90 K (for HD 112532). For HD 145101, we only have an upper limit on the disk size. From this, we can calculate a lower limit of ~ 100 K on T_{BB} , while the temperature estimate from fitting its SED (163 K, Table A.2) provides an upper limit on this parameter. From this, two dust mass estimates can be calculated, the average of which is taken as the final result. For HD 131960 and HD 144277, we only have upper limits on the millimeter flux. As already mentioned above, although their SED analysis indicates only dust with temperatures of 150–180 K, the presence of a colder disk component cannot be excluded, so we have assumed $T_{\text{BB}} = 60$ K in the calculations, which is the average of the dust temperature estimates we obtained for the 8 spatially resolved disks. If there is any disk around HD 31305 A, it is probably limited in size to the gravitational influence of its nearby companion star. Therefore, in estimating a dust mass upper limit in this case, we have assumed a

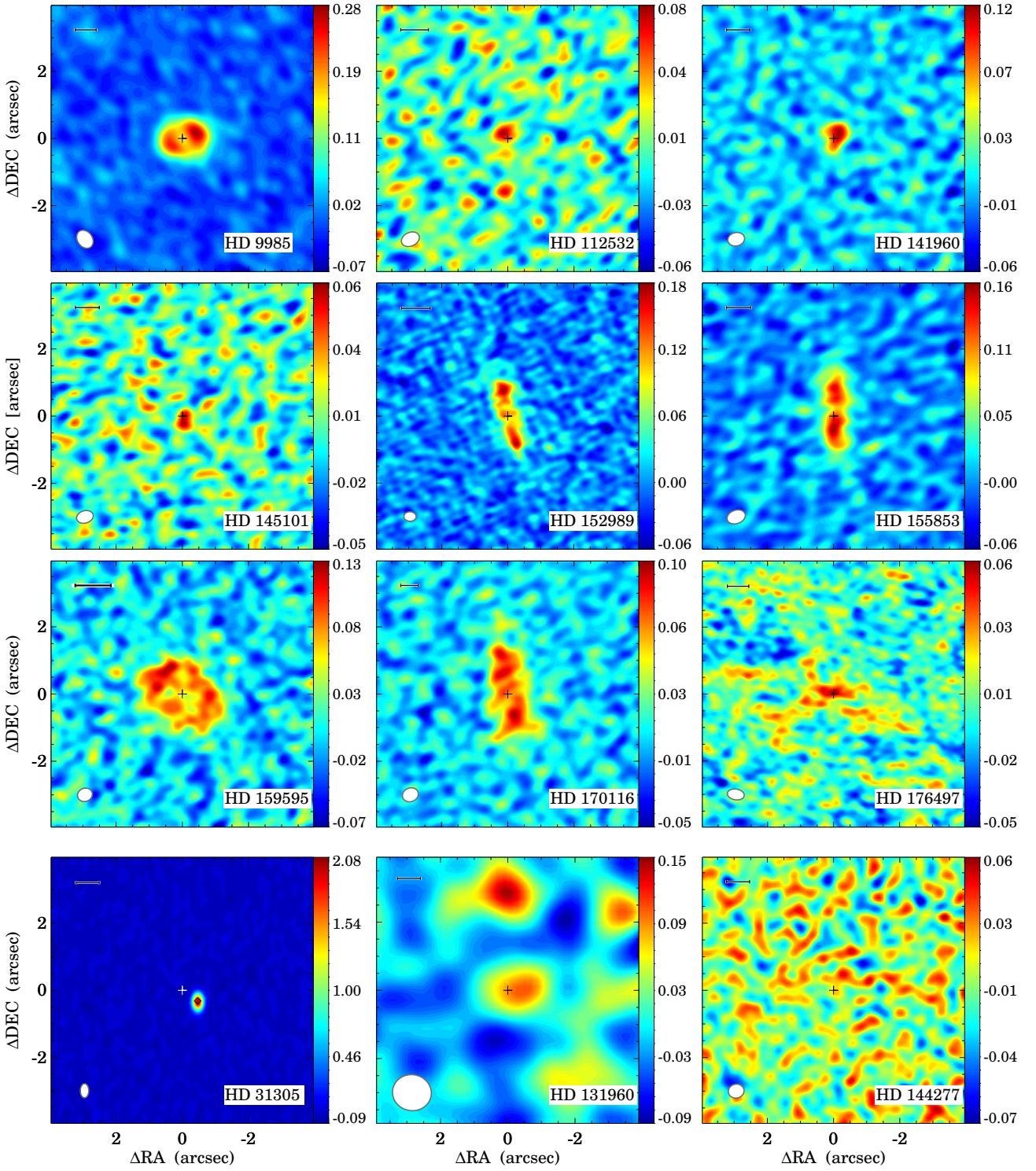


Fig. 1: ALMA Band 6 continuum emission for the observed targets. The stellar position is marked with a black plus sign. In the case of HD 31305, the position of the primary component (HD 31305 A) is shown by a white plus sign, while the companion star (HD 31305 B) is marked by a black diamond. For HD 131960 the visibility data are tapered by a Gaussian with an FWHM of $1''$. At the bottom left of each panel a filled white ellipse shows the beam size. The length of the horizontal black bars corresponds to 100 au. The color bar units are mJy beam^{-1} .

dust temperature of 110 K, corresponding to a radial distance of ~ 25 au assuming blackbody grains (Sect. 4.2).

The dust mass estimates are listed in Table 3. We caution that the uncertainties given are formal errors only, taking into account the errors in the measured flux density, the distance of

the system, and the derived dust temperature, but do not consider the possible systematic uncertainties associated with the value of the dust opacity, which can reach a factor of several (Krivov & Wyatt 2021), as well as the fact that the dust temperature is unlikely to be characterized by a single value.

Table 3: Results from continuum observations.

Target name	$L_{\text{disk}}/L_{\text{bol}}$ (10^{-4})	Model	$F_{1.33\text{mm}}$ (mJy)	R_{disk} (au)	W_{disk} (au)	i ($^{\circ}$)	PA ($^{\circ}$)	M_{dust} (M_{\oplus})	Label
Detected disks									
HD 9985	12.6	Gaussian ring	1.26 \pm 0.14 (0.06)	84 \pm 9	57 \pm 25	48 \pm 3	104 \pm 11	2.6 \pm 0.3e-01	1
HD 112532	7.3	Gaussian	0.119 \pm 0.038 (0.036)	36 \pm 17	39 \pm 7	8.9 \pm 3.7e-03	2
HD 141960	23.1	Gaussian ring	0.25 \pm 0.03 (0.02)	41 \pm 10	29	66 \pm 13	166 \pm 11	3.5 \pm 0.6e-02	3
HD 145101	6.1	Point source	0.061 \pm 0.016 (0.015)	<33	4.1 \pm 1.4e-03	4
HD 152989	75.8	Gaussian ring	1.42 \pm 0.15 (0.04)	103 \pm 7	44 \pm 9	79 \pm 2	14 \pm 1	2.1 \pm 0.2e-01	5
		Two narrow rings	0.56 \pm 0.20 (0.19)	83 \pm 13	...	77 \pm 2	15 \pm 1	8.3 \pm 3.0e-02	
			0.91 \pm 0.19 (0.16)	120 \pm 15	...	77 \pm 2	15 \pm 1	1.3 \pm 0.3e-01	
HD 155853	16.8	Gaussian ring	0.98 \pm 0.11 (0.04)	117 \pm 8	116 \pm 16	77 \pm 3	2 \pm 1	1.9 \pm 0.2e-01	6
HD 159595	21.2	Gaussian ring	1.79 \pm 0.21 (0.10)	83 \pm 7	72 \pm 18	46 \pm 10	60 \pm 10	1.4 \pm 0.2e-01	7
HD 170116	13.6	Gaussian ring	1.03 \pm 0.11 (0.04)	197 \pm 25	141 \pm 26	76 \pm 3	10 \pm 4	5.1 \pm 0.7e-01	8
HD 176497	17.0	Gaussian ring	0.135 \pm 0.032 (0.029)	72 \pm 17	50	78 \pm 7	83 \pm 7	2.7 \pm 0.7e-02	9
Non-detections									
HD 31305	? ^a	...	<0.063	<5.5e-03	...
HD 131960	13.0	...	<0.120	<2.1e-02	...
HD 144277	5.9	...	<0.072	<1.2e-02	...

Notes. The fractional luminosities ($L_{\text{disk}}/L_{\text{bol}}$) are taken from Appendix A.5. For detected disks, the estimates of the flux density at 1.33 mm ($F_{1.33\text{mm}}$), the disk radius (R_{disk}), the ring width (W_{disk}), the inclination (i), and the position angle (PA) parameters are the results of model fitting with the `UVMULTIFIT` tool. The quoted uncertainties of the flux densities are quadratic sums of the measurement errors (listed in brackets) and the absolute calibration error (which were conservatively assumed to be 10%). With the exception of HD 112532 and HD 145101, where an elliptical Gaussian and a point source model were used, respectively, we applied Gaussian ring models to fit the visibility data of the detected disks (Sect. 4.2). In the latter cases, the radius of the disk corresponds to the radius of the fitted ring, while for HD 112532 to the semi-major axis ($0.5 \text{ FWHM}_{\text{maj}}$) of the best-fitting Gaussian model. For HD 152989, an alternative model consisting of two infinitesimally thin rings was also tested (Sect. 5.3). To estimate the flux density upper limits for non-detections, we followed the method described in Sect. 4.2. The 9th column lists the derived dust masses (Sect. 4.3). ^(a) In the case of HD 31305, a significant fraction or even all of the observed excess of the system probably comes from the disk around the late-type companion, HD 31305 B. Due to the low spatial resolution of the available IR data, the fractional luminosity of the disk around HD 31305 A (if it exists at all) cannot be constrained. The last column shows which label we use to mark the given object in Figs. 7–9.

5. Analysis of line data

5.1. Imaging and CO line fluxes

To produce CO image cubes from the continuum subtracted visibility data (Sect. 3) we used the `TCLEAN` task. Similar to the continuum imaging, the *multiscale* algorithm was employed, with the same scale settings and Briggs weighting with the robust parameter set to 0.5 by default. LSR reference frame was used and the channel width was rebinned to 0.4 km s⁻¹ for ¹²CO line data and 1.6 km s⁻¹ for ¹³CO and C¹⁸O observations. Basic properties of the synthesized beams and the 1 σ rms levels are given in Table B.1.

Since ¹²CO is by far the most abundant of the three isotopologs studied, we expect the strongest signal from this molecule if circumstellar gas is present around a target. To search for ¹²CO (2–1) emission, we examined channels that are within ± 30 km s⁻¹ of the radial velocity of the target star in the LSR frame. The latter parameters were calculated from the heliocentric radial velocity data listed in Table 1. We identified four systems, HD 9985, HD 145101, HD 152989, and HD 155853, with significant line emission ($>3\sigma$), spanning several adjacent channels, which spatially coincides well with the disk observed in the continuum. In the case of HD 155853, which is located close to the galactic plane (galactic latitude $b = +2.6^{\circ}$), in the velocity range where the disk is detected, some channels show bright extended emission close to, but not overlapping with the disk. Although it does not cause a direct contamination, it affects the background flux level of the specific channels. However, we found that this effect can be eliminated by omitting visibilities

with baselines shorter than 60 m in the cleaning process. For further analysis, the ¹²CO data cube obtained in this way was used. In addition to these four discoveries, a faint but significant CO emission was identified in HD 170116, which coincides well with the southern side of the continuum disk. We found no evidence of the presence of a gas disk at our other seven targets. In the case of HD 159595, which is also located in the galactic plane ($b = -0.11^{\circ}$), spatially very extended, bright line emission is present in a large fraction of the channels studied. However, the spatial distribution of the emitting regions bears no resemblance to the structure observed in the continuum, suggesting that they are associated with background molecular cloud material rather than the disk around the star. At HD 31305, similar to the continuum observation, no emission is detectable at the primary companion, but HD 31305B clearly hosts a bright gas disk. Since this is probably a protoplanetary disk, its line measurements are discussed in more detail separately in Appendix C.

By inspecting the channel maps of the rarer ¹³CO and C¹⁸O isotopologs, we found significant emission at HD 9985, HD 145101 and HD 155853 for the ¹³CO line, with similar spatial structure and velocity range as for ¹²CO. HD 9985 and HD 155853 show also C¹⁸O line emission, but it can be detected only over a smaller area and in a narrower velocity interval than the ¹²CO and ¹³CO emissions. We note that the extensive background emissions observed in the ¹²CO data at HD 155853 are absent from the ¹³CO and C¹⁸O measurements. None of our other targets exhibit detectable ¹³CO or C¹⁸O line emission.

To construct ¹²CO moment 0 (velocity integrated) maps for HD 9985, HD 145101, HD 152989 and HD 155853, as a first step

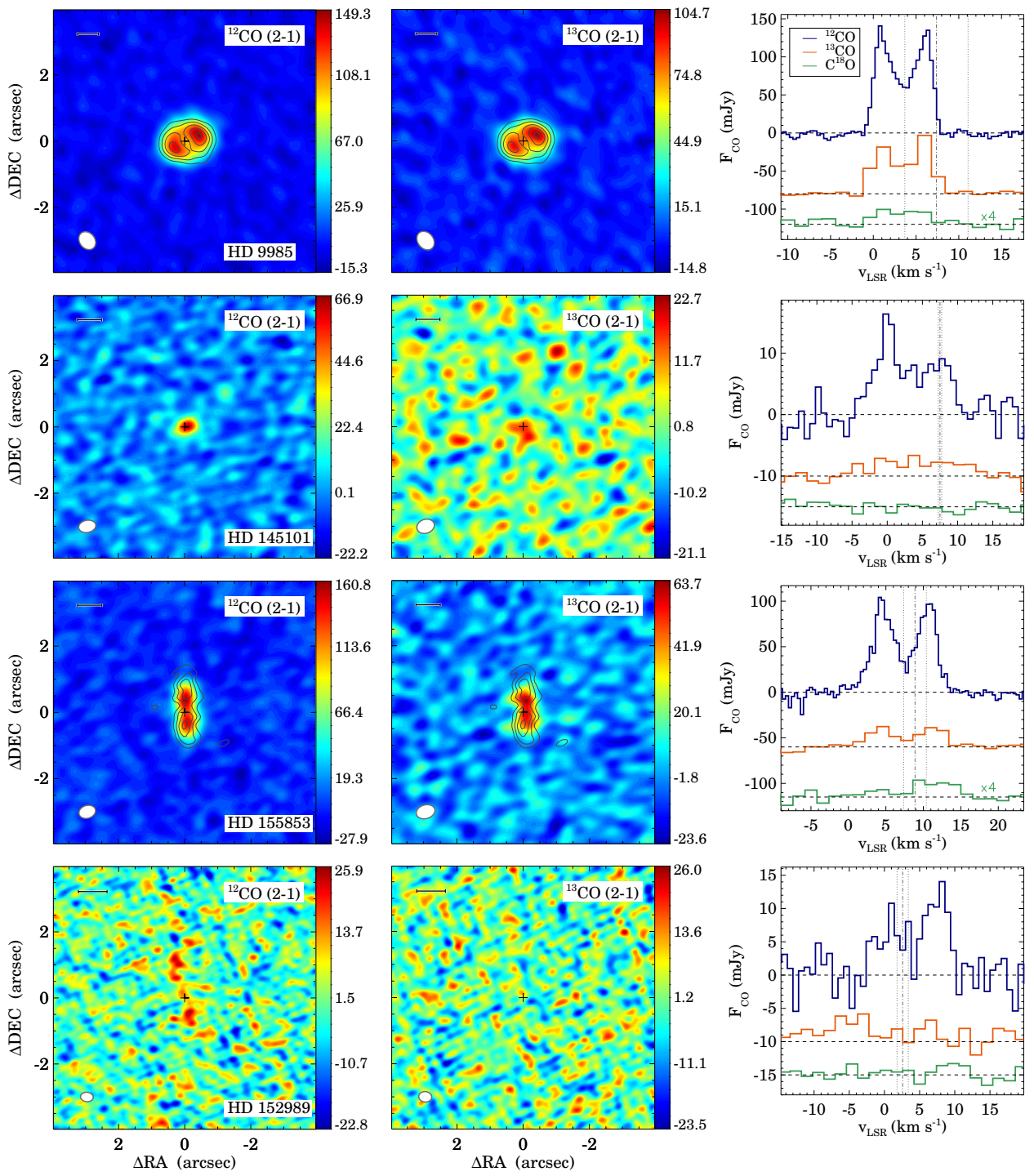


Fig. 2: ^{12}CO (2–1) and ^{13}CO (2–1) moment 0 maps for HD 9985, HD 145101, HD 155853, and HD 152989 (left and middle columns). At the bottom left of each panel a filled white ellipse shows the beam size. The length of the horizontal black bars corresponds to 100 au. The color bar units are $\text{mJy beam}^{-1} \text{km s}^{-1}$. The contours plotted over the moment 0 maps of HD 9985 and HD 155853 show the continuum emission. The contour levels are in steps of $[5, 8, 11, 14, 17] \times \text{rms noise of } 15.9 \mu\text{Jy beam}^{-1}$ for HD 9985 and $[4, 6, 8, 10] \times \text{rms noise of } 15.3 \mu\text{Jy beam}^{-1}$ for HD 155853. The right column displays the obtained CO spectra in all three isotopologs. For better visibility, the ^{13}CO and C^{18}O spectra have been shifted downward, and in the case of HD 9985 and HD 155853 the C^{18}O spectrum is multiplied by 4. The horizontal dashed lines show the zero flux levels of the spectra. The vertical dash-dotted and dotted lines mark the radial velocity of the star and its uncertainty in the LSR frame.

we identified those channels where significant, $>3\sigma$ emission is detected in the region corresponding to the continuum disk. The latter was defined by an ellipse fitted to the outer 2σ contour

of the structure detected in the continuum image. For the much fainter HD 145101 and HD 152989, this analysis was done using data cubes binned in 2 velocity channels (resulting in a chan-

nel width of 0.8 km s^{-1}). The moment 0 maps, which are shown in the left column of Figure 2, were then obtained by integrating the data cube over the derived velocity range. For all of the above processing, we used self-developed routines implemented in IDL (Interactive Data Languages). For HD 9985 and HD 155853 we repeated the above procedure to create their ^{13}CO moment 0 maps (middle column of Fig. 2). We note that the velocity ranges we obtained are consistent with the ones found for ^{12}CO . For HD 145101, which is very faint in this line, and for HD 152989, which has no detection at all, however, it was not possible to define the velocity range of the integration based on the measured results. Therefore, in these cases, we adopted the same velocity range extracted for the ^{12}CO data to construct their ^{13}CO moment 0 maps (middle column of Fig. 2). Finally, to produce the C^{18}O integrated maps, we adopted the velocity ranges used for the ^{13}CO observations for all four sources.

To measure the integrated CO line flux densities we used the moment 0 maps. For disks with resolved structure, we first determined the integration aperture, i.e. the region that belongs to the disk. We considered pixels with intensities of $>2\sigma$, where σ is the noise in the map, measured in regions outside the disk. We kept the area within 2σ around the peak with disk emission and discarded any other $>2\sigma$ pixels disjoint from this region. Then we fitted an ellipse to the mask created this way and used it as an aperture to measure the line flux. By changing the size of the elliptical aperture, we obtained a growth curve of fluxes, which ended in a flat plateau in all cases. We used the aperture corresponding to the starting point of the plateau for the final flux extraction. While this procedure worked well for the ^{12}CO and ^{13}CO maps of HD 9985 and HD 155853, where these disks form a coherent structure, to analyze the ^{12}CO data of HD 152989 we had to define three different elliptical aperture masks corresponding to the distinct, southern, central, and northern bright regions (see Fig. 2). To estimate the uncertainty of the integrated line fluxes, we placed 20 apertures identical to the source aperture at random positions outside the disk, and then derived the uncertainty as the standard deviation of the flux values measured in them.

For the C^{18}O moment 0 map of HD 9985 and HD 155853, the above procedure was performed using the aperture mask obtained for the ^{13}CO map. This resulted in measured line fluxes of $(20.1 \pm 4.5) \times 10^{-23} \text{ W m}^{-2}$ and $(18.0 \pm 5.8) \times 10^{-23} \text{ W m}^{-2}$, respectively, suggesting the presence of faint but detectable emission. Similarly, to estimate the line flux density of the disk around HD 152989 in the two rarer isotopologs, we used the aperture obtained for the ^{12}CO data. This approach yielded 3σ upper limits in both lines. In the case of HD 145101, the detected ^{12}CO emission shows a compact structure, similar to its 1.3 mm continuum map. To estimate the integrated line flux, we used an elliptical aperture with the same aspect ratio and position angle as the corresponding beam, whose size, as in the above cases, was set using the curve of growth method. The resulting aperture was then employed to estimate the uncertainties as described above. To estimate the ^{13}CO and C^{18}O line fluxes we used the same aperture defined based on the ^{12}CO moment 0 map.

In the ^{12}CO observation of HD 155853, the background emission (see above) is only present in channels between $v_{\text{LSR}} = 2.2$ and 4.2 km s^{-1} , and outside this velocity range, the data are free from its influence. This enables us to examine the impact of removing the visibility measurements with the smallest baseline on the line flux measurement. Using all baselines to construct the ^{12}CO data cube and repeating the flux measurement procedure described above, we found that the flux in the velocity range unaffected by background emission was 9% higher than in the

short baseline-free data. Taking this into account, we scaled up the ^{12}CO line flux, obtained from data with small baseline cut, by 9%. The derived integrated line fluxes are listed in Table 4. We have also plotted the spectra extracted from the apertures for all three CO isotopologs in Figure 2 (right column).

To study the faint ^{12}CO line emission found at HD 170116, natural weighting was used to improve the signal-to-noise ratio. Assuming that the possible gas is co-located with the dust material we can calculate a velocity range in which the emission should be present: $v_{\text{sys}} \pm \sqrt{GM_*/R_{\text{in}}} \sin i$, where v_{sys} is the systemic velocity, M_* is the stellar mass, R_{in} is the inner disk radius, while i is the inclination of the disk. Using the radial velocity of the star in the LSR frame as the systemic velocity, taking M_* and i from Tables 1 and 3 and assuming that $R_{\text{in}} = R_{\text{disk}} - W_{\text{disk}}/2$ we obtained a v_{LSR} interval of $[-4.4, +2.8] \text{ km s}^{-1}$ for HD 170116. Figure 3 (left) shows the naturally weighted moment 0 map of the ^{12}CO 2–1 transition for this velocity range overlaid by the contours of the natural-weighted continuum image of the source. Significant CO emission is detected only in the southern side of the continuum structure, indicating a strong asymmetry in the CO brightness distribution. By applying an elliptical aperture fitted to the 3σ contour of the continuum disk image, we obtain an integrated line flux of $(43.6 \pm 10.3) \times 10^{-23} \text{ W m}^{-2}$. Analyzing separately the regions corresponding to the southern (south-southwest) and northern (north-northeast) parts of the continuum disk, they have integrated CO fluxes of $(40.5 \pm 7.3) \times 10^{-23} \text{ W m}^{-2}$ and $(3.1 \pm 7.3) \times 10^{-23} \text{ W m}^{-2}$, respectively. By further examining the data cube, we found that the majority of detected line emission is indeed present at velocities between 0.4 and 2.8 km s^{-1} (Fig. 3, center panel). The observed CO structure has an integrated line flux of $(28.5 \pm 3.6) \times 10^{-23} \text{ W m}^{-2}$ and its brightest part coincides well with a point-like clumpy structure detected in the continuum disk. The spectrum of localized CO brightness peak is shown in Figure 3 (right). It is worth noting that, although in a different velocity range from the disk (and the brightness peak), between $+4.4$ and $+4.8 \text{ km s}^{-1}$, additional, spatially extended CO emission can be detected in the HD 170116 measurements. Given the close proximity of this star to the Galactic plane ($b = +4.7^\circ$), it is likely that the latter, narrow CO line emission is related to a background molecular cloud. Although only the faintest parts of this cloud overlap with the disk, it shows up as a narrow peak in the spectrum of the CO peak (Fig. 3, right). This background cloud has no detectable counterpart in the continuum measurement.

For the analysis of possible ^{13}CO or C^{18}O emission from the disk, moment 0 maps were generated for both the expected velocity range of the disk and the measured velocity range of the detected CO brightness peak. However, we found no signal above the noise in either line. The derived 3σ line flux upper limits are listed in Table 4.

To look for gas toward the other seven sources (HD 31305 A, HD 112532, HD 131960, HD 141960, HD 144277, HD 159595, and HD 176497), in addition to the Briggs weighted cubes, we also constructed naturally weighted and tapered (using Gaussian tapers of size 1" or 2") data sets. With the exception of HD 159595, no significant CO emissions were found at any other target. In the case of HD 159595, however, as mentioned previously, the structure of the spatially very extended, bright emission that is present in almost all channels in the studied v_{LSR} range between -30 and $+30 \text{ km s}^{-1}$, is very different from that of the disk observed in the continuum and is likely to originate from background molecular clouds. To mitigate the contamination effect from this extended emission, in the following analysis of this source, we used a data cube where only visibilities with

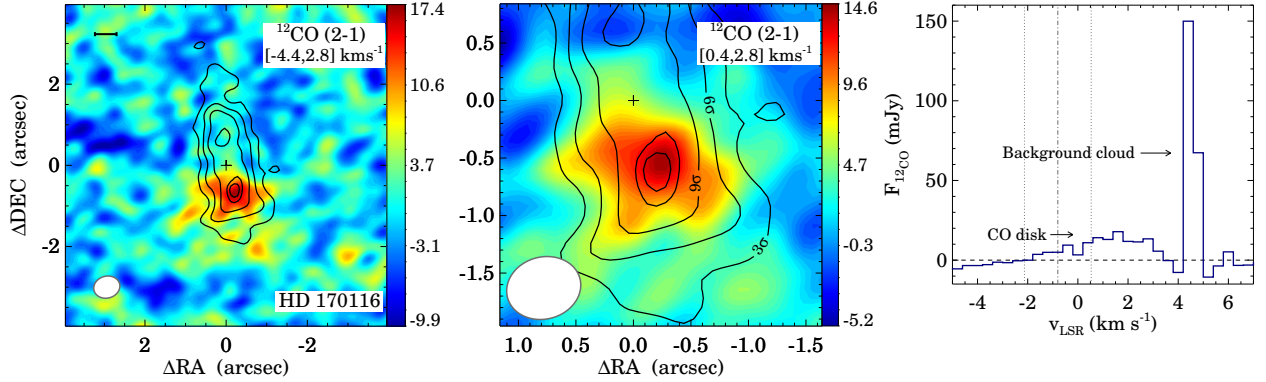


Fig. 3: Left panel: Integrated ^{12}CO (2–1) intensity map of HD 170116 between v_{LSR} of -4.4 and $+2.8 \text{ km s}^{-1}$, using natural weighted data. The applied velocity interval was calculated under the assumption that the possible gas material is co-located with the detected dust (Sect. 5.1). The color bar units are $\text{mJy beam}^{-1} \text{ km s}^{-1}$. The moment 0 map is overlaid by the contours of the natural-weighted continuum image of the source. The contour levels are at 3, 6, 9, 12, and $13 \times \text{rms}$ of the continuum image. The white ellipse in the lower left corner shows the synthetic beam. The size of the horizontal black bar in the upper left corner corresponds to 100 au. The black plus sign indicates the position of the star. Center panel: same as the left panel, but zoomed in to the center of the observed localized CO brightness peak and using a narrower integration velocity range from $+0.4$ and $+2.8 \text{ km s}^{-1}$, corresponding to the interval in which the emission is detected. Right panel: spectrum of the observed CO peak. The vertical dash-dotted and dotted lines mark the radial velocity of the star and its uncertainty in the LSR frame.

baselines of $> 100 \text{ m}$ were used in the `tclean` process. To constrain upper limits of the ^{12}CO integrated line fluxes for these seven systems, we first derived their moment 0 maps by using the expected velocity intervals. For HD 112532, HD 141960, HD 159595, and HD 176497 we assumed that the possible gas is co-located with the observed dust disk (Sect. 4.2). In the case of HD 131960, HD 144277, and HD 31305 A, no emission was detected around the stars in the mm continuum. While mid-IR measurements provide evidence of warm dust disks around the first two objects, it is unclear whether there is circumstellar dust around HD 31305 A (Sect. 4.2). Based on the dust temperatures obtained from SED fitting (Sect. A.5), we first estimated the blackbody radii of the disks around HD 131960 and HD 144277. Due to the presence of small dust particles that are inefficient emitters and thus warmer than blackbody grains present at the same location, the radii derived in this manner are lower limits (e.g., Pawellek et al. 2014). To estimate the true disk radii, we applied an empirical relation based on spatially resolved debris disks to examine the ratio of the two radius types as a function of the central stars’ luminosity (Pawellek et al. 2021). Assuming that the disks are edge-on and the possible gas is co-located with the dust, we adopted a velocity interval of 20 km s^{-1} and 16 km s^{-1} centered on the radial velocity of the star in the LSR frame for HD 131960 and HD 144277, respectively. For HD 31305 A we assumed a line width of 20 km s^{-1} centered on the systemic velocity of the CO disk around HD 31305 B (Appendix C). To estimate the 3σ upper limits of the integrated line fluxes, for objects where we detected the disk in the continuum (HD 112532, HD 141960, HD 159595, and HD 176497), we placed 20 apertures at random positions on the moment 0 maps and then computed the 1σ uncertainty as the standard deviation of the flux values measured in them. The aperture was defined by fitting an ellipse to the detected continuum disk. For HD 131960 and HD 144277, the 3σ upper limits were derived from the noise measured in their $1''$ tapered moment 0 maps, while for HD 31305 A we used the Briggs weighted map for this purpose. The obtained upper limits are listed in Table 4.

5.2. CO mass estimates

Taking an optically thin $J = 2 - 1$ rotational transition line of the observed isotopologs, ^{12}CO , ^{13}CO , or C^{18}O , the total mass of ^{12}CO gas can be estimated as:

$$M_{\text{CO}} = 4\pi md^2 \frac{F_{21}}{x_2 h v_{21} A_{21}} f_{^{12}\text{C}^{16}\text{O}/^{13}\text{C}^{18}\text{O}}, \quad (2)$$

where m is the mass of a ^{12}CO molecule, d is the distance of the object, F_{21} is the measured $J = 2 - 1$ line flux of the given ^{13}CO isotopolog, h is the Planck constant, v_{21} and A_{21} are the rest frequency and the Einstein coefficient of the transition, while x_2 is the fractional population of the upper, $J = 2$ level.

The $f_{^{12}\text{C}^{16}\text{O}/^{13}\text{C}^{18}\text{O}}$ is the abundance ratio of the ^{12}CO molecule relative to the specific isotopolog. In the local interstellar medium, the $[^{12}\text{C}]/[^{13}\text{C}]$ and $[^{16}\text{O}]/[^{18}\text{O}]$ ratios are estimated to be ~ 77 and ~ 560 , respectively (Wilson & Rood 1994). In the following analysis, we assume corresponding CO isotope ratios in the observed gas disks. Using this assumption, the line opacities can be estimated from the obtained flux ratios (Di Folco et al. 2020, eq. 1). For HD 9985, HD 145101, and HD 155853, the measured ^{12}CO to ^{13}CO flux ratios are between 1.7 and 4.5, indicating highly optically thick ^{12}CO emission in all cases with $\tau_{^{12}\text{CO}}$ of ~ 80 , ~ 25 , and ~ 24 , respectively. However, these results also suggest that their ^{13}CO line may be optically thin. This statement is further strengthened in the case of HD 9985 and HD 155853 by their measured $F_{^{12}\text{CO}}/F_{\text{C}^{18}\text{O}}$ ratios. For HD 9985, HD 145101, and HD 155853, we therefore use the ^{13}CO line measurements to estimate the CO gas mass, while for HD 152989 and HD 170116, where only ^{12}CO emission was detected, we assume that the given line is optically thin.

The fractional population of the $J = 2$ level (x_2) depends on how often the CO molecules collide with other particles, the nature of the collision partners, and the radiation field to which they are exposed. In dense media, the collisions can be frequent enough to dominate the excitation of the rotational levels, leading to local thermodynamic equilibrium (LTE) in which the level populations follow the Boltzmann distribution. If we assume this

Table 4: Results from CO line observations.

Target name	$F_{^{12}\text{CO}}$ ($10^{-23} \text{ W m}^{-2}$)	$F_{^{13}\text{CO}}$ ($10^{-23} \text{ W m}^{-2}$)	$F_{\text{C}^{18}\text{O}}$ ($10^{-23} \text{ W m}^{-2}$)	M_{CO} (M_{\oplus})	$\tau_{^{12}\text{CO}}$
Detections					
HD 9985	559.1 ± 56.3 (6.9)	316.9 ± 32.4 (6.6)	22.5 ± 5.6 (5.2)	$(2.2 \pm 0.2) \times 10^{-2}$	80 ± 22
HD 145101	80.4 ± 10.3 (6.5)	19.3 ± 4.2 (3.7)	< 10.1	$(10.3 \pm 2.3) \times 10^{-4}$	25 ± 8
HD 152989	67.7 ± 10.7 (8.2)	< 21.2	< 16.7	$(2.7 \pm 0.4) \times 10^{-5}$...
HD 155953	567.5 ± 60.8 (21.7)	134.5 ± 15.9 (8.5)	20.9 ± 6.7 (6.4)	$(7.0 \pm 0.8) \times 10^{-3}$	24 ± 4
HD 170116	40.5 ± 8.4 (7.3)	< 21.5	< 18.8	$(4.4 \pm 0.9) \times 10^{-5}$...
HD 170116 (CO peak)	28.5 ± 4.0 (2.8)	< 6.8	< 5.5	$(3.1 \pm 0.4) \times 10^{-5}$...
Non-detections					
HD 31305	< 25.1	$< 1.6 \times 10^{-5}$...
HD 112532	< 17.5	$< 7.7 \times 10^{-6}$...
HD 131960	< 31.8	$< 2.1 \times 10^{-5}$...
HD 141960	< 13.6	$< 8.5 \times 10^{-6}$...
HD 144277	< 22.1	$< 1.4 \times 10^{-5}$...
HD 159595	< 107.0	$< 2.8 \times 10^{-5}$...
HD 176497	< 25.4	$< 1.8 \times 10^{-5}$...

Notes. Integrated CO line fluxes (^{12}CO , ^{13}CO , and C^{18}O (2–1) fluxes for disks with detected ^{12}CO emission and only the ^{12}CO flux upper limits for non-detections) and CO mass estimates (M_{CO}) for our twelve targets. The quoted uncertainties of the line fluxes are quadratic sums of the measurement errors (given in brackets) and the absolute calibration error (which were conservatively assumed to be 10%). For the three disks detected in both the ^{12}CO and the ^{13}CO emission lines, the last column provides the estimated ^{12}CO optical depth. The quoted uncertainties of the $\tau_{^{12}\text{CO}}$ estimates are formal and only consider the uncertainties of the line flux measurements, but not account for the uncertainties of the adopted isotopolog abundance ratio.

situation in our newly discovered gas disks, i.e. that LTE holds, then we need the gas excitation temperature to estimate x_2 . Using the measured peak flux values of the optically thick ^{12}CO data we obtained minimum gas brightness temperatures of 11 K for HD 9985 and HD 155853 and 5 K for HD 145101. In previously identified CO-bearing debris disks, where the gas excitation temperature could be estimated, similarly low values between 8 and 30 K were typically obtained (Kóspál et al. 2013; Flaherty et al. 2016; Matrà et al. 2017a; Higuchi et al. 2020; Di Folco et al. 2020). In our calculations we have finally adopted an excitation temperature of 20 K for all gaseous disks. The obtained CO gas mass estimates and their formal uncertainties, which take into account the errors in the distance and flux values, are summarized in Table 4.

Several simplifications have been made in the above calculations, and the uncertainties in the CO mass estimates are in fact likely larger than the calculated formal errors. To assess how feasible the hypothesized LTE approximation is, we should know what types of collision partners are present and what their densities are. However, no measurements are available for other possible important constituents of the observed gas disk, such as H_2 molecules if the gas is primordial, or H, C, O atoms or electrons in the case of second generation gas material. We also know little about the real gas temperatures. For our adopted excitation temperature of 20 K and LTE, the $J = 2$ rotational level is very efficiently populated, but a significantly different temperature and/or non-LTE environment may result in a lower fractional population than assumed and, accordingly, a higher CO mass.

For three disks, the ^{12}CO mass was estimated from the measured ^{13}CO line fluxes, assuming a $^{12}\text{CO}/^{13}\text{CO}$ abundance ratio that is typical of the local interstellar material. However, isotope selective photodissociation or isotopic fractionation can significantly affect the abundances of these molecules leading to very different ratios from disk to disk (Visser et al. 2009). While the

former process tends to result in a higher $^{12}\text{CO}/^{13}\text{CO}$ abundance ratio, the fractionation can even reduce it if the gas is sufficiently cold.

Taking all these effects into account, the actual mass of CO may differ by as much as several factors from what we have estimated, and is more likely to be higher.

For those targets where no gas emission was detected, we derived an upper limit for the CO mass. To do this, we used the obtained CO flux upper limits and assumed LTE conditions and a gas excitation temperature of 20 K. The results are given in Table 4. As a caveat, we note that in these presumably gas-poor systems, it is likely that radiative processes rather than the collisions govern the population of the rotational levels. Such subthermal excitation can lead to a lower population of the $J=2$ rotational level (x_2) than we assumed, resulting in higher upper limits for CO mass (Matrà et al. 2015; Cataldi et al. 2023).

5.3. Spatial distribution of CO gas

To investigate whether the detected CO gas is co-located with the dust in HD 9985, HD 155853, HD 152989, and HD 170116, we constructed their ^{12}CO position-velocity (PV) diagrams along the major axis of the disks (Figs. 4a–d). The overplotted black solid curves show the tangential velocity of the gas as a function of projected distance from the star, while the diagonal black dashed lines mark the radial velocities and positions of the gas orbiting at two orbital radii, assuming Keplerian rotation. To calculate the diagrams, we need as input parameters the position angles and inclinations of the disks as well as the distances and stellar masses (Matrà et al. 2017a). For HD 152989 and HD 170116, where the CO emission is relatively weak, the disk position angles and inclinations obtained for the continuum data were adopted from Table 3. In the case of HD 9985 and HD 155853 we used their moment 0 maps to estimate these disk parameters. To this end we made cuts from the stellar position toward po-

sition angles between 0 and 360° in 5° increments, determined the location of maximum intensity along these cuts, and finally the derived positions were fitted with an ellipse. In this way, we obtained $116 \pm 7^\circ$ and $49 \pm 3^\circ$ for the position angle and inclination of the CO disk around HD 9985, and $2.5 \pm 1^\circ$ and $77 \pm 2^\circ$ for HD 155853. We note that these disk parameters are in very good agreement within the uncertainties with the *PA* and *i* estimates obtained from their continuum observations (Table 3). The distances and stellar masses were taken from Table 1 for all four systems.

The PV diagram shows that the bulk of the CO gas in HD 9985 lies between ~ 55 and ~ 125 au (Fig. 4a). By modeling its continuum data we found that the peak of the dust radial distribution is at ~ 84 au and the FWHM of the fitted Gaussian profile is ~ 57 au (Table 3), indicating that the densest part of the dust ring is confined between ~ 55 au and ~ 115 au, i.e. the dust and gas in this system are probably quite well co-located. The good agreement of the images and normalized azimuthally averaged radial flux profiles for the continuum and ^{12}CO moment 0 maps in Figures 2 and 4e (top) further supports this finding. As Figures 1 and 2 show, for HD 9985, the brightness distributions of the ^{12}CO and ^{13}CO integrated maps, and the continuum emission all peak in a similar location at the northwestern ansa of the ring. The maximum brightness of the northwestern part of the ring exceeds that of the southwestern part by 2.4, 2.4, and 2.6σ in the continuum, ^{12}CO , and ^{13}CO maps, respectively. Although the differences measured in individual maps are not significant in themselves, considering them together, they hint at a brightness asymmetry, given the positional coincidence. Detailed analysis of this brightness asymmetry will be the topic of a future study.

In the case of HD 155853, we found that the CO gas is mostly situated between 45 and 140 au (Fig. 4b), closer to the star than large dust particles whose emission comes mainly from radial distances between 60 and 175 au (Table 3). Figures 2 and 4e (bottom) also clearly illustrate this discrepancy in the radial spatial distributions of gas and dust. This property of HD 155853 makes it most similar to HD 21997 and HD 131488 among the previously known CO-bearing disks, in which the gas and dust components also show significant spatial differences. In these disks the inner boundary of the gas appears substantially closer to the star than that of the large dust particles (Kóspál et al. 2013; Pawellek et al. 2024). Based on the ^{12}CO and ^{13}CO moment 0 maps (Fig. 2), the northern part of the disk is brighter than the southern one. However, the difference in peak emissions between the northern and southern regions is less than 1.7σ in both maps. Further higher sensitivity observations are needed to confirm and study the possible brightness asymmetry. We note that in the continuum image, contrary to the CO moment 0 maps, the southern part of the disk is brighter, but the peak is not significant, since the brightness difference compared to the northern part is only $\sim 1\sigma$.

Assuming a dust ring with a Gaussian radial brightness profile, the analysis of the continuum data for HD 152989 indicated that the majority of the large grains are located between 80 and 125 au (Table 3). In contrast, the PV diagram of the object suggests that there is little gas between these two radial distances, and that the CO is instead mostly concentrated in two rings at ~ 75 and ~ 130 au (Fig. 4c). Motivated by this result, we examined whether the dust distribution could be consistent with such a morphology. To do this, we adopted a UVMULTIFIT model in which the emission is associated with two infinitesimally thin rings with the same position angle and inclination. The model fit yielded a position angle of $15 \pm 1^\circ$ and an inclination of $77 \pm 2^\circ$, both are consistent with the results of the Gaussian ring model

within the uncertainties (Table 3). For the radius and flux density of the inner ring we obtained 83 ± 13 au and 0.56 ± 0.20 mJy, while the best estimate for the radius and flux density of the outer ring are 120 ± 15 au and 0.90 ± 0.19 mJy. Using BIC to assess the goodness-of-fit of the two assumed models – the single Gaussian ring and the double narrow ring, which have 7 and 8 free parameters, respectively – we found no significant difference between them. The best-fit radii of the two continuum dust rings agree reasonably well with the estimated radii for the possible two gas rings. It is therefore conceivable that the dust and gas are in fact quite well co-located and exist in two rings separated by a zone depleted in both materials. This would make this system unique as we do not know other gas-bearing debris disks where the gas is located in multiple distinct rings.

According to the continuum model of HD 170116, the bulk of the dust observed at 1.33 mm lies between 130 and 270 au (Fig. 4d). The PV diagram of the detected ^{12}CO gas, which is concentrated in the southern wing of the disk, also shows that the gas appears to reside roughly within this radial interval. The bright CO clump is located close to the inner edge of the disk. Note that while for the other three objects we used the ^{12}CO data to estimate the systematic velocity of the gas, this was not possible for the HD 170116, where we therefore adopted the measured radial velocity of the star.

By fitting a two-dimensional elliptical Gaussian model to the ^{12}CO moment 0 map of HD 145101, we found that its gas disk is marginally resolved and has FWHMs of $0''.39 \pm 0''.11 \times 0''.30 \pm 0''.10$, implying a characteristic disk radius of 27 ± 8 au. This disk size is consistent with the upper limit obtained from the analysis of the continuum data (< 33 au, Table 3).

6. Discussion

In our mini-survey we observed 12 young intermediate mass stars, 9 of which are found to have detectable millimeter continuum emission from surrounding dust-rich debris disks, and 5 of which also exhibit CO line emission. Over the past decade, dozens of young, dust-rich debris disks have been targeted in various ALMA observing programs to study their fundamental properties and assess their CO content. In the following discussion, we combine our results with data from the literature to investigate the occurrence of CO gas in dust-rich young debris disks, as well as the similarities or differences of the newly discovered CO-bearing debris disks to previously identified ones. The unified sample also allows us to improve our knowledge of the general characteristics of young CO-bearing systems, to examine the environmental conditions under which they can form, and to confront the observational results with the current theories of the origin of the gas. The dust continuum has been spatially resolved for most of our targets allowing us to investigate possible mechanisms for the dynamic excitation of these disks and whether the result of this analysis could indicate the presence of larger planet(s) in the system.

6.1. Sample of young dust-rich debris disks observed by the ALMA

For one of our targets, HD 31305, the millimeter continuum and line emission has been found to originate from a disk around its companion star, presumably of protoplanetary nature. This discovery raises the possibility that the observed infrared excess of the system is also more likely associated with this young gas-rich disk, and that HD 31305 may have no circumstellar material at all, or that its possible disk is much fainter than pre-

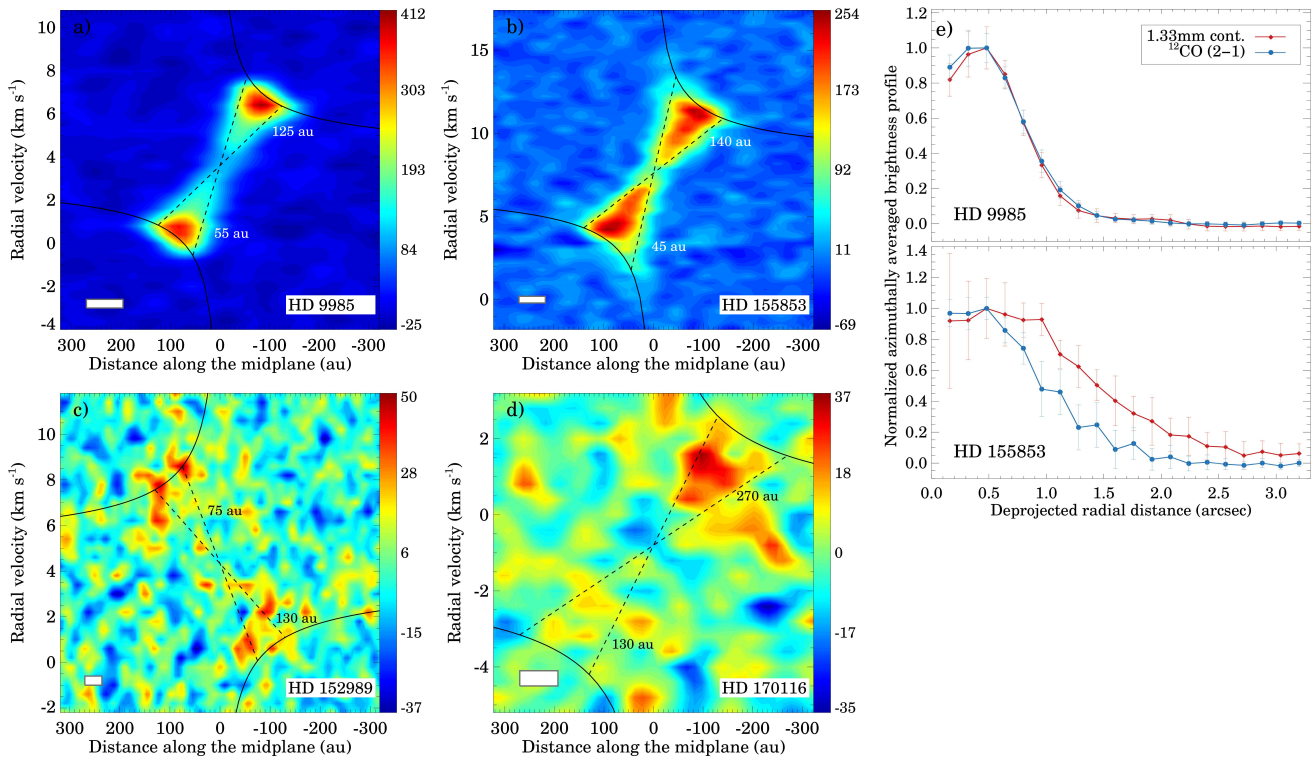


Fig. 4: a–d): Position-velocity diagrams of ^{12}CO (2-1) emission for HD 9985 (a), HD 155853 (b), HD 152989 (c), and HD 170116 (d). The color bar units are mJy beam $^{-1}$ channel $^{-1}$. The black solid curves show the tangential velocity of the gas, while the black dashed diagonal lines display the line-of-sight velocity of the gas at a fixed orbital radius as a function of projected separation. To derive these, we assume a Keplerian rotation profile for the gas, the distance and mass of the star are taken from Table 1, and the position angle and inclination of the gas disk are from Sect. 5.3. The white rectangle at the bottom left represents the spectro-spatial resolution. e): Azimuthally averaged radial profile for the continuum and ^{12}CO (2-1) data for HD 9985 (top) and HD 155853 (bottom). For comparison, the profiles are normalized to unity.

viously thought. We have therefore excluded this system from our further analysis. The other 11 disks – 10 of which are hosted by A-type stars and 1 possessed by an early F-type star – are all younger than 50 Myr and have fractional luminosities $>5\times10^{-4}$. In the literature, we identified 46 additional debris disks around stars with spectral types from A to K that are similarly young and dust-rich and for which ALMA millimeter CO line measurements are available (Kóspál et al. 2013; Dent et al. 2014; Lieman-Sifry et al. 2016; Marino et al. 2016; Moór et al. 2017, 2019; Di Folco et al. 2020; Kral et al. 2020b; Schneiderman et al. 2021; Lovell et al. 2021b; Rebollido et al. 2022). The relevant properties of the 46 systems are summarized in Table D.1. Of the total sample of 57 disks, 30 are around A-type stars, while the other 27 host stars have F–K spectral types⁴.

6.2. Detection rate of CO gas

In the combined sample, the presence of CO gas has been detected in 19 disks around A-type stars and in 4 disks surrounding later-type stars. So, in line with previous results (Lieman-Sifry et al. 2016; Moór et al. 2017), the majority of CO-bearing disks are found around A-type stars. However, the new, larger sample now allows a finer analysis of the detection rate as a function of the luminosity of the host stars. All but two gaseous disks have ^{12}CO luminosities $L_{^{12}\text{CO}(2-1)} > 9.5\times10^{16}$ W. The gas disks around HD 172555 and HD 181327 have substantially lower ^{12}CO (2-1) luminosities of 1.3×10^{16} W and 6.5×10^{15} W, respectively. They are among the closest stars in the sample, and similarly faint gas disks such as they host would be undetectable for most of the other objects in the sample, which are typically located >100 pc away. The sample also includes three objects whose $3\sigma_{L_{^{12}\text{CO}(2-1)}}$ detection limits are higher than 9.5×10^{16} W (HD 145263, HD 145880, and HD 159595). To avoid detection bias when examining the dependence of detection rates on stellar luminosity, the above five objects were not taken into account. We then divided the remaining 52 systems into four subgroups of 13 objects each, according to their stellar luminosity. In the case of HD 106906, which is a nearly equal mass binary with a projected separation of 0.36–0.58 au (Rodet et al. 2017), $\sim 3.5 L_\odot$, half of the total luminosity of the system was taken into account in the course of grouping. From the lowest to the highest luminosities, the subgroups L1 ($0.18 L_\odot < L_* < 3.52 L_\odot$), L2 ($3.53 L_\odot < L_* < 6.47 L_\odot$), L3

⁴ Our original target list included 28 dust-rich debris disks, out of which 12 were observed in the project (Sect. 2). We note that of the 16 targets that were finally not measured, eight have since been observed with the ALMA 12-m Array as part of two other projects (2022.1.00968.S, PI: James Miley; 2024.1.00852.S, PI: Joshua Lovell). The latter measurements were also performed in Band 6 and similarly to our project they also targeted the ^{12}CO , ^{13}CO , and C^{18}O rotational lines in addition to the continuum. Following their analysis, the sample can be expanded further in the future.

($6.54 L_{\odot} < L_{*} < 11.7 L_{\odot}$), and L4 ($11.8 L_{\odot} < L_{*} < 21.9 L_{\odot}$) typically include stars with K7–F5, F5–A9, A8–A4 and A4–A0 spectra.

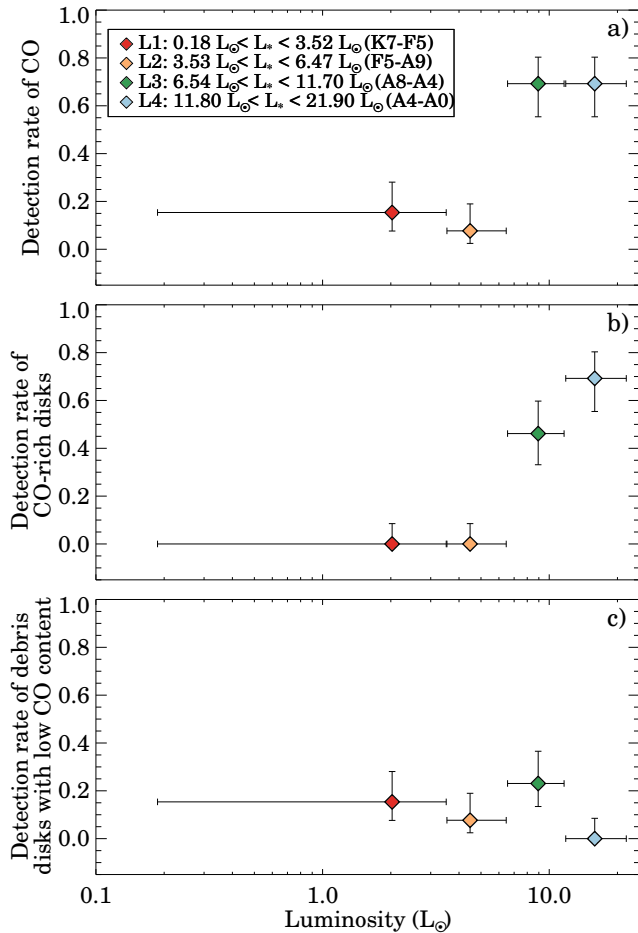


Fig. 5: a) Detection rates of CO gas in debris disks as a function of host star luminosity. Within the 52-member sample, four subgroups (L1–L4) were defined according to luminosities, with 13 disks in each subgroup. b) Detection rates of CO-rich debris disks as a function of host star luminosity. c) Detection rates of debris disks with low CO content as a function of host star luminosity.

Figure 5a shows the proportions of debris disks showing detected ^{12}CO (2–1) emission with a luminosity of $>9.5 \times 10^{16} \text{ W}$ in the four stellar luminosity intervals. While in the two lower luminosity subgroups (L1 and L2) the detection rates of CO gas are only $15.4^{+12.7\%}_{-7.8\%}$ and $7.7^{+11.3\%}_{-5.2\%}$, respectively, for disks around stars belonging to the higher luminosity L3 and L4 subgroups, the detection rates are significantly higher, at $69.2^{+11.1\%}_{-13.8\%}$ in both cases⁵. If we consider only CO-rich debris disks (Fig. 5b), i.e. systems with $M_{\text{CO}} > 10^{-3} M_{\oplus}$, we find that there are no such disks in L1 and L2 subgroups, while in L3 we obtain a slightly lower detection rate ($46.2^{+13.6\%}_{-13.0\%}$) than when we consider also objects with lower CO mass (see above). Interestingly, the CO-bearing debris disks around stars with luminosity $>13.2 L_{\odot}$ are

⁵ Because of the small samples, the lower and upper bounds of the 68.2% confidence interval were computed using the approach proposed by Agresti & Coull (1998) and available in the `binom` library of the R statistical package.

all CO-rich. When we compare the combined L1 and L2 and the combined L3 and L4 subgroups, the Fisher's exact test⁶ we applied shows a significant relationship between stellar luminosity and the occurrence of CO-bearing disks, regardless of whether all CO detections or only CO-rich objects are considered. Finally, we note that if only the low CO content ($M_{\text{CO}} < 10^{-4} M_{\oplus}$) debris disks are considered, their detection rates were similar in all four luminosity groups: $15.4^{+12.7\%}_{-7.8\%}$, $7.7^{+11.3\%}_{-5.2\%}$, $23.1^{+13.5\%}_{-9.6\%}$, and $0^{+8.5\%}_{-1.4\%}$ in the L1, L2, L3, and L4, respectively (Fig. 5c).

There are a total of 26 disks in the L3 and L4 subgroups, of which 8 have fractional luminosities between 5×10^{-4} and 10^{-3} , and 18 with $f_d > 10^{-3}$. In the "low" f_d subset there are 3 disks with detected CO gas ($37.5^{+17.6\%}_{-14.8\%}$), whereas in the "high" f_d subset there are 15 ($83.33^{+7.1\%}_{-10.6\%}$, only HD 95086, HR 4796, and HD 176497 have no CO detection). However, using again Fisher's exact test to compare the rates, we obtained a probability of 0.06, implying that the difference between the occurrences of CO-bearing disks in the "low" and "high" f_d groups is statistically not significant.

Systems belonging to the L3–L4 subgroups have ages between 6 and 48 Myr; however, their age distribution – due to most of them being members of the Sco-Cen association (15 out of 26) – is far from uniform. The sample contains 19 objects younger than 20 Myr and 7 with ages between 20 and 48 Myr, while for HD 32297 only an upper limit of 30 Myr is available for the age. By assigning the latter object to the "older" systems, we obtain a CO gas detection rate of 6/7 ($85.7^{+9.3\%}_{-18.2\%}$) in this group, while in the "younger" group this rate is 12/19 ($63.2^{+10.2\%}_{-11.5\%}$). When comparing the proportion of CO-bearing debris disks in the two different age groups, we found no statistically significant difference between them by applying Fisher's exact test. This remains true even if we assign HD 32297 to the younger subsample. It is safe to say that within the studied age range of 6 to 48 Myr, we found no evidence for an evolutionary trend in the detection rates of CO-bearing disks with age. However, the sample size of older disks is still quite small.

Finally, we compared the cumulative distributions of the ^{12}CO (2–1) line luminosities of the disks in the combined L1/L2 ($L_{*} < 3.52 L_{\odot}$) and L3/L4 ($L_{*} > 3.53 L_{\odot}$) subgroups. With the exception of NO Lup, for which the J=3–2 rotational transition of ^{12}CO was measured, observations of the J=2–1 line are available for all objects in the sample. For NO Lup, the obtained $L_{12\text{CO}(3-2)}$ luminosity was converted to $L_{12\text{CO}(2-1)}$ by assuming LTE for gas at a temperature of 20 K. To infer the cumulative distribution functions of the given groups, we used the Kaplan-Meier estimator implemented in the `lifelines` package (Davidson-Pilon 2019), which considers not only detections, but also the measured CO line luminosity upper limits. A logrank test showed that the observed difference between the distributions of ^{12}CO line luminosities of the two subgroups (Fig. 6) is statistically significant. In line with our previous results based on detection rates (see above), this test also confirms that the CO component of debris disks around early type stars with higher luminosity differs significantly from that of disks around late type, low luminosity stars.

6.3. Radial location of planetesimal belts in CO bearing debris systems

Large dust particles probed at 1.3 mm are little influenced by stellar radiative/wind forces and thus can serve as a proxy for

⁶ We employed the `fisher.test` routine implemented in the R statistical package.

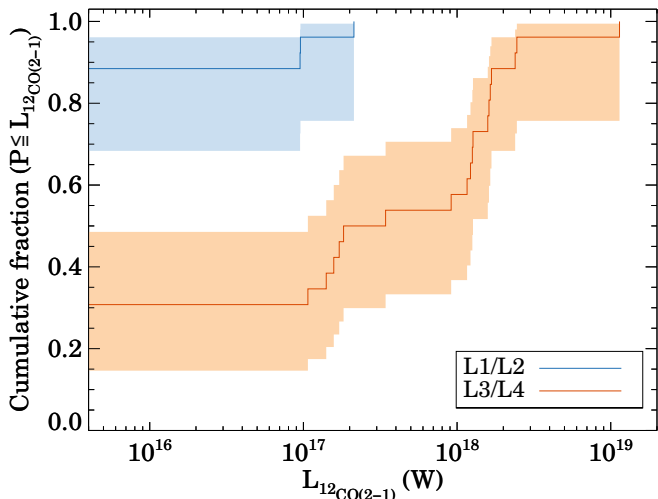


Fig. 6: Cumulative distribution functions of the ^{12}CO line luminosities of debris disks belonging to the L1/L2 (blue curve) and L3/L4 groups (orange curve). The shaded regions show 95% confidence intervals.

the spatial distribution of unseen parent planetesimals, the possible source of gas. We detected continuum millimeter emission from nine of the debris disks we observed with ALMA. In Figure 7 we plotted the obtained radii and, where available, the widths of these disks as a function of the stellar luminosity. In cases where the widths of the belts were fixed to be $0.7R_{\text{disk}}$, the vertical bars indicating these parameters are marked with dotted lines. For HD 152989, we used the parameters of the single Gaussian ring model for simplicity, but note that the double ring model also gives very similar results for the inner and outer edges of the debris disk (Sect. 5.3). Systems where no CO emission is detected are shown by empty squares, while CO-bearing debris disks are marked by filled circles. For the latter, different colors were used according to the derived CO mass, distinguishing three categories: disks with low M_{CO} of $<10^{-4} M_{\oplus}$, and CO-rich debris disks with M_{CO} between 10^{-3} and $10^{-2} M_{\oplus}$, and with $M_{\text{CO}} > 10^{-2} M_{\oplus}$. In the combined sample, radii derived from spatially resolved data are available for 17 additional disks around A-type stars having luminosities similar to our 9 objects ($> 6 L_{\odot}$). These systems are also plotted in Fig. 7. For 15 of them, the results are also based on measurements at millimeter wavelength, while in the case of HD 111161 and HD 143675 the disk has only been detected in scattered light. Since small particles observed in scattered light are significantly affected by the radiation pressure, for the latter two objects we only assumed that the peak of the radial distribution of the small dusts roughly coincides with that of the larger particles measured at mm wavelengths, but did not consider the inferred radial extent, which could be much wider than the planetesimal belt due to interactions with the radiation forces. Finally, we also added the disk of HD 172555 to the plotted sample, whose radius estimate was taken from Schneiderman et al. (2021). Thus we plotted 27 disks in total. While the nine disks from our program are marked with numbers, the other objects from the literature are marked with letters. Using spatially resolved millimeter observations of debris disks, Matrà et al. (2018) derived an empirical relationship between the radius of the belts and the luminosity of the central star. Figure 7 shows the updated version of this relationship based on a larger sample (Matrà et al. 2025).

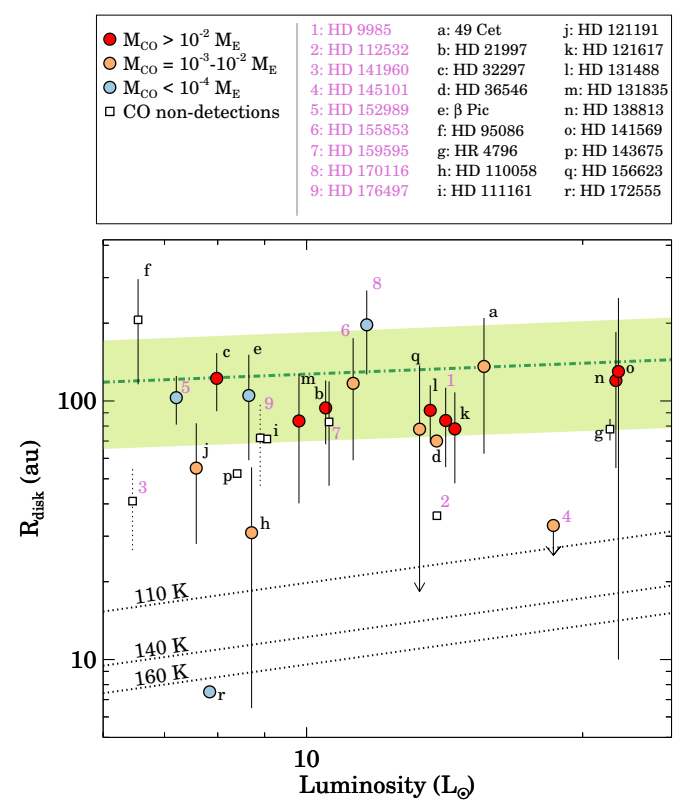


Fig. 7: Radii of dust disks as a function of stellar luminosities. In addition to the 9 disks we detected (indicated by numbers) 17 additional, previously identified debris disk systems (indicated by letters) are also displayed. The data for the latter objects are taken from Table D.1. The vertical bars represent the radial extent of the disks. For disks where the width parameter was fixed in the modeling the bars are shown by dotted lines. In the case of HD 156623 (marked by q) only an upper limit is available for the position of the inner edge of the disk. With the exception of HD 111161 (i), HD 143675 (p), and HD 172555 (r), the size estimates are derived from millimeter continuum observations. Different symbols indicate those systems where CO gas is detected and those where it is not, and within the first group three categories are further distinguished by CO mass estimates. The green dashed-dotted line represents the best fit of the empirical planetesimal belt radius–stellar luminosity relationship (Matrà et al. 2025), while the green shaded region shows the $\pm 68\%$ confidence taking into account both the intrinsic scatter as well as the uncertainties of the obtained parameters.

As Fig. 7 demonstrates, the radii of the planetesimal belts in CO-rich systems are not different from those in which only small amounts of CO gas have been found, or even no gas was detected at all. In the most CO-rich objects ($M_{\text{CO}} > 10^{-2} M_{\oplus}$) the peak radii of the planetesimal belts lie in a relatively narrow range from 78 to 130 au. The relative width ($W_{\text{disk}}/R_{\text{disk}}$) of these belts, in most cases, are between 0.5 and 1.1. Three of these particularly CO-rich systems, HD 9985, HD 121617, and HD 131488, are very similar to each other, both in terms of the size of their planetary belts and the luminosity of their host stars. However, if the radial extent of the gas disk is taken into account in the comparison, the strong similarity holds only for the first two systems since while in HD 9985 and HD 121617 the gas and dust are quite well co-located (Sect. 5.3 and Cataldi et al. 2023),

in HD 131488 the gas disk extends much further inwards than the dust disk (Pawellek et al. 2024).

With the exception of HD 172555, where the observed warm dust and CO gas may have been released in a giant collisional event (Lisse et al. 2009; Schneiderman et al. 2021), the planetesimal belts in the other systems are situated at tens of au from their star. Of the CO-rich debris disks, the one around the newly discovered HD 145101 has the smallest radial extent. In a sufficiently high temperature environment CO and CO₂ ices trapped in an amorphous water ice matrix can desorb. Laboratory experiments indicate significant gas releases at the phase change from amorphous to crystalline water at ~ 140 K and also when the desorption of water ice occurs at ~ 160 K (Collings et al. 2003). In real astrophysical environments, however, the heating of ice is much slower than in the laboratory, resulting in lower desorption temperatures (Collings et al. 2003; Martín-Doménech et al. 2014). Considering realistic heating rates of comets, water ice desorption is more likely to occur at temperatures around 110–120 K (Collings et al. 2004). In the figure we indicated regions corresponding to the relevant temperatures mentioned above. These were calculated assuming planetesimals with an albedo of 5%. This suggests that desorption processes in the inner regions of the disks around HD 110058, HD 141569, and HD 156623 and in the disk of HD 145101 may also contribute to CO gas production. In the case of HD 110058, this possibility has already been raised by Hales et al. (2022) in their analysis of the gas disk. While in the case of HD 145101 we only have an upper limit for the size of the continuum disk, by analyzing its ¹²CO moment 0 map we obtained an estimate of 27 ± 8 au for the characteristic radius of the gas disk (Sect. 5.3), which corresponds to a temperature of 110 ± 16 K for planetesimals with an albedo of 5% using the luminosity of the host star. This suggests that CO and CO₂ gas can be released from the surface layers of larger icy bodies, even as a result of desorption. The temperature of smaller dust particles, as they are inefficient emitters, could be even higher. From the available SED data, we inferred a characteristic dust temperature of 163 ± 15 K for this disk (Sect. A.5), suggesting that the ice mantles of small dust particles, if any, may sublimate and contribute to gas production.

Of the eight disks successfully resolved in our study, those around HD 112532 and HD 141960 are among the smallest, with sizes well below those predicted by the empirical relation (Fig. 7). The radius of the belt around HD 170116, however, is one of the largest among the resolved disks around young A-type stars. This conclusion regarding the disk's outstanding size remains valid even when compared to the sample of 74 debris belts studied in the REASONS millimeter survey, which also includes disks around older stars with different spectral types (Matrà et al. 2025).

6.4. Second generation gas produced in a steady-state collisional cascade?

The observed dust content of most known debris disks can be explained by the slow, steady state collisional grinding of a planetesimal belt that is more or less co-located with the dust ring (Wyatt 2008). If the minor bodies involved are rich in volatiles, collisions can result not only in smaller and smaller fragments and eventually dust particles, but also in the release of second generation gas material (Zuckerman et al. 2012; Matrà et al. 2015; Kral et al. 2017). Assuming that the icy exo-planetesimals are similar to comets in the Solar System (Mumma & Charnley 2011; Bockelée-Morvan & Biver 2017), the release of H₂O, CO, and CO₂ molecules is expected to be predominant. If there is no

effective shielding mechanism in operation, these molecules dissociate relatively quickly ($t_{\text{phd}} \lesssim 120$ yr even for CO molecules, the most resistant among them, Visser et al. 2009; Heays et al. 2017) under the influence of interstellar and stellar UV photons.

According to Matrà et al. (2017b) the mass loss rate of solids at the bottom of the ideal collisional cascade can be estimated as

$$\dot{M}_{\text{D}_{\text{min}}} (M_{\oplus} \text{yr}^{-1}) = 1.2 \times 10^{-3} \left(\frac{R_{\text{disk}}}{\text{au}} \right)^{1.5} \left(\frac{W_{\text{disk}}}{\text{au}} \right)^{-1} f_{\text{d}}^2 \left(\frac{L_{*}}{L_{\odot}} \right) \left(\frac{M_{*}}{M_{\odot}} \right)^{-0.5}, \quad (3)$$

Assuming that the gas release is mediated by collisions that expose new icy surfaces or release trapped gas, a simple estimate of its production rate and finally the mass of CO can then be derived (Matrà et al. 2019):

$$M_{\text{CO,pred}} = \dot{M}_{\text{D}_{\text{min}}} t_{\text{phd}} \frac{f_{\text{CO+CO}_2}}{1 - f_{\text{CO+CO}_2}}, \quad (4)$$

where $f_{\text{CO+CO}_2}$ is the mass fraction of CO+CO₂ in the planetesimals involved in the cascade. In reality, the estimate of $M_{\text{CO,pred}}$ is subject to large uncertainties. First, the typical formal uncertainty of the $\dot{M}_{\text{D}_{\text{min}}}$ estimate is 40–60%, and the real uncertainty could be even substantially higher as there are a number of simplifying assumptions behind Eq. 3. For example, the luminosity is included because brighter stars have a stronger radiation pressure and can therefore blow out larger dust particles, meaning that the same fractional luminosity corresponds to a larger mass in small dust particles. However, there are debris disks where the size of the smallest particle does not necessarily correspond to the blowout grain size, it can either be larger than that (Pawellek et al. 2014), or smaller in disks with a very high f_{d} and/or having significant gas content (Thebault & Kral 2019; Bhowmik et al. 2019; Singh et al. 2021). Moreover, even if we consider only comets in the Solar System, we see significant differences in their CO+CO₂ abundance ($f_{\text{CO+CO}_2}$), and it is reasonable to assume that for comets in different exoplanetary systems this parameter may show even larger diversity. The photodissociation lifetime of CO gas also has its own uncertainty e.g. depending on the possible shielding processes.

Figure 8 shows the mass loss rates ($\dot{M}_{\text{D}_{\text{min}}}$) computed from Eq. 3 as a function of the observationally estimated CO mass for 46 debris disks including 9 from our sample. Only disks with radii derived from spatially resolved data were considered. Additionally, we excluded systems whose circumstellar material is believed to be of transient origin rather than related to a steady-state collisional cascade. Following these principles, two CO-bearing debris disks were excluded from this analysis. For HD 172555, it was suggested that the observed warm dust and CO gas may have transient nature, presumably resulting from a recent giant collision (Lisse et al. 2009; Su et al. 2020; Schneiderman et al. 2021). In the case of NO Lup, only an upper limit of the disk size is available, and the fractional luminosity of the cold dust component is subject to large uncertainty (Lovell et al. 2021b), making the estimate of the dust production rate to be very uncertain as well. Therefore, this system was also discarded.

The data for the calculations were taken from Tables 1, 3, 4, and D.1. As before, in cases where no estimate of the width of the dust ring is available, or where the disk has so far only been resolved in scattered light, we assumed that $W_{\text{disk}} = 0.7 R_{\text{disk}}$. For debris disks whose excess spectrum requires two different temperature components to be properly modeled, we used the fractional luminosity of the cold components in the calculations. In the case of HD 145101, we used the derived upper limit of

$R_{\text{disk}} < 33$ au in the calculations, thereby also obtaining an upper limit for $\dot{M}_{\text{D}_{\text{min}}}$. For the sake of simplicity, for HD 152989 we adopted the R_{disk} and W_{disk} parameters derived from its Gaussian ring model.

As shown in the figure, the estimated CO masses exhibit a large spread of at least five orders of magnitude with a gap separating debris disks with low ($M_{\text{CO}} \lesssim 10^{-4} M_{\oplus}$) and high (CO-rich, $M_{\text{CO}} \gtrsim 10^{-3} M_{\oplus}$) CO content. It is worth noting here that for the latter group of disks the ^{12}CO line is probably optically thick and therefore their mass estimates are based on isotopolog measurements, which introduces a further uncertainty in the estimates due to the uncertain abundance ratios of the CO isotopologs. The large spread is evident for all $\dot{M}_{\text{D}_{\text{min}}}$. In debris disks with low CO content, in the absence of efficient shielding mechanism, the photodissociation lifetimes of CO molecules is limited to a few hundred years (Kral et al. 2017; Matrà et al. 2017a; Marino et al. 2022), so the long-term persistence of the gas disk requires continuous replenishment. Therefore, there is a general consensus that the gas in these systems, if present at all, is of secondary origin (Kral et al. 2017; Matrà et al. 2017a,b; Marino et al. 2020a). There are six disks in this subsample in which CO gas has already been detected: β Pic, HD 129590, HD 146897, HD 181327, HD 152989, and HD 170116 (marked by e, x, y, z, 5, and 8 in Fig. 8). With the exception of HD 181327, their estimated M_{CO} masses are between 10^{-5} and $10^{-4} M_{\oplus}$. All of these CO-bearing debris disks have $\dot{M}_{\text{D}_{\text{min}}} \gtrsim 0.38 M_{\oplus} \text{Myr}^{-1}$. Even if we discard those disks (including HD 181327 and HD 159595) that do not meet our detection limit criterion (Sect. 6.2), the CO detection rate for disks having $\dot{M}_{\text{D}_{\text{min}}} \gtrsim 0.38 M_{\oplus} \text{Myr}^{-1}$ is 5/7, while for disks with lower production rates it is 0/22. Using these results, the null hypothesis that the CO detection rates in the high and low dust production groups would be the same can be rejected on the basis of a Fisher's exact test which yielded a low probability of 1.8×10^{-4} . This suggests that collisions may play some role in CO gas production in the low CO content disks.

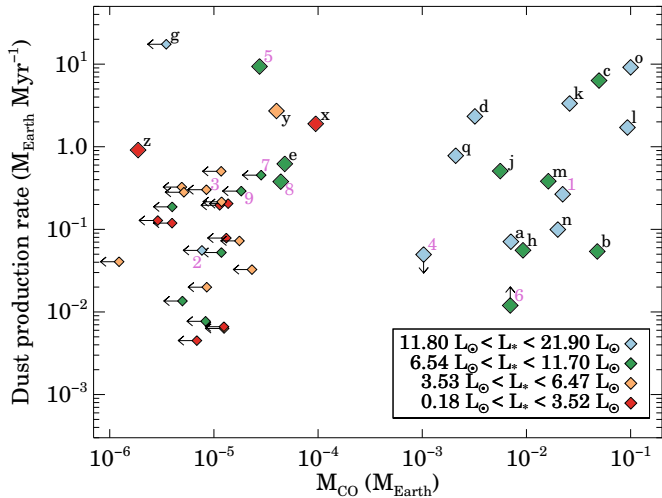


Fig. 8: Dust production rate as a function of the obtained CO masses. The different colors of the symbols correspond to the luminosity groups defined earlier in Sect. 6.2. The number and letter designations of the CO-bearing debris disks are the same as in Fig. 7. The three objects that were not included in that figure, HD 129590, HD 146897, and HD 181327, are labeled with the letters x, y, and z, respectively. For the HD 155853, we have only a lower limit for the f_d of the cold component (Appendix A.5), and hence also for the $\dot{M}_{\text{D}_{\text{min}}}$.

Both newly discovered low CO content gaseous debris disks show interesting structural features. For HD 152989, the ALMA observations hint at the presence of two gas-bearing dust rings with a gap between them, while the disk around HD 170116 is similar to the one around β Pic, not only in terms of CO mass and dust production rate, but also in the fact that the CO brightness distribution shows a significant asymmetry (Sect. 5.3 and Dent et al. 2014). Assuming that the ^{12}CO line is optically thin, which seems plausible, this implies that the mass distribution of the gas is also highly asymmetric. The nature of the bright CO clump observed in the disk of β Pic is still debated, it could either originate from a recent giant collision between Mars-sized bodies, from a tidal disruption event, or from collisions of planetesimals trapped in mean-motion resonance with a planet (Dent et al. 2014; Matrà et al. 2017a; Cataldi et al. 2018). The asymmetry is even more pronounced in HD 170116, where only one side of the disk shows detectable CO emission (Fig. 3). This CO disk also has a brighter clumpy part, which coincides well with the brightest part of the continuum dust emission. The possible scenarios to explain the observations here may be similar to those proposed for β Pic, but further detailed investigation of these is beyond the scope of this work. In any case, this suggests that in both disks there is a mechanism that produces CO gas on top of the collisional cascade, thereby increasing the steady state gas (and dust) content, albeit possibly only temporarily.

The presence and persistence of the observed large amounts of CO gas in CO-rich debris disks, which sometimes reach levels similar to those in protoplanetary disks, is only possible if some kind of shielding gas material exists in the system. The nature of this material and the observed gas component is still debated. It may be either second generation (see below) or residual primordial (Sect. 6.5). According to the shielded secondary gas disk model (Kral et al. 2019; Marino et al. 2020a), the high gas content of CO-rich systems can be explained if at some point during their evolution, due to a sufficiently high gas production rate, the emerging neutral carbon gas – mainly derived from the photodissociation of CO and CO_2 – becomes optically thick and can shield CO from UV photons. Together with the subsequent self-shielding of CO molecules, this process can prolong the photodissociation lifetime of CO significantly, allowing large gas masses to accumulate in such debris disks.

Assuming that both gas and dust originate from the collisions of icy solids, one might naively expect on the basis of this picture that CO-rich disks should tend to have a higher dust production rate than debris systems that do not harbor such massive gas disks. However, the observational results, as demonstrated by Fig. 8, do not support this expectation. The derived dust production rates for the CO-rich debris disks range between 0.01 and $9.2 M_{\oplus} \text{Myr}^{-1}$, while for the six gas-bearing disks with a low CO content are between 0.4 and $9.4 M_{\oplus} \text{Myr}^{-1}$. Thus, interestingly the two ranges significantly overlap, and the production rates for the former group is even slightly smaller on average ($1.7 M_{\oplus} \text{Myr}^{-1}$ versus $2.6 M_{\oplus} \text{Myr}^{-1}$). Even if we focus only on the CO-rich subsample, we see no correlation between $\dot{M}_{\text{D}_{\text{min}}}$ and M_{CO} . We note that, based on a smaller sample of gas-rich debris disks, Cataldi et al. (2023) also found no correlation between the predicted $\text{CO} + \text{CO}_2$ production rates and the measured CO masses. Marino et al. (2020a) found that the timescale of the viscous evolution of the gas can be longer than that of the evolution of the collisional cascade. This means that the massive gas component can persist for a long time after the dust (and gas) production rate of the cascade has dropped, i.e. it is possible that the decline of the gas disk follows the decline of the dust disk with a significant delay. So if we are interested in the formation

and evolution of CO-rich disks, then the past collisional mass loss should be taken into account, which could be much higher than the present one. This could even open up the possibility that there was a period in the early evolution of CO-rich disks when, for some reasons (e.g. a dynamic instability), the rate of dust and gas production increased peculiarly, allowing the formation of a CO-rich environment. The question is, whether this possible decoupling of the evolution of the dust and gas components is sufficient in itself to explain why the observed amount of CO does not depend on the mass loss rate of solids.

Another possible solution to this issue is that the ratio of the gas to dust production rates tends to be higher in the CO-rich systems, e.g. because the abundances of CO/CO₂ ice in their planetesimals are higher, and/or because other, possibly more efficient, outgassing mechanisms are at work in addition to collisions. The heating of icy planetesimals, either by stellar irradiation or by the decay of radioactive nuclides, can result in the release of gas (Davidsson 2021; Kral et al. 2021). Examples where sublimation induced by stellar irradiation may contribute to the CO production, at least in the inner parts of the disks, are HD 110058 and HD 145101 (see above), which are among the CO-rich debris systems with the lowest $M_{D_{\min}}$. The release of gas by radiogenic heating can be significant in the first ~ 30 Myr, but mostly only if large bodies of hundreds of kilometers in size are present in the planetesimal population (Davidsson 2021; Bonsor et al. 2023). This could suggest that CO-rich disks are systems where the planetesimals have become larger for some reason. However, these are among the brightest debris disks, where, if the maximum planetesimal size were so large, the solid matter content would significantly exceed the amount of material observed to be available in protoplanetary disks, suggesting that in these systems, especially in the outer zones, the planetesimals are instead small (Krivov & Wyatt 2021; Bonsor et al. 2023). Thus, despite the possible scenarios outlined above, questions remain as to why CO-rich disks can form in some systems but not in others at the same dust production rate, and why this phenomenon is restricted to disks around higher luminosity A-type stars.

6.5. Residual gas from the primordial disk phase?

A possible alternative explanation is that the gas in CO-rich debris disks, or at least some of them, is residual material from the previous protoplanetary phase. In fact, already after the discovery of the first CO-rich disks – motivated by their young age – it was proposed that the observed CO is only a small fraction of the gas material, which is predominantly composed of primordial H₂ gas that could significantly extend the photodissociation lifetime of CO molecules by efficiently shielding them from UV radiation (Kóspál et al. 2013; Péricaud et al. 2017). Since the dust component of these systems is of secondary origin, this scenario assumes a disk of hybrid nature (Kóspál et al. 2013). It should be noted that, although H₂ is primordial in this model, the observed CO gas is not necessarily, and secondary processes may play a role or even dominate its formation. Although most of the CO-rich disks have ages between 10 and 20 Myr (Fig. 9), at least three objects, including the newly discovered HD 9985, have been identified that are probably older than 30 Myr. A key question for the viability of the hybrid disk scenario is whether a primordial gas disk around an A-type star can survive to such old ages.

We note that although Herbig Ae disks typically disperse on a timescale of a few million years (Brittain et al. 2023; Pfalzner et al. 2022), we know of some that are older than

10 Myr (e.g., Arun et al. 2019; Wichittanakom et al. 2020) so their age distribution overlaps with that of the youngest CO-rich debris disks. These disks, however, are very different from the ones we have studied: though there is also an overlap in the CO content between the least gas-rich Herbig Ae disks and the most gas-rich debris disks, the dust content is orders of magnitude higher in the former systems providing additional very efficient shielding to not only CO but other molecules as well. Because of this latter effect, there may be a significant difference in the composition of the gas, and thus in the molecules that can be detected in the two types of disks (Klusmeyer et al. 2021; Smirnov-Pinchukov et al. 2022).

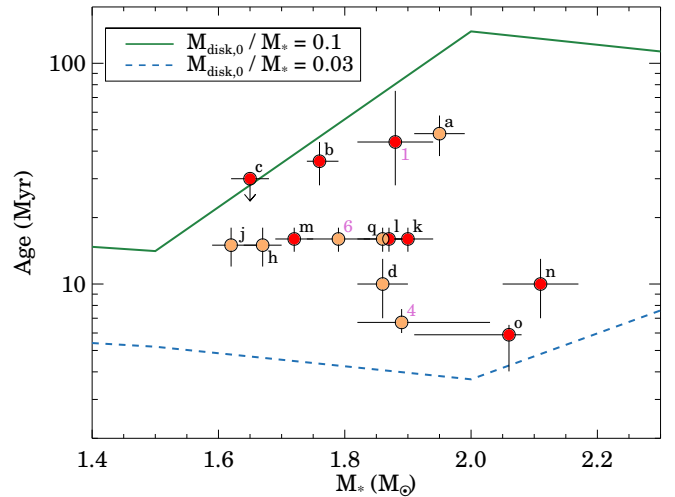


Fig. 9: Age as a function of stellar mass for known CO-rich debris systems. As in Fig. 7, the red symbols indicate disks with estimated CO masses $> 0.01 M_{\oplus}$, while the orange ones represent disks with M_{CO} between 0.001 and $0.01 M_{\oplus}$. The labels of the disks (numbers or letters) are also the same as in Fig. 7. The solid green and dashed blue curves show the lifetimes of primordial gas in disks depleted in submicron size dust particles assuming initial disk masses of $M_{disk,0} = 0.1 M_{*}$ and $M_{disk,0} = 0.03 M_{*}$, respectively. The curves are taken from Ooyama et al. (2025).

To assess the potential lifetime of primordial disks around stars of different masses, Nakatani et al. (2023) used a semi-analytic 0D disk evolution model and found that protoplanetary disks depleted in submicron dust particles and PAHs can persist for tens of millions of years around intermediate-mass stars, as the lack of small grains leads to much slower far-UV photoevaporation. By extending this model using 1D disk evolution simulations, Ooyama et al. (2025) further investigated this question. In Fig. 9 the solid green curve shows the lifetimes of primordial gas disks as a function of stellar masses in their fiducial model where they assumed initial disk masses of $M_{disk,0} = 0.1 M_{*}$ (for further default parameters of the fiducial model, see Ooyama et al. 2025). As the figure shows, according to this model, primordial gas can persist even up to ~ 140 Myr around a $2 M_{\odot}$ star, and the predicted maximum disk lifetimes exceed the age of the known CO-rich debris systems. Ooyama et al. (2025) also found that by assuming smaller initial disk masses ($M_{disk,0} = 0.03 M_{*}$), the predicted lifetime of the primordial gas is dramatically reduced (blue dashed curve), well below the age of the known systems. These results suggest that the gas in CO-rich systems could be of primordial origin, and if so, they may be the descendants of the most massive protoplanetary disks.

Table 5: Stirring of spatially resolved debris disks in our sample.

Target name	$M_{\text{disk, self-stir}}$ (M_{\oplus})	$M_{\text{pl, stir}}$ (M_{Jup})
HD 9985	600^{+200}_{-300}	$0.10^{+0.11}_{-0.13}$
HD 112532	40^{+40}_{-40}	$0.04^{+0.13}_{-0.13}$
HD 141960	100^{+100}_{-100}	$0.07^{+0.14}_{-0.14}$
HD 152989 ^a	2100^{+400}_{-400}	$0.13^{+0.06}_{-0.06}$
HD 152989 ^b	2000^{+600}_{-600}	$0.10^{+0.08}_{-0.08}$
HD 155853	3000^{+600}_{-600}	$1.63^{+1.07}_{-1.07}$
HD 159595	800^{+300}_{-200}	$0.37^{+0.34}_{-0.32}$
HD 170116	11000^{+4000}_{-4000}	$0.58^{+0.49}_{-0.50}$
HD 176497	600^{+400}_{-400}	$0.17^{+0.30}_{-0.30}$

Notes. Minimum disk mass ($M_{\text{disk, self-stir}}$) and minimum planet mass ($M_{\text{pl, stir}}$) required to excite the disk by self-stirring or secular stirring by an eccentric planet over the life of the system (for details see Sect. 6.6). In the case of HD 152989, both available continuum models (a: Gaussian ring; b: double ring) were considered in the calculations.

6.6. Dynamical excitation of the disks

For collisions between planetesimals to result in their erosion and eventual dust production through a collision cascade, the relative velocity of the bodies must be sufficiently high, which requires dynamical excitation of the disk (Wyatt 2008). Assuming that the disk has not been prestirred in some way since its birth, some mechanism is required to initiate and maintain an excited population of planetesimals. This may be the gravitational influence of the largest planetesimals embedded in the disk (self-stirring, Kenyon & Bromley 2004; Krivov & Booth 2018) or perturbation from a planet or stellar companion present in the system (Mustill & Wyatt 2009), and in some cases stellar flybys may also play a role (Kenyon & Bromley 2002). Knowing some basic properties of the central star and the planetesimal belt, it is possible, under certain assumptions, to estimate a minimum disk mass that would be required to excite the disk by self-stirring over the lifetime of the system (Pearce et al. 2022). We used the `MinSelfStirringDiscMass`⁷ python script developed by Pearce et al. (2022) to compute this parameter for all disks from our sample whose continuum emission was spatially resolved. The required input parameters are: the mass and age of the star and the radii of the inner and outer edges of the planetesimal belt (assuming that the disk is axisymmetric) and the measured dust mass (from which the total disk mass is estimated). The stellar parameters and their uncertainties are taken from Table 1. Since those large particles that dominate the observed millimeter-wavelength emission are negligibly affected by the radiative forces, their spatial distribution is supposed to follow that of the parent bodies. Therefore, in the calculations we have assumed that the planetesimal belts' inner and outer edge radii equal to $R_{\text{disk}} - 0.5W_{\text{disk}}$ and $R_{\text{disk}} + 0.5W_{\text{disk}}$, respectively (Table 3). For HD 112532, HD 141960, and HD 176497, where we had no estimate for the disk width from the measurements, we adopted $W_{\text{disk}} = 0.7R_{\text{disk}}$. For HD 152989, both the Gaussian ring and the double ring models were considered, in the latter case utilizing the radii of the inner and outer ring as the inner and outer edges of the disk. The dust mass estimates of the disks were taken from Table 3.

The resulting minimum disk masses, which range from 40 to $11\,000 M_{\oplus}$ are given in Table 5. A disk mass greater than $1000 M_{\oplus}$ is unlikely, as this would exceed the observed amount of solid material in protoplanetary disks (Krivov & Wyatt 2021; Pearce et al. 2022). Self-stirring alone therefore is likely not a viable excitation mechanism for debris disks around HD 152989, HD 155853, and for HD 170116. It is worth considering, however, that there are still questions regarding the total mass of solids in protoplanetary disks (e.g., Liu et al. 2022; Viscardi et al. 2025), and the real uncertainties of the disks' dust mass estimates used as input data in the calculations can even significantly exceed the derived formal ones (Sect. 4.3), meaning that this conclusion should be treated with caution. A possible alternative is that the disk stirring is caused by the secular perturbation of an unseen, eccentric planet orbiting inside the disk (Mustill & Wyatt 2009). Using eq. 23 from Pearce et al. (2022), we can estimate the minimum mass of the planet ($M_{\text{pl, stir}}$) that can excite the planetesimal population on a timescale shorter than the age of the system. This minimum value is calculated for all systems in Table 5, assuming, similarly to Pearce et al. (2022), that the eccentricity of the possible planet is 0.3. As the table shows, in most cases a relatively low mass planet is sufficient for the excitation, the only system that would require a planet with $>1 M_{\text{Jup}}$ is HD 155853. However, this calculation assumes a massless disk. If the self-gravity of the disk is taken into account, and if the mass of the disk exceeds that of the planet, the secular perturbation effect will be weaker, and a more massive planet than the ones inferred from the above approach is required for the sufficient excitation (Sefilian 2024). It is worth noting that several other avenues of planetary stirring have recently been proposed. Resonance sweeping accompanied with the migration of a planet can excite the disk material igniting more violent, higher velocity collisions (Friebe et al. 2022). Costa et al. (2024) argue that massive projectiles scattered by a planet orbiting at the inner edge of the disk can also stir the orbit of other planetesimals. They also found that sufficiently massive planets ($\gtrsim 0.5 M_{\text{Jup}}$) can excite a disk via broad mean motion resonances. Finally, the combination of self-stirring and the secular perturbation of a planet can be significantly more efficient than considering these mechanisms separately (Muñoz-Gutiérrez et al. 2023).

Thus, by investigating the possible dynamical excitation of our disks, we found that self-stirring is highly unlikely in at least three debris disks, HD 152989, HD 155853, and HD 170116, and that for these systems, other mechanisms, most likely planetary stirring is required for the collision cascade to work. If debris material of the HD 152989 system is indeed concentrated in two rings, this could be another strong indication of the presence of a planet in the gap between them, which would also explain how this disk is stirred. Such gaps, potentially carved by planets, have already been detected in several wide outer debris disks through mm continuum observations with high spatial resolution (Marino et al. 2018, 2019, 2020b; MacGregor et al. 2019; Nederlander et al. 2021). We note that those gaps may also be present in the gas distribution and observable with ALMA for massive enough planets, as recently shown in Bergez-Casalou & Kral (2024). It is worth mentioning that HD 152989 has a wide, relatively massive companion (Appendix A.2), which, if its orbit is sufficiently eccentric, could also contribute to the dynamical excitation of the planetesimals. These findings make these three systems promising targets for future planet search programs.

⁷ <https://www.tdpearce.uk/public-code/>

7. Summary and Conclusions

Aiming to study the presence and evolution of gas in young dust-rich debris disks around intermediate-mass stars, we have carried out Band 6 continuum and CO line observations with ALMA toward 12 systems that show strong excess emission based on their previous IR observations. The selected systems have received little or no attention so far, and our program has provided their first subarcsecond angular resolution measurements at millimeter wavelengths. We detected mm continuum emission from nine of our targets, and resolved the debris disk at least marginally in eight of them. In addition, we discovered CO gas in five disks. In two of them, HD 152989 and HD 170116, only emission from the most abundant main isotopolog ^{12}CO was detected. In the other three, HD 145101, HD 9985, and HD 155853, emission of ^{13}CO gas was also detected, and in the latter two even the presence of the much rarer C^{18}O isotopolog was revealed. From the continuum and CO line measurements, we estimated the dust and gas masses of the disks and examined the radial distribution of dust and gas. In addition to these results, we also detected both continuum and CO line emission from the HD 31305 system, but these detections are not associated with the targeted very young A-type star, but with a disk of its late-type companion, which is probably of protoplanetary origin.

While the CO content of the disks around HD 152989 and HD 170116 is $<10^{-4} \text{ M}_\oplus$, the other three gas-bearing systems, HD 9985, HD 145101, and HD 155853, have CO masses $>10^{-3} \text{ M}_\oplus$, and are therefore classified as CO-rich debris disks. While the gas in the disks with low CO content is most likely of secondary origin, for the CO-rich objects a primordial origin may be a possible alternative.

The debris disk around HD 152989, despite its outstandingly high fractional luminosity of $\sim 7 \times 10^{-3}$, was unknown before our study. The position-velocity diagram of ^{12}CO emission suggests that there is a gap in the radial distribution of the gas disk: the bulk of the CO is in two rings at radial distances of ~ 75 au and ~ 130 au. Based on the continuum data modeling, the distribution of large dust particles can also be described by a consistent two-ring model, but the solution is not unique. If this disk does indeed show such a gapped structure – further higher spatial resolution, deeper ALMA measurements are needed to prove this – then it is unique among known CO-bearing debris disks.

The debris disk of HD 170116 is one of the most distant that has ever been spatially resolved with ALMA. The disk has a peak radius of ~ 200 au, which makes it one of the largest known debris disks (cf. the REASONS sample Matrà et al. 2025). The spatial distribution of the relatively small amount of CO gas is highly asymmetric, with the detectable emission associated only with one side of the disk and showing a CO brightness peak located close to the inner edge of the dust disk. How this high degree of asymmetry has developed is not yet clear. However, the similarity of this feature to the disk around β Pic raises the possibility that a transient gas- and dust-producing event or a resonant planetary population may be behind the phenomenon (Matrà et al. 2017a; Cataldi et al. 2018).

Of our sample, the debris disk around HD 9985 is the most CO-rich with an estimated CO mass of $\sim 0.02 \text{ M}_\oplus$. In many ways, this system resembles the previously discovered CO-rich debris system, HD 121617 (Moór et al. 2017; Cataldi et al. 2023). The host stars have very similar luminosities, the gas and dust material is well co-located, the radial positions (84 ± 5 au for HD 9985 and 78 ± 5 au for HD 121617, see Table 3 and Matrà et al. 2025) as well as the fractional widths of the debris rings (0.68 ± 0.31 for HD 9985 and 0.77 ± 0.14 for HD 121617, see Table 3 and

Matrà et al. 2025) are also quite similar to each other. Based on its estimated age of 44_{-16}^{+31} Myr, HD 9985, along with 49 Cet and HD 21997, is likely the oldest of the known CO-rich debris disks.

The continuum observations of HD 155853 reveal a broad dust belt extending from 60 to 175 au. The disk is CO-rich, but unlike the case of HD 9985, the spatial distribution of the gas component is different from that of the large dust grains, the former showing a more compact morphology. This feature makes this disk more akin to the CO-rich debris disks found around HD 21997 and HD 131488 (Kóspál et al. 2013; Pawellek et al. 2024), whose gas and dust components are also not well co-located. Both the abovementioned HD 152989 and HD 155853 are the members of the UCL association, which has proven to be the richest reservoir of CO-bearing debris disks to date, with 7 of such objects identified so far in this group.

HD 145101 is a young (~ 7 Myr), intermediate mass pre-main-sequence star that belongs to the US association. While in the vast majority of the young CO-bearing debris disks identified so far, including the 4 newly discovered ones above, the bulk of the gas and dust is located at radial distances larger than 40 au, the disk around HD 145101 is quite compact, with both components predominantly situated at < 33 au. Consistently, the analysis of the SED also indicates a rather high characteristic dust temperature of ~ 160 K. In this respect, this disk is more similar to the one around HD 172555 (Su et al. 2020; Schneiderman et al. 2021), which also contains warm dust only. However, the CO content of HD 145101 is two orders of magnitude higher. If the gas is of secondary origin, it is possible that thanks to the higher temperature environment, thermal desorption of ices may play a larger role in the gas release than in the other known CO-bearing debris systems.

In a future paper, we plan for a more detailed analysis of the origin and evolution of gas in these five systems by taking into account the production and the subsequent photodissociation, shielding, and viscous evolution of the CO gas.

By investigating the possible dynamical excitation of those debris disks from our sample that are spatially resolved in the continuum, we found that self-stirring of HD 152989, HD 155853, and HD 170116 would require unreasonably large disk masses suggesting that their excitation is instead related to an unseen planet(s) or a companion. These systems could be promising targets for future planet search programs.

To study the general characteristics of young (≤ 50 Myr), dust-rich ($f_d > 5 \times 10^{-4}$) CO-bearing debris disks and the environments in which they form, we combined our new results with data from the literature. In agreement with previous results (Lieman-Sifry et al. 2016; Moór et al. 2017), we found that the occurrence rate of CO gas rises significantly for disks surrounding host stars with $L_* > 6.5 \text{ L}_\odot$, corresponding to spectral types earlier than $\sim \text{A8}$. While in disks around stars with a luminosity lower than this value, the detection rate is 3/26 (12%), in systems with higher luminosity hosts it is 18/26 (69%). While none of the gas-bearing disks in the former subgroup are CO-rich, the latter contains 15 such objects. Interestingly, all the 9 gaseous disks around stars with luminosities from 13.2 to 21.9 L_\odot (A4–A0) are CO-rich. If we consider only the disks with $f_d > 10^{-3}$ in the higher stellar luminosity subsample, the CO detection rate is 15/18, i.e. these two easily measured parameters together provide a good indicator of the presence of CO gas in young debris systems.

There is a general consensus that the gas in debris disks with CO masses of $< 10^{-4} \text{ M}_\oplus$ is derived from the erosion of planetesimals, similar to dust. By comparing the estimated CO content and the mass loss rate of the solids in such disks – the lat-

ter parameter is estimated by assuming an ideal collision cascade – we found that the detected gas-bearing systems belong to the ones with the highest mass loss rates. This is an indication that collisions, in line with model predictions (Kral et al. 2017), may play a role in gas production in debris disks with low CO content. According to the recently developed shielded secondary gas disk model (Kral et al. 2019; Marino et al. 2020a), even the large gas content of the CO-rich debris disks can be explained by second generation processes. Interestingly, when comparing low CO content and CO-rich disks, we do not see a significant difference in the estimated dust mass loss rates, and when looking only at the latter disks, we see no correlation between CO content and mass loss. This raises the question of what could be the difference that, at similar dust mass loss rates, lead to a CO-rich state in some of the debris disks but not in others. In addition to the possible explanation that the current dust mass loss rates do not reflect those characterising the initial stage of the CO-rich disks, due to the gas lifetime far exceeding the evolution of the collision cascade (Marino et al. 2020a), we also raise the possibility that in these particular systems the abundance of CO ices in the planetesimals may have been higher and/or other more efficient gas release mechanisms may have been active in addition to collisions. Alternatively, as Nakatani et al. (2023) and Ooyama et al. (2025) have shown, the CO-rich phenomenon can also be explained by that, under certain conditions, the gas material of massive protoplanetary disks depleted in small grains can persist for much longer than previously thought. By comparing the predictions of the latest model with the ages of known CO-rich disks, we found that for all of them it is conceivable that the gas is dominantly made by residual primordial material. Thus, the origin of the gas in CO-rich disks still remains an open question.

Acknowledgements. We thank the anonymous referee for their useful suggestions. We are grateful to W. Ooyama for sending us their modeling data on the lifetimes of primordial gas disks as a function of stellar mass. This paper makes use of the following ALMA data: ADS/JAO.ALMA#2021.1.01487.S. ALMA is a partnership of ESO (representing its member states), NSF (USA) and NINS (Japan), together with NRC (Canada), NSTC and ASIAA (Taiwan), and KASI (Republic of Korea), in cooperation with the Republic of Chile. The Joint ALMA Observatory is operated by ESO, AUI/NRAO and NAOJ. This work presents results from the European Space Agency (ESA) space mission Gaia. Gaia data are being processed by the Gaia Data Processing and Analysis Consortium (DPAC). Funding for the DPAC is provided by national institutions, in particular the institutions participating in the Gaia MultiLateral Agreement (MLA). The Gaia mission website is <https://www.cosmos.esa.int/gaia>. The Gaia archive website is <https://archives.esac.esa.int/gaia>. Funding for the DPAC has been provided by national institutions, in particular, the institutions participating in the Gaia Multilateral Agreement. This research has made use of the VizieR catalogue access tool, CDS, Strasbourg, France (DOI: 10.26093/cds/vizier). The original description of the VizieR service was published in A&AS 143, 23. AMH gratefully acknowledges support from the National Science Foundation through Grant No. AST-2307920.

References

Agresti, A. & Coull, B. 1998, *The American Statistician*, 52, 119

Andrews, S. M., Rosenfeld, K. A., Kraus, A. L., & Wilner, D. J. 2013, *ApJ*, 771, 129

Arun, R., Mathew, B., Manoj, P., et al. 2019, *AJ*, 157, 159

Aumann, H. H., Gillett, F. C., Beichman, C. A., et al. 1984, *ApJ*, 278, L23

Bailer-Jones, C. A. L., Rybizki, J., Fouesneau, M., Demleitner, M., & Andrae, R. 2021, *AJ*, 161, 147

Ballerina, N. P., Rieke, G. H., Su, K. Y. L., & Montiel, E. 2013, *ApJ*, 775, 55

Balog, Z., Müller, T., Nielbock, M., et al. 2014, *Experimental Astronomy*, 37, 129

Belokurov, V., Penoyre, Z., Oh, S., et al. 2020, *MNRAS*, 496, 1922

Bendahan-West, R., Kennedy, G. M., Brown, D. J. A., & Strøm, P. A. 2025, *MNRAS*, 537, 229

Bergez-Casalou, C. & Kral, Q. 2024, *A&A*, 692, A156

Bhowmik, T., Boccaletti, A., Thébault, P., et al. 2019, *A&A*, 630, A85

Binks, A. S., Jeffries, R. D., & Maxted, P. F. L. 2015, *MNRAS*, 452, 173

Binks, A. S., Jeffries, R. D., & Ward, J. L. 2018, *MNRAS*, 473, 2465

Binks, A. S., Jeffries, R. D., & Wright, N. J. 2020, *MNRAS*, 494, 2429

Blaauw, A. 1964, *ARA&A*, 2, 213

Bockelée-Morvan, D. & Biver, N. 2017, *Philosophical Transactions of the Royal Society of London Series A*, 375, 20160252

Boller, T., Freyberg, M. J., Trümper, J., et al. 2016, *A&A*, 588, A103

Bonsor, A., Wyatt, M. C., Marino, S., et al. 2023, *MNRAS*, 526, 3115

Bouma, L. G., Palumbo, E. K., & Hillenbrand, L. A. 2023, *ApJ*, 947, L3

Brandt, T. D. 2021, *ApJS*, 254, 42

Brennan, A., Matrà, L., Marino, S., et al. 2024, *MNRAS*, 531, 4482

Brittain, S. D., Kamp, I., Meeus, G., Oudmaijer, R. D., & Waters, L. B. F. M. 2023, *Space Sci. Rev.*, 219, 7

Bryson, S., Coughlin, J., Batalha, N. M., et al. 2020, *AJ*, 159, 279

Capitanio, L., Lallement, R., Vergely, J. L., Elyajouri, M., & Montreal-Ibero, A. 2017, *A&A*, 606, A65

Castelli, F. & Kurucz, R. L. 2004, *ArXiv Astrophysics e-prints* [[astro-ph/0405087](https://arxiv.org/abs/astro-ph/0405087)]

Cataldi, G., Aikawa, Y., Iwasaki, K., et al. 2023, *ApJ*, 951, 111

Cataldi, G., Brandeker, A., Wu, Y., et al. 2018, *ApJ*, 861, 72

Cataldi, G., Wu, Y., Brandeker, A., et al. 2020, *ApJ*, 892, 99

Chen, C. H., Mittal, T., Kuchner, M., et al. 2014, *ApJS*, 211, 25

Choi, J., Dotter, A., Conroy, C., et al. 2016, *ApJ*, 823, 102

Clark, F. O. 1991, *ApJS*, 75, 611

Cody, A. M., Tayar, J., Hillenbrand, L. A., Matthews, J. M., & Kallinger, T. 2013, *AJ*, 145, 79

Collings, M. P., Anderson, M. A., Chen, R., et al. 2004, *MNRAS*, 354, 1133

Collings, M. P., Dever, J. W., Fraser, H. J., McCoustra, M. R. S., & Williams, D. A. 2003, *ApJ*, 583, 1058

Costa, T., Pearce, T. D., & Krivov, A. V. 2024, *MNRAS*, 527, 7317

Cotten, T. H. & Song, I. 2016, *ApJS*, 225, 15

Cutri, R. M. & et al. 2014, *VizieR Online Data Catalog*, II/328

Cutri, R. M., Skrutskie, M. F., van Dyk, S., et al. 2003, *VizieR Online Data Catalog*, 2246

Davidson-Pilon, C. 2019, *Journal of Open Source Software*, 4, 1317

Davidsson, B. J. R. 2021, *MNRAS*, 505, 5654

Deacon, N. R. & Kraus, A. L. 2020, *MNRAS*, 496, 5176

Dent, W. R. F., Wyatt, M. C., Roberge, A., et al. 2014, *Science*, 343, 1490

Di Folco, E., Péricaud, J., Dutrey, A., et al. 2020, *A&A*, 635, A94

Dommangé, J. & Nys, O. 2002, *VizieR Online Data Catalog*, I/274

Dotter, A. 2016, *ApJS*, 222, 8

El-Badry, K. & Rix, H.-W. 2018, *MNRAS*, 480, 4884

Fazio, G. G.,Hora, J. L., Allen, L. E., et al. 2004, *ApJS*, 154, 10

Ferlet, R., Hobbs, L. M., & Vidal-Madjar, A. 1987, *A&A*, 185, 267

Flaherty, K. M., Hughes, A. M., Andrews, S. M., et al. 2016, *ApJ*, 818, 97

Fribe, M. F., Pearce, T. D., & Löhne, T. 2022, *MNRAS*, 512, 4441

Gagné, J. & Faherty, J. K. 2018, *ApJ*, 862, 138

Gagné, J., Faherty, J. K., Moranta, L., & Popinchalk, M. 2021, *ApJ*, 915, L29

Gagné, J., Mamajek, E. E., Malo, L., et al. 2018, *ApJ*, 856, 23

Gaia Collaboration, Brown, A. G. A., Vallenari, A., et al. 2018, *A&A*, 616, A1

Gaia Collaboration, Vallenari, A., Brown, A. G. A., et al. 2023, *A&A*, 674, A1

Galli, P. A. B., Bouy, H., Olivares, J., et al. 2020, *A&A*, 634, A98

Goldman, B., Röser, S., Schilbach, E., Moór, A. C., & Henning, T. 2018, *ApJ*, 868, 32

Gontcharov, G. A. 2006, *Astronomy Letters*, 32, 759

Gratton, R., Bonavita, M., Mesa, D., et al. 2024, *A&A*, 685, A119

Greaves, J. S., Holland, W. S., Matthews, B. C., et al. 2016, *MNRAS*, 461, 3910

Hales, A. S., Marino, S., Sheehan, P. D., et al. 2022, *ApJ*, 940, 161

Hardy, A., Caceres, C., Schreiber, M. R., et al. 2015, *A&A*, 583, A66

Hauschildt, P. H., Allard, F., & Baron, E. 1999, *ApJ*, 512, 377

Heays, A. N., Bosman, A. D., & van Dishoeck, E. F. 2017, *A&A*, 602, A105

Henden, A. A., Templeton, M., Terrell, D., et al. 2016, *VizieR Online Data Catalog*, 2336

Higuchi, A. E., Kóspál, Á., Moór, A., Nomura, H., & Yamamoto, S. 2020, *ApJ*, 905, 122

Hinkley, S., Matthews, E. C., Lefevre, C., et al. 2021, *ApJ*, 912, 115

Høg, E., Fabricius, C., Makarov, V. V., et al. 2000, *A&A*, 357, 367

Hom, J., Patience, J., Esposito, T. M., et al. 2020, *AJ*, 159, 31

Hoogerwerf, R. 2000, *MNRAS*, 313, 43

Hughes, A. M., Duchêne, G., & Matthews, B. C. 2018, *ARA&A*, 56, 541

Iglesias, D., Bayo, A., Olofsson, J., et al. 2018, *MNRAS*, 480, 488

Ishihara, D., Onaka, T., Kataza, H., et al. 2010, *A&A*, 514, A1

Jeffries, R. D., Jackson, R. J., Wright, N. J., et al. 2023, *MNRAS*, 523, 802

Kalas, P. 2005, *ApJ*, 635, L169

Kennedy, G. M., Marino, S., Matrà, L., et al. 2018, *MNRAS*, 475, 4924

Kennedy, G. M., Murphy, S. J., Lisse, C. M., et al. 2014, *MNRAS*, 438, 3299

Kenyon, S. J. & Bromley, B. C. 2002, *AJ*, 123, 1757

Kenyon, S. J. & Bromley, B. C. 2004, *AJ*, 127, 513

Kervella, P., Arenou, F., & Thévenin, F. 2022, *A&A*, 657, A7

Kiefer, F., Lecavelier des Etangs, A., Augereau, J. C., et al. 2014, *A&A*, 561, L10

Klusmeyer, J., Hughes, A. M., Matrà, L., et al. 2021, *ApJ*, 921, 56

Kóspál, Á., Moór, A., Juhász, A., et al. 2013, *ApJ*, 776, 77

Kral, Q., Davout, J., & Charnay, B. 2020a, *Nature Astronomy*, 4, 769

Kral, Q., Marino, S., Wyatt, M. C., Kama, M., & Matrà, L. 2019, *MNRAS*, 489, 3670

Kral, Q., Matrà, L., Kennedy, G. M., Marino, S., & Wyatt, M. C. 2020b, *MNRAS*, 497, 2811

Kral, Q., Matrà, L., Wyatt, M. C., & Kennedy, G. M. 2017, *MNRAS*, 469, 521

Kral, Q., Pringle, J. E., Guilbert-Lepoutre, A., et al. 2021, *A&A*, 653, L11

Krivov, A. V. 2010, *Research in Astronomy and Astrophysics*, 10, 383

Krivov, A. V. & Booth, M. 2018, *MNRAS*, 479, 3300

Krivov, A. V. & Wyatt, M. C. 2021, *MNRAS*, 500, 718

Lacour, S., Wang, J. J., Rodet, L., et al. 2021, *A&A*, 654, L2

Lada, C. J. 1987, in *IAU Symposium*, Vol. 115, *Star Forming Regions*, ed. M. Peimbert & J. Jugaku, 1

Lallement, R., Capitanio, L., Ruiz-Dern, L., et al. 2018, *A&A*, 616, A132

Lallement, R., Vergely, J.-L., Valette, B., et al. 2014, *A&A*, 561, A91

Lieman-Sifry, J., Hughes, A. M., Carpenter, J. M., et al. 2016, *ApJ*, 828, 25

Lindgren, L., Hernández, J., Bombrun, A., et al. 2018, *A&A*, 616, A2

Lisse, C. M., Chen, C. H., Wyatt, M. C., et al. 2009, *ApJ*, 701, 2019

Lisse, C. M., Sitko, M. L., Russell, R. W., et al. 2017, *ApJ*, 840, L20

Liu, Y., Linz, H., Fang, M., et al. 2022, *A&A*, 668, A175

Lovell, J. B., Kennedy, G. M., Marino, S., et al. 2021a, *MNRAS*, 502, L66

Lovell, J. B., Wyatt, M. C., Ansdell, M., et al. 2021b, *MNRAS*, 500, 4878

Luhman, K. L. 2022, *AJ*, 163, 24

Luhman, K. L. 2023, *AJ*, 165, 37

Luhman, K. L., Herrmann, K. A., Mamajek, E. E., Esplin, T. L., & Pecaut, M. J. 2018, *AJ*, 156, 76

MacGregor, M. A., Weinberger, A. J., Hughes, A. M., et al. 2018, *ApJ*, 869, 75

MacGregor, M. A., Weinberger, A. J., Nesvold, E. R., et al. 2019, *ApJ*, 877, L32

Marino, S., Bonsor, A., Wyatt, M. C., & Kral, Q. 2018, *MNRAS*, 479, 1651

Marino, S., Cataldi, G., Jankovic, M. R., Matrà, L., & Wyatt, M. C. 2022, *MNRAS*, 515, 507

Marino, S., Flock, M., Henning, T., et al. 2020a, *MNRAS*, 492, 4409

Marino, S., Matrà, L., Stark, C., et al. 2016, *MNRAS*, 460, 2933

Marino, S., Yelverton, B., Booth, M., et al. 2019, *MNRAS*, 484, 1257

Marino, S., Zurlo, A., Faramaz, V., et al. 2020b, *MNRAS*, 498, 1319

Markwardt, C. B. 2009, in *Astronomical Society of the Pacific Conference Series*, Vol. 411, *Astronomical Data Analysis Software and Systems XVIII*, ed. D. A. Bohlander, D. Durand, & P. Dowler, 251

Marshall, J. P., Wang, L., Kennedy, G. M., Zeegers, S. T., & Scicluna, P. 2021, *MNRAS*, 501, 6168

Martí-Vidal, I., Vlemmings, W. H. T., Muller, S., & Casey, S. 2014, *A&A*, 563, A136

Martín-Doménech, R., Muñoz Caro, G. M., Bueno, J., & Goessmann, F. 2014, *A&A*, 564, A8

Marton, G., Calzolatti, L., Perez Garcia, A. M., et al. 2017, *arXiv e-prints*, arXiv:1705.05693

Mason, B. D., Wycoff, G. L., Hartkopf, W. I., Douglass, G. G., & Worley, C. E. 2001, *AJ*, 122, 3466

Matrà, L., Dent, W. R. F., Wyatt, M. C., et al. 2017a, *MNRAS*, 464, 1415

Matrà, L., MacGregor, M. A., Kalas, P., et al. 2017b, *ApJ*, 842, 9

Matrà, L., Marino, S., Kennedy, G. M., et al. 2018, *ApJ*, 859, 72

Matrà, L., Marino, S., Wilner, D. J., et al. 2025, *A&A*, 693, A151

Matrà, L., Panić, O., Wyatt, M. C., & Dent, W. R. F. 2015, *MNRAS*, 447, 3936

Matrà, L., Wyatt, M. C., Wilner, D. J., et al. 2019, *AJ*, 157, 135

McDonald, I., Zijlstra, A. A., & Boyer, M. L. 2012, *MNRAS*, 427, 343

McMullin, J. P., Waters, B., Schiebel, D., Young, W., & Golap, K. 2007, in *Astronomical Society of the Pacific Conference Series*, Vol. 376, *Astronomical Data Analysis Software and Systems XVI*, ed. R. A. Shaw, F. Hill, & D. J. Bell, 127

Meeus, G., Montesinos, B., Mendigutía, I., et al. 2012, *A&A*, 544, A78

Mooley, K., Hillenbrand, L., Rebull, L., Padgett, D., & Knapp, G. 2013, *ApJ*, 771, 110

Moór, A., Ábrahám, P., Juhász, A., et al. 2011a, *ApJ*, 740, L7

Moór, A., Ábrahám, P., Szabó, G., et al. 2021, *ApJ*, 910, 27

Moór, A., Curé, M., Kóspál, Á., et al. 2017, *ApJ*, 849, 123

Moór, A., Henning, T., Juhász, A., et al. 2015a, *ApJ*, 814, 42

Moór, A., Kóspál, Á., Ábrahám, P., et al. 2015b, *MNRAS*, 447, 577

Moór, A., Kóspál, Á., Ábrahám, P., et al. 2016, *ApJ*, 826, 123

Moór, A., Kral, Q., Ábrahám, P., et al. 2019, *ApJ*, 884, 108

Moór, A., Pascucci, I., Kóspál, Á., et al. 2011b, *ApJS*, 193, 4

Moór, A., Pawellek, N., Ábrahám, P., et al. 2020, *AJ*, 159, 288

Moranta, L., Gagné, J., Couture, D., & Faherty, J. K. 2022, *ApJ*, 939, 94

Moshir, M., Kopan, G., Conrow, T., et al. 1990, in *Bulletin of the American Astronomical Society*, Vol. 22, 1325

Muñoz-Gutiérrez, M. A., Marshall, J. P., & Peimbert, A. 2023, *MNRAS*, 520, 3218

Mumma, M. J. & Charnley, S. B. 2011, *ARA&A*, 49, 471

Mustill, A. J. & Wyatt, M. C. 2009, *MNRAS*, 399, 1403

Nakatani, R., Kobayashi, H., Kuiper, R., Nomura, H., & Aikawa, Y. 2021, *ApJ*, 915, 90

Nakatani, R., Turner, N. J., Hasegawa, Y., et al. 2023, *ApJ*, 959, L28

Nederlander, A., Hughes, A. M., Fehr, A. J., et al. 2021, *ApJ*, 917, 5

Oh, S., Price-Whelan, A. M., Hogg, D. W., Morton, T. D., & Spergel, D. N. 2017, *AJ*, 153, 257

Olofsson, J., Henning, T., Nielbock, M., et al. 2013, *A&A*, 551, A134

Ooyama, W., Nakatani, R., Hosokawa, T., Mitani, H., & Turner, N. J. 2025, *ApJ*, 983, 153

Paegert, M., Stassun, K. G., Collins, K. A., et al. 2021, *arXiv e-prints*, arXiv:2108.04778

Pascucci, I., Testi, L., Herczeg, G. J., et al. 2016, *ApJ*, 831, 125

Pawellek, N., Krivov, A. V., Marshall, J. P., et al. 2014, *ApJ*, 792, 65

Pawellek, N., Moór, A., Kirchschlager, F., et al. 2024, *MNRAS*, 527, 3559

Pawellek, N., Wyatt, M., Matrà, L., Kennedy, G., & Yelverton, B. 2021, *MNRAS*, 502, 5390

Pearce, T. D., Launhardt, R., Ostermann, R., et al. 2022, *A&A*, 659, A135

Pecaut, M. J. & Mamajek, E. E. 2013, *ApJS*, 208, 9

Péricaud, J., Di Folco, E., Dutrey, A., Guilloteau, S., & Piétu, V. 2017, *A&A*, 600, A62

Perryman, M. A. C. 1997, in *ESA Special Publication*, Vol. 402, *Hipparcos - Venice '97*, ed. R. M. Bonnet, E. Høg, P. L. Bernacca, L. Emiliani, A. Blaauw, C. Turon, J. Kovalevsky, L. Lindegren, H. Hassan, M. Bouffard, B. Strim, D. Heger, M. A. C. Perryman, & L. Wolter, 1-4

Pfalzner, S., Dehghan, S., & Michel, A. 2022, *ApJ*, 939, L10

Poglitsch, A., Waelkens, C., Geis, N., et al. 2010, *A&A*, 518, L2

Potravnov, I. S., Grinin, V. P., & Serebriakova, N. A. 2019, *A&A*, 630, A64

Punzi, K. M., Kastner, J. H., Melis, C., et al. 2018, *AJ*, 155, 33

Ratzenböck, S., Großschedl, J. E., Alves, J., et al. 2023a, *A&A*, 678, A71

Ratzenböck, S., Großschedl, J. E., Möller, T., et al. 2023b, *A&A*, 677, A59

Rebollido, I., Eiroa, C., Montesinos, B., et al. 2020, *A&A*, 639, A11

Rebollido, I., Ribas, A., de Gregorio-Monsalvo, I., et al. 2022, *MNRAS*, 509, 693

Rhee, J. H., Song, I., Zuckerman, B., & McElwain, M. 2007, *ApJ*, 660, 1556

Rieke, G. H., Young, E. T., Engelbracht, C. W., et al. 2004, *ApJS*, 154, 25

Riello, M., De Angeli, F., Evans, D. W., et al. 2021, *A&A*, 649, A3

Riviere-Marichalar, P., Barrado, D., Augereau, J. C., et al. 2012, *A&A*, 546, L8

Riviere-Marichalar, P., Barrado, D., Montesinos, B., et al. 2014, *A&A*, 565, A68

Roberge, A., Kamp, I., Montesinos, B., et al. 2013, *ApJ*, 771, 69

Rodet, L., Beust, H., Bonnefoy, M., et al. 2017, *A&A*, 602, A12

Samland, M., Henning, T., Caratti o Garatti, A., et al. 2025, *ApJ*, 989, 132

Schneiderman, T., Matrà, L., Jackson, A. P., et al. 2021, *Nature*, 598, 425

Sefilian, A. A. 2024, *ApJ*, 966, 140

Singh, G., Bhowmik, T., Boccaletti, A., et al. 2021, *A&A*, 653, A79

Skrutskie, M. F., Cutri, R. M., Stiening, R., et al. 2006, *AJ*, 131, 1163

Slawson, R. W., Hill, R. J., & Landstreet, J. D. 1992, *ApJS*, 82, 117

Smirnov-Pinchukov, G. V., Moór, A., Semenov, D. A., et al. 2022, *MNRAS*, 510, 1148

Spitzer Science Center (SSC) & Infrared Science Archive (IRSA). 2021, *VizieR Online Data Catalog: The Spitzer (SEIP) source list (SSTSL2)* (Spitzer Science Center, 2021), *VizieR On-line Data Catalog: II/368*. Originally published in: Spitzer Science Center (SSC), IRSA (2021)

Stanford-Moore, S. A., Nielsen, E. L., De Rosa, R. J., Macintosh, B., & Czekala, I. 2020, *ApJ*, 898, 27

Stassun, K. G. & Kounkel, M. 2024, *ApJ*, 967, L36

Su, K. Y. L., Kennedy, G. M., Rieke, G. H., et al. 2023, *ApJ*, 959, 43

Su, K. Y. L., Rieke, G. H., Melis, C., et al. 2020, *ApJ*, 898, 21

Thebault, P. & Kral, Q. 2019, *A&A*, 626, A24

Tian, H.-J., El-Badry, K., Rix, H.-W., & Gould, A. 2020, *ApJS*, 246, 4

Torres, C. A. O., Quast, G. R., da Silva, L., et al. 2006, *A&A*, 460, 695

Torres, C. A. O., Quast, G. R., Melo, C. H. F., & Sterzik, M. F. 2008, *Young Nearby Loose Associations*, ed. B. Reipurth, 757

van Leeuwen, F., ed. 2007, *Astrophysics and Space Science Library*, Vol. 350, *Hipparcos, the New Reduction of the Raw Data*

Vican, L., Schneider, A., Bryden, G., et al. 2016, *ApJ*, 833, 263

Viscardi, E. M., Macías, E., Zagaria, F., et al. 2025, *A&A*, 695, A147

Visser, R., van Dishoeck, E. F., & Black, J. H. 2009, *A&A*, 503, 323

Welsh, B. Y. & Montgomery, S. 2013, *PASP*, 125, 759

Wichittanakom, C., Oudmaijer, R. D., Fairlamb, J. R., et al. 2020, *MNRAS*, 493, 234

Williams, J. P. & Andrews, S. M. 2006, *ApJ*, 653, 1480

Williams, J. P. & Cieza, L. A. 2011, *ARA&A*, 49, 67

Wilner, D. J. & Welch, W. J. 1994, *ApJ*, 427, 898

Wilson, T. L. & Rood, R. 1994, *ARA&A*, 32, 191

Wolniewicz, L. M., Berger, T. A., & Huber, D. 2021, *AJ*, 161, 231

Worthen, K., Chen, C. H., Law, D. R., et al. 2024, *ApJ*, 964, 168

Wright, E. L., Eisenhardt, P. R. M., Mainzer, A. K., et al. 2010, *AJ*, 140, 1868

Wyatt, M. C. 2008, *ARA&A*, 46, 339

Yamamura, I., Makiuti, S., Ikeda, N., et al. 2010, *VizieR Online Data Catalog*, 2298

Zechmeister, M. & Kürster, M. 2009, *A&A*, 496, 577

Zuckerman, B., Forveille, T., & Kastner, J. H. 1995, *Nature*, 373, 494

Zuckerman, B., Melis, C., Rhee, J. H., Schneider, A., & Song, I. 2012, *ApJ*, 752, 58

Zwintz, K., Reese, D. R., Neiner, C., et al. 2019, *A&A*, 627, A28

Appendix A: Properties of the selected systems

A.1. Fundamental stellar properties and photosphere models

To estimate the basic parameters of the stars, such as their effective temperature (T_{eff}) and luminosity (L_*), and to predict the photospheric contribution to the measured total flux at IR and mm wavelengths, we fitted the optical and near-IR broadband photometry available for the targets with ATLAS9 atmosphere models (Castelli & Kurucz 2004). The photometric measurements were taken from the TYCHO2 (Høg et al. 2000), Hipparcos (Perryman 1997), Gaia DR3 (Gaia Collaboration et al. 2023), APASS (Henden et al. 2016), and 2MASS (Cutri et al. 2003) surveys. Where available, these data were complemented by UBV -band photometry from Slawson et al. (1992). According to our knowledge, HD 31305 is the only star in the sample having a close companion that could contaminate its photometry (see Appendix A.2). In this case the pair of stars is not spatially resolved by Gaia either, but a high-resolution ground-based K_p -band observation suggests that the brightness difference between the two stars is only 1^m3 , which, in addition to the stars' youth, is probably due to the fact that the late-type companion hosts a protoplanetary disk (see Appendix C). Since the contamination can be significant at near-IR wavelengths, 2MASS measurements were ignored in the fitting of this target.

Synthetic photometry was derived from the model spectra for the given filter set and compared with the measured data in the fitting process. For the metallicity we adopted $[\text{Fe}/\text{H}] = 0.0 \pm 0.1$, while the estimates of the stars' interstellar reddenings ($E(B-V)$) were obtained using the Stilism 3D reddening map (Lallement et al. 2014; Capitanio et al. 2017) and utilized as an a priori information. Distances were taken from Bailer-Jones et al. (2021) adopting their geometric estimates. We used a Bayesian approach to estimate the posterior distributions of the model parameters, T_{eff} and the solid angle of the star. The derived T_{eff} and L_* parameters with their uncertainties are summarized in Table 1. The Hertzsprung–Russell diagram of the stars is shown in Figure A.1.

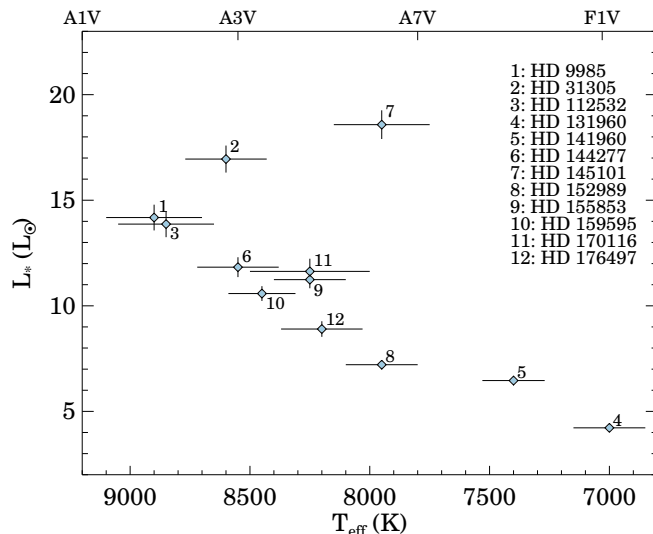


Fig. A.1: Hertzsprung–Russell diagram of our targets. The effective temperature and luminosity values are taken from Appendix A.1

A.2. Multiplicity

Using data from the Gaia DR3 catalog, we searched for stellar companions of the target stars. By applying the method proposed by Deacon & Kraus (2020) to Gaia objects in the vicinity of our targets, we identified two systems, HD 144277 and HD 152989, that have co-moving and co-distant pairs. The latter binary system was already known from the literature (Mason et al. 2001; Domanget & Nys 2002; El-Badry & Rix 2018; Tian et al. 2020). The projected separation is $12''.1$ (1739 au) for HD 144277 B (Gaia DR3 5997064901308024192) and $11''.2$ (1288 au) for HD 152989 B (Gaia DR3 6033260854136740992). By fitting the available Gaia DR3 and 2MASS broadband photometric data of the revealed companions using stellar atmosphere models, ATLAS9 for HD 152989 B and NEXTGEN (Hauschildt et al. 1999) for HD 144277 B, we obtained effective temperature estimates of 5560 ± 70 K and 3320 ± 60 K, respectively. Based on the spectral type and T_{eff} sequences for young stars derived by Pecaut & Mamajek (2013) (see their table 6), we found that these temperatures correspond to spectral types of G4 and M3.

In the Gaia DR3 catalog, the renormalized unit weight error (ruwe) parameter shows how well the single star model fits to the astrometric observations. Therefore, the high value of ruwe (> 1.2 , e.g., Belokurov et al. 2020; Bryson et al. 2020; Wolniewicz et al. 2021) can be used as a robust indicator of the unresolved binarity for Gaia sources. Taking this into account, the ruwe value of 3.06 obtained for HD 31305 strongly suggests the presence of a companion close to the star. This finding is further supported by the fact that the ipd_frac_multi_peak parameter – which shows the fraction of observing windows in which multiple peaks are detected and can thus also be used as a metric of binarity – also has a high value of 36. In good agreement with this, as reported by Cody et al. (2013), a high-resolution K_p -band image of HD 31305, obtained with the Keck/NIRC2 camera, reveals a nearby fainter star $\sim 0''.5$ away, at a position angle of $-128^{\circ}3$, which is probably a late type companion of HD 31305. In the specific band, HD 31305 is only 1.3 magnitudes brighter than its companion. The ruwe values of the other targets range between 0.8 and 1.1, and their ipd_frac_multi_peak is 0, i.e. there is no indication of close companions.

By comparing astrometric data from the Hipparcos and Gaia EDR3 catalogs, Brandt (2021) searched for signs of astrometric acceleration indicating the presence of companions. For HD 9985 and HD 170116, the two stars from our sample that are included in both catalogs, no significant acceleration was found. Consistently with this, the study of Kervella et al. (2022) – which is also based on these two catalogs – did not reveal any significant proper motion anomaly for these two stars. Thus, these data do not indicate the presence of companion stars.

A.3. Membership in young associations

We used the BANYAN Σ tool (Gagné et al. 2018), a Bayesian classifier, to assess the membership probabilities of our target stars in 27 young associations situated within 150 pc of the Sun. The input data for the calculations: stellar positions, proper motions, parallaxes and, where available, radial velocities (RVs), and the uncertainties of these parameters were taken from the Gaia DR3 catalog. For HD 9985 there is no velocity data in the Gaia catalog, but Gontcharov (2006) lists an RV of $+10.2 \pm 3.7$ km s $^{-1}$. However, since the latter measurement has a rather large uncertainty we used its heliocentric systemic ve-

Table A.1: Membership of target stars in nearby young associations.

Target name	Group	P_{memb}	Refs.	SigMA cluster
HD 31305	TAU	81.1	1,2,9,10	...
HD 112532	LCC	99.4	5	σ Cen
HD 131960	UCL	90.0	8	Libra-South
HD 141960	US	63.1	3,6,7	ρ Sco
HD 144277	UCL	99.9	3,6	η Lup
HD 145101	US	99.9	6,7	δ Sco
HD 152989	UCL	93.6	8	η Lup
HD 155853	UCL	71.5	...	Scorpio-Body
HD 176497	UCRA	100.0	3,4	CrA-North

Notes. Column 2 and 3 summarize the outcomes of BANYAN Σ , showing the most probable young association to which the star may belong (Col. 2) and the obtained membership probability (Col. 3). Column 4 lists references for previous studies dealing with the star's membership in the respective group. Using a novel clustering method (SigMA) and harnessing the unique potential of Gaia DR3, Ratzenböck et al. (2023b) proposed a new division of young stars in the Sco-Cen region. Column 5 shows the names of the subgroups to which the stars belong in this new classification. References used in this table: (1): Cody et al. (2013); (2): Gagné et al. (2018); (3): Gagné & Faherty (2018); (4): Galli et al. (2020); (5): Goldman et al. (2018); (6): Hoogerwerf (2000); (7): Luhman et al. (2018); (8): Luhman (2022); (9): Luhman (2023); (10): Mooley et al. (2013).

locity ($6.3 \pm 0.3 \text{ km s}^{-1}$) derived as the weighted center of the ^{12}CO line instead (Sect. 5.1). For two other targets, HD 31305 and HD 112532, no RV data are available, and therefore their derived membership probabilities are based only on the astrometric data. Table A.1 shows the most likely young association, and the membership probability (P_{memb}) for those 9 systems where the latter value is $> 60\%$. For these objects, previous studies have already shown that they likely belong to the indicated young stellar groups (see Table A.1).

The BANYAN Σ algorithm, following the classical approach proposed by Blaauw (1964), distinguishes three subgroups in the Scorpius-Centaurus (Sco-Cen) OB association: the Upper Scorpius (US), the Upper Centaurus Lupus (UCL) and the Lower Centaurus Crux (LCC). However, new studies, based on Gaia data, revealed a more complex morphology with more substructures in the Sco-Cen OB association (e.g. Goldman et al. 2018). Recently, by applying a new clustering algorithm, the significance mode analysis (SigMA), Ratzenböck et al. (2023b) identified 37 co-moving clusters in Sco-Cen. For the eight objects where this is relevant, the sub-clusters corresponding to this new division have also been indicated in the table. As for HD 31305, in their recent study of the Taurus star-forming region, Luhman (2023) proposed that it belongs to the L1517 subgroup.

HD 159595. For HD 159595, BANYAN Σ returned membership probabilities of 24.7% and 9.4% for the β Pic moving group (BPMG) and UCL, respectively. The $U_0, V_0, W_0 = -10.11, -15.45, -8.43$ ($\pm 0.65, \pm 0.07, \pm 0.03$) km s^{-1} galactic space velocities of the star is in excellent agreement with the average space motion of the BPMG ($\langle U \rangle, \langle V \rangle, \langle W \rangle = -10.9, -16.0, -9.10 \text{ km s}^{-1}$, Gagné et al. 2018): the relatively low membership probability is rather due to the fact that the object is located outside the space region occupied by the BPMG as defined in the BANYAN model. However, some recent results suggest that this group may

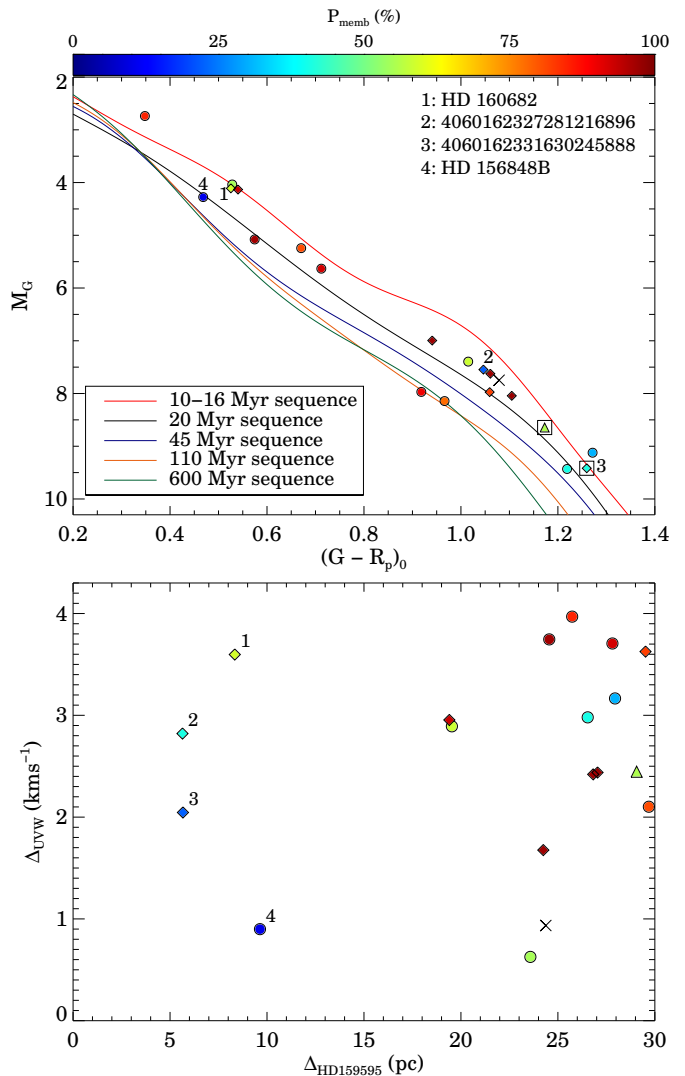


Fig. A.2: Top: ($M_G, (G - R_p)_0$) color-magnitude diagram for 21 Gaia DR3 stars located within 30 pc of HD 159595 and having similar galactic space motion (Sect. A.3). Potential members of BPMG, UCL, and US are marked by filled diamonds, circles, and triangles, respectively. The color of the symbols indicates the membership probability. A star with a group membership probability of no more than 10% in any of these clusters is marked by a cross. Stars with Gaia $\text{ruwe} > 1.2$ (possible binaries) are denoted with large squares. Empirical sequences of different ages are taken from Gagné et al. (2021). Bottom: Galactic space velocity differences (Δ_{UVW}) as a function of positional differences ($\Delta_{\text{HD}159595}$) with respect to HD 159595 for 19 stars, found to be young from the above 21.

actually be more widespread than previously thought (e.g. Hinkley et al. 2021).

Therefore, to explore this issue further, we have collected all stars located within 30 pc of HD 159595 from the Gaia DR3 catalog, that have 1) $\text{ruwe} < 1.4$, 2) $\text{parallax_over_error} > 10$, and 3) radial velocity with an uncertainty $< 5 \text{ km s}^{-1}$ and, to ensure the sufficiently good quality of the photometry, whose 4) corrected BP and RP flux excess $|C_*| < 5\sigma_{C_*}$ (see Riello et al. 2021, for the definition of C_* and σ_{C_*}). After calculating their U, V, W velocities we kept only those having velocities within 4 km s^{-1} of HD 159595 ($\Delta_{\text{UVW}} =$

$\sqrt{(U - U_0)^2 + (V - V_0)^2 + (W - W_0)^2} < 4 \text{ km s}^{-1}$). These selection criteria left us with 21 sources whose membership probabilities were also assessed using the BANYAN Σ . In Figure A.2 (top) we show the $(G - R_p)_0$ color versus absolute G magnitude diagram of the selected sources. To correct for interstellar extinction, the $E(B - V)$ reddenings of the objects were taken from *Stilism* 3D map (Lallement et al. 2014; Capitanio et al. 2017). For those stars where BANYAN Σ yielded a probability of $>10\%$ for a young association, we marked the most likely cluster and used colors to indicate the obtained probability. Empirical sequences of known coeval populations of stars that represent five different ages from Gagné et al. (2021) were also added to the plot. The figure suggests that, with two exceptions, stars with similar galactic space motion and spatial position to those of HD 159595 are young ($\lesssim 50$ Myr). In some cases, other observations confirm this result. Seven out of the nineteen stars were included in the SACY survey (Torres et al. 2006) and their outstandingly high measured lithium equivalent line widths are clear indicators of their youth. Four other objects have counterparts in the ROSAT catalog (Boller et al. 2016) and their high X-ray luminosities suggest strong coronal activity that is most likely associated with young stars. For the majority of these young stars, the most likely associated group is the BPMG (filled diamonds) or the UCL (filled circles).

Figure A.2 (bottom) displays the Δ_{UVW} velocity differences as a function of the distance from HD 159595 for the 19 young nearby co-moving stars. For most objects located more than 18 pc away, BANYAN Σ returned membership probabilities $>50\%$. The five systems assigned to the BPMG, all have $P_{\text{memb}} > 82\%$, including stars such as HD 168210 and GSC 07396-00759, which have long been identified as secure members of this group (Torres et al. 2006). Within 10 pc, in the immediate vicinity of HD 159595, there are four young stars that show similar galactic space motion. For HD 156848 B (Gaia DR3 4108078979665915648, indicated by 4 in Fig. A.2), BANYAN Σ yielded a probability of 10.4% to belong to the UCL. Apart from the fact that this indicates a rather low probability, it should be mentioned that the radial velocity of the star's companion, HD 156848 A, is quite different from that of HD 156848 B ($-4.56 \pm 0.3 \text{ km s}^{-1}$ compared to $-10.79 \pm 1.5 \text{ km s}^{-1}$) and thus for the former the Δ_{UVW} is of 5.9 km s^{-1} , which raises questions even how similar the space motion of this system to that of HD 159595. The other three stars are candidate members of the BPMG. Gaia DR3 4060162327281216896 (marked by number 2 in Fig. A.2, $P_{\text{memb,BPMG}} = 22\%$) and Gaia DR3 4060162331630245888 (number 3, $P_{\text{memb,BPMG}} = 41.1\%$) are separated in the sky by $\sim 5''$ and, based on their very similar proper motions and parallaxes, they may form a wide binary system at a distance of 5.7 pc from HD 159595. Finally, HD 160682 (number 1, $P_{\text{memb,BPMG}} = 58.8\%$) is a well-known young star with a high lithium content (Torres et al. 2006; Binks et al. 2020). The proximity of the latter two systems (three stars) to HD 159595 suggests that they belong together to the BPMG, but are further away from its main region of the group. However, it cannot be excluded that, despite their very similar galactic space motion to the BPMG, these young stars form an independent small cluster located not very far from this group.

HD 9985. According to BANYAN Σ , HD 9985 does not belong to any of the 27 young clusters considered by the classification tool. However, Oh et al. (2017) found that it has a co-moving pair, HQ Psc (TYC 1204-

171-1, Gaia DR3 288826178310839936), a late-type star. In fact, based on Gaia DR3, the two stars are 13.4 pc apart, and their galactic space motion, $U, V, W = -10.1, -5.0, -5.1 (\pm 0.2, \pm 0.2, \pm 0.2) \text{ km s}^{-1}$ for HD 9985 and $U, V, W = -11.0, -6.5, -4.3 (\pm 0.8, \pm 0.8, \pm 1.0) \text{ km s}^{-1}$ for HQ Psc, are also very similar. Binks et al. (2018) proposed that HQ Psc, together with 13 other young late-type stars, form a spatially very extended kinematic association, the 30–50 Myr old Pisces moving group. However, based on more recent and complete kinematic data, Moranta et al. (2022) found that the galactic space velocities of the proposed members are quite different, making it unlikely that this is a single coeval group. Alternatively, they suggest that HQ Psc may form a smaller group with three other previously proposed members of the putative Pisces MG, but the fact that HQ Psc is 65 pc away from even the nearest of these stars (and 123 pc from the furthest one) makes this suggestion questionable as well, yet. So, although their similar motions and spatial positions suggest that HD 9985 and HQ Psc belong to the same moving group further investigation is needed to see if there are other members in their vicinity.

HD 170116. Due to its greater distance, the HD 170116 is well outside the region considered by the BANYAN Σ model, so it is not surprising that the tool found no relationship between the listed young groups and the star. Other literature data do not suggest any group membership either. Using the same criteria as in the case of HD 159595, our search for co-moving stars in the 30 pc neighborhood of the target resulted in 9 objects. Of these, only one, Gaia DR3 4270531719524839936, is likely a young star (< 100 Myr), based on its position on the color-magnitude diagram ($(G - R_p)_0$ vs. M_G , CMD) and its strong X-ray emission ($\log L_X/L_{\text{bol}} = -3.1 \pm 0.2$). This star has a UVW velocity of $-7.7, -22.5, -6.9 (\pm 2.2, \pm 1.2, \pm 0.2) \text{ km s}^{-1}$, which is almost identical with that of HD 170116 ($U, V, W = -7.4, -22.2, -6.7 (\pm 1.2, \pm 0.7, \pm 0.1) \text{ km s}^{-1}$).

A.4. Stellar ages and masses

With the exception of HD 145101, stars that found to be members of young associations (Table 1) were assumed to have the same age as that of the group. The ages for the US, UCL, and LCC subgroups of the Sco-Cen association, 10 ± 3 , 15 ± 3 , and 16 ± 2 Myr, are taken from Gagné et al. (2018). For the L1517 subgroup of the Taurus, that includes HD 31305, Luhman (2023) obtained an age estimate of $2.5^{+3.8}_{-1.5}$ Myr. To estimate the masses of these stars, their effective temperatures and luminosities obtained in Appendix A.1 were compared to the theoretical predictions of the MESA Isochrones and Stellar Tracks (Choi et al. 2016; Dotter 2016). In the isochrone fitting, we followed the method proposed by Pascucci et al. (2016), by assuming a metallicity of $[\text{Fe}/\text{H}] = 0.0 \pm 0.1$ and taking into account the derived ages as an a priori information. Note that even if the new, finer SigMa-based subdivision of the Sco-Cen and the new subcluster ages (Ratzenböck et al. 2023a) are used instead of the classical ones, no significant difference in the mass estimates is obtained, since the alternative age estimates are in good agreement with the used ones within the uncertainties. Based on its position on the HRD (Fig. A.1), HD 145101 clearly appears to be a pre-main sequence star which is likely younger than the average of the US population, which group is found to exhibit quite wide age range between 3 and 19 Myr by Ratzenböck et al. (2023a). For this target, therefore we only assumed a priori that it is younger than

20 Myr (as a member of the US group), and its final age estimate, $6.7^{+1.0}_{-0.7}$ Myr, was derived from the isochrone fitting.

If HD 159595 belongs to the BPMG, then we can use the age of the group as a priori data in the isochrone fitting. Using the average of the age estimates from the literature, Gratton et al. (2024) derived an age of 21 ± 4 Myr for this group. However, it is possible that HD 159595, together with three other nearby stars (two of which, Gaia DR3 4060162327281216896 and Gaia DR3 4060162331630245888, constitute a wide binary), may form a small cluster separate from the BPMG (Appendix A.3). Taking into account the available age indicators, however, it can be concluded that this small group may not only have UVW velocity but also an age quite similar to that of the BPMG. On the CMD shown in Figure A.2 (top), HD 160682, Gaia DR3 4060162327281216896, and Gaia DR3 4060162331630245888, are all located between the 10–16 and 20 Myr empirical sequences, although the latter star has a ruwe of 1.21, raising the possibility that it is not a single system. Comparing the lithium equivalent width measured in the SACY survey (Torres et al. 2006) for HD 160682 ($EW_{Li} = 260$ mÅ, $(B - V)_0 = 0.070$) with the sequence of Li equivalent widths of BPMG stars (Stanford-Moore et al. 2020, figure 5) we find a good match. Using the *eagles* tool (Jeffries et al. 2023) to estimate the stellar age from the lithium observation we obtained an upper limit of 50 Myr. Overall, this small group is also of similar age, or at most a few million years younger than the BPMG, so for the final age estimate of HD 159595 we adopted the age of the BPMG by assigning a somewhat higher value to the lower age uncertainty (21^{+4}_{-5} Myr). We used this age as an a priori information in the mass estimate of the star.

In age diagnostic of HD 9985, we assumed that the star is co-moving and coeval with HQ Per. For the latter star, using the available broadband photometric data (from Gaia DR3, TYCHO, APASS and 2MASS surveys) and the method described in Sect. A.1 we obtained T_{eff} of 5940 ± 100 K and L_* of $1.27 \pm 0.06 L_{\odot}$. The posterior age probability distributions were then determined for both stars via isochrone fitting. Using the measured lithium equivalent width of HQ Psc (144 ± 21 mÅ, Binks et al. 2015) and the derived T_{eff} , we also obtained an age posterior probability distribution based on this indicator by applying the *eagles* package again. Finally, the fast rotation ($P_{\text{rot}} = 1.87$ d, Binks et al. 2015) and the strong X-ray emission ($\log L_X/L_{\text{bol}} = -3.84$, Binks et al. 2015) of this late-type star indicate an age of < 100 Myr. By combining all these age posterior distributions and determining the median and the 68% confidence interval of the final distribution, we obtained an age estimate of 44^{+31}_{-16} Myr for HD 9985 (and for HQ Psc).

HD 170116 also has a potential young late-type co-moving pair, the Gaia DR3 4270531719524839936. If we assume that the similarity in their kinematics is due to the fact that they were born in the same star formation region at roughly the same time, then their age analysis is worth combining. Based on optical and near-IR photometric data we derived T_{eff} of 4980 ± 90 K and L_* of $0.44 \pm 0.04 L_{\odot}$ for the late-type star. Its high X-ray luminosity (Sect. A.3) implies strong magnetic activity and fast spinning. To further study this, we downloaded its ASAS-SN g-band light curve using the *SkyPatrol* tool⁸. By applying the Generalized Lomb-Scargle algorithm (GLS; Zechmeister & Kürster 2009) to the data we found that the star exhibits significant periodic variability with a period of ~ 2.4 d, likely due to rotational variations from surface spots. This rapid rotation and the strong X-ray emission both indicate that Gaia DR3 4270531719524839936 is

Table A.2: Basic disk properties.

Target name	T_{dust} (K)	β	$L_{\text{disk}}/L_{\text{bol}}$
HD 9985	80 ± 6	0.41 ± 0.15	$1.3e-03$
HD 112532	139 ± 12	0.65	$7.3e-04$
HD 131960	182 ± 16	0.65	$1.3e-03$
HD 141960	119 ± 8	0.65	$2.3e-03$
HD 144277	151 ± 18	0.65	$5.9e-04$
HD 145101	163 ± 15	0.65	$6.1e-04$
HD 152989	96 ± 4	0.85 ± 0.09	$7.6e-03$
HD 155853	159 ± 11	0.65	$1.7e-03$
HD 159595	90 ± 4	0.65	$2.1e-03$
HD 170116	74 ± 3	0.40 ± 0.11	$1.4e-03$
HD 176497	141 ± 9	0.60 ± 0.16	$1.7e-03$

younger than 100 Myr (Bouma et al. 2023; Stassun & Kounkel 2024). By performing isochrone fitting for both stars – assuming that neither has a close companion (in line with their Gaia ruwe of < 1.2) – and combining the results, also taking into account the upper age limit derived above, we obtain an age estimate of 31^{+9}_{-7} Myr. We note that this result is mostly based on the isochrone fitting of Gaia DR3 4270531719524839936.

A.5. Fundamental disk properties

Figure A.3 shows the spectral energy distribution from $1 \mu\text{m}$ to 2 mm for all our targets except HD 31305. The plotted IR photometry are taken from the 2MASS (Skrutskie et al. 2006), AllWISE (Cutri & et al. 2014), AKARI IRC and FIS (Ishihara et al. 2010; Yamamura et al. 2010), and *IRAS* FSC (Moshir et al. 1990) all-sky survey catalogs. In addition, three of our targets were serendipitously observed as part of larger surveys performed by the *Spitzer* and/or the *Herschel* space telescopes, allowing us to complement their SEDs by *Spitzer* IRAC and MIPS photometry (Fazio et al. 2004; Rieke et al. 2004) from the *Spitzer* Enhanced Imaging Products (SEIP; *Spitzer* Science Center (SSC) & Infrared Science Archive (IRSA) 2021, DOI: 10.26131/IRSA3) and *Herschel* PACS data (Poglitsch et al. 2010) from the *Herschel*/PACS Point Source catalogs (Marton et al. 2017). To correct for potential overestimation of the true flux in the saturated WISE W2-band photometry at $4.6 \mu\text{m}$, we used the method proposed by Cotten & Song (2016, equation 5). The final photometric uncertainties were derived as quadratic sums of the measurement errors listed in the catalogs and the corresponding absolute calibrational uncertainties (Ishihara et al. 2010; Yamamura et al. 2010; Balog et al. 2014, The AllWISE Data Release⁹, IRAC Instrument Handbook¹⁰, MIPS Instrument Handbook¹¹). The ALMA photometric data points obtained in our project at 1.33 mm (Table 1) are also added to the plots.

To estimate the basic disk properties, the characteristic dust temperature (T_{dust}) and the fractional luminosity ($L_{\text{disk}}/L_{\text{bol}}$), the excess SEDs – derived by subtracting the photospheric models (Sect. A.1) from the measured flux densities – are fitted by a single temperature modified blackbody (MBB) model whose emissivity is 1 at wavelengths shorter than λ_0 and varies as $(\lambda/\lambda_0)^{-\beta}$ beyond that. The rationale for using this type of model

⁹ <https://wise2.ipac.caltech.edu/docs/release/allwise/>

¹⁰ <https://irsa.ipac.caltech.edu/data/SPITZER/docs/irac/iracinstrumenthandbook/>

¹¹ <https://irsa.ipac.caltech.edu/data/SPITZER/docs/mips/mipsinstrumenthandbook/>

⁸ <https://asas-sn.osu.edu>

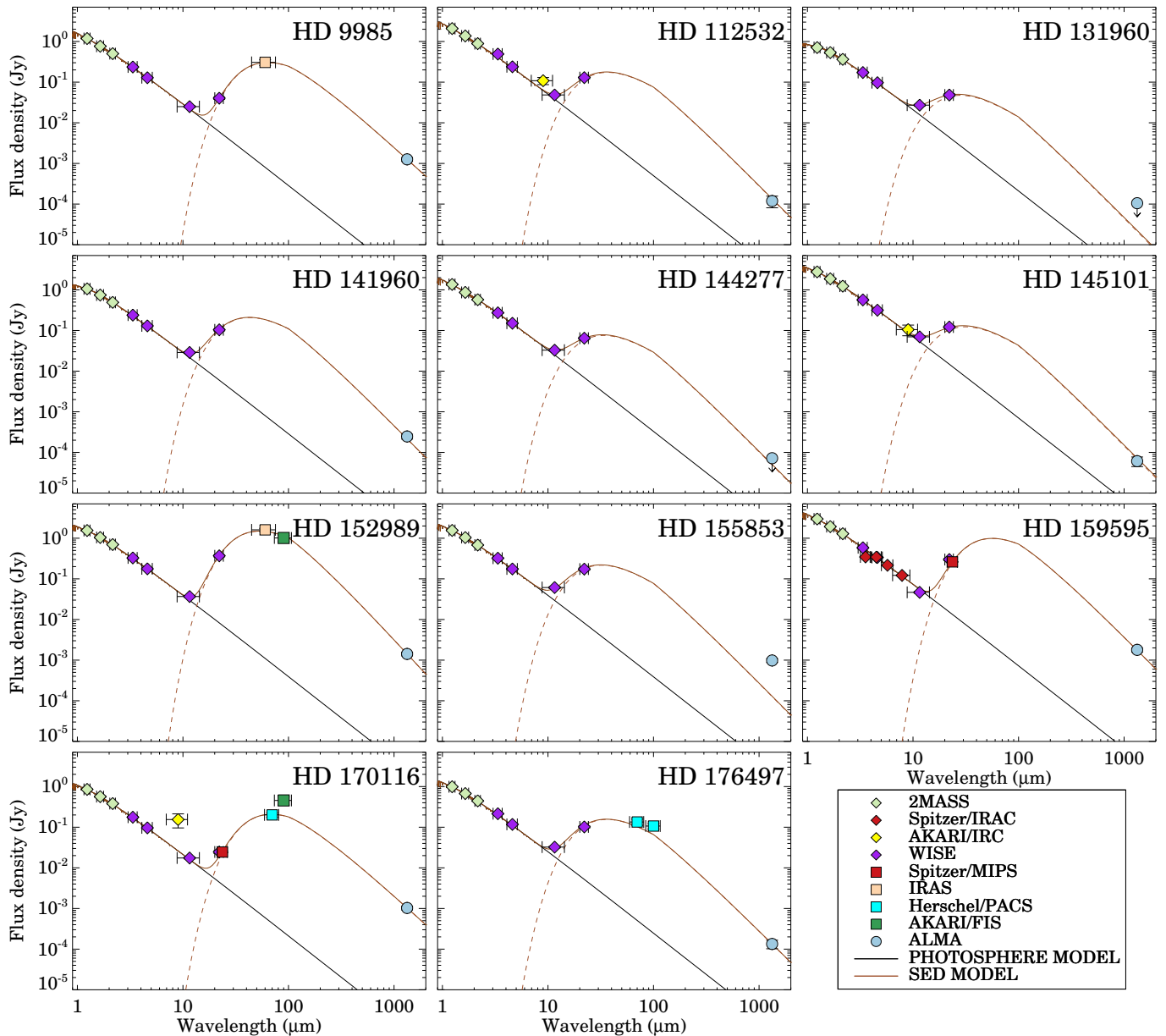


Fig. A.3: Spectral energy distributions of the studied systems. The stellar photosphere and the best-fitting SED models (Sect. A.5) are also displayed. The horizontal bars show the width of the filters used to obtain the photometric data.

is that observations show that at wavelengths well above the typical grain size, the spectrum of debris disks falls off significantly steeper than that of a blackbody. To find the best-fitting model, we used the MPFIT IDL routine (Markwardt 2009). For HD 9985, HD 152989, HD 170116, and HD 176497, where far-IR data points in the wavelength range between 25 and 200 μm are available, we fixed the λ_0 break wavelength to 100 μm (Williams & Andrews 2006), while the dust temperature, the solid angle of the emitting region and the β were free parameters. For the other objects, where the measurements, except for the ALMA observation, are limited to wavelengths shorter than 25 μm , the β parameter was also fixed at 0.65. The obtained disk parameters are summarized in Table A.2.

The lack of far-infrared data points and, in more general, the sparse sampling of the SEDs, makes it difficult to assess for some

of the sources how correct the adopted single temperature component model is, and whether a colder dust component is not actually present, as observed in many debris disks (Kennedy et al. 2014; Chen et al. 2014). The fact that, with the fixed disk parameters, most of these SED models agree reasonably well with the measured ALMA flux density at 1.33 mm suggests that, if there is a colder dust component at all, its contribution is not particularly pronounced. HD 155853, however, is an exception: its MBB model significantly underestimates the millimeter brightness of the disk and even if a pure blackbody model were used, the measured flux density would not match. We also know from the ALMA observations (Sect. 4) that the star is surrounded by a spatially extended, presumably cold, outer disk. So for this object, with a proper sampling, we would probably see an excess SED that is better modeled by two dust components with differ-

ent temperatures. Assuming that this cold component can also be described by a modified blackbody model with the same fixed λ_0 and β parameters as we used above, the fractional luminosity can be estimated from the ALMA measurement. The temperature of the cold dust is not known, but it is reasonable to assume that it should be higher than 47 K, which is the blackbody temperature corresponding to the measured radius of the disk (Table 1). Taking these into account, we obtain a lower limit of 3.3×10^{-4} for f_d of the cold component.

Appendix B: Overview of the imaging parameters

Table B.1 present the relevant imaging parameters for our continuum and line observations.

Table B.1: Overview of the imaging parameters for continuum and CO line observations.

	Continuum	^{12}CO	^{13}CO	C^{18}O
HD 9985				
Beam size (arcsec \times arcsec)	0.58 \times 0.45	0.58 \times 0.46	0.61 \times 0.47	0.61 \times 0.47
Beam PA (°)	36.6	38.1	38.1	38.4
rms noise ($\mu\text{Jy beam}^{-1} / \text{mJy beam}^{-1} \text{ch}^{-1}$)	15.9	1.6	0.8	0.6
HD 31305				
Beam size (arcsec \times arcsec)	0.42 \times 0.25	0.42 \times 0.25	0.45 \times 0.27	0.47 \times 0.27
Beam PA (°)	-0.5	0.1	5.6	4.9
rms noise ($\mu\text{Jy beam}^{-1} / \text{mJy beam}^{-1} \text{ch}^{-1}$)	21.3	2.7	1.4	1.2
HD 112532				
Beam size (arcsec \times arcsec)	0.57 \times 0.41	0.58 \times 0.42
Beam PA (°)	-66.4	-66.7
rms noise ($\mu\text{Jy beam}^{-1} / \text{mJy beam}^{-1} \text{ch}^{-1}$)	19.0	2.3
HD 131960				
Beam size (arcsec \times arcsec)	1.16 \times 1.05	1.25 \times 1.15
Beam PA (°)	81.8	76.8
rms noise ($\mu\text{Jy beam}^{-1} / \text{mJy beam}^{-1} \text{ch}^{-1}$)	27.3	4.1
HD 141960				
Beam size (arcsec \times arcsec)	0.51 \times 0.40	0.53 \times 0.40
Beam PA (°)	-77.6	-76.4
rms noise ($\mu\text{Jy beam}^{-1} / \text{mJy beam}^{-1} \text{ch}^{-1}$)	14.9	1.8
HD 144277				
Beam size (arcsec \times arcsec)	0.63 \times 0.54	0.65 \times 0.54
Beam PA (°)	-81.6	-82.4
rms noise ($\mu\text{Jy beam}^{-1} / \text{mJy beam}^{-1} \text{ch}^{-1}$)	18.0	2.2
HD 145101				
Beam size (arcsec \times arcsec)	0.51 \times 0.37	0.52 \times 0.37	0.54 \times 0.42	0.54 \times 0.42
Beam PA (°)	-74.2	-77.9	-71.2	-71.0
rms noise ($\mu\text{Jy beam}^{-1} / \text{mJy beam}^{-1} \text{ch}^{-1}$)	15.1	1.9	1.0	0.8
HD 152989				
Beam size (arcsec \times arcsec)	0.37 \times 0.28	0.38 \times 0.29	0.39 \times 0.32	0.40 \times 0.32
Beam PA (°)	88.5	84.6	83.0	84.9
rms noise ($\mu\text{Jy beam}^{-1} / \text{mJy beam}^{-1} \text{ch}^{-1}$)	16.1	2.1	1.2	0.9
HD 155853				
Beam size (arcsec \times arcsec)	0.57 \times 0.40	0.51 \times 0.38	0.57 \times 0.41	0.58 \times 0.41
Beam PA (°)	-71.7	-72.6	-73.7	-74.5
rms noise ($\mu\text{Jy beam}^{-1} / \text{mJy beam}^{-1} \text{ch}^{-1}$)	15.3	2.4	1.0	0.9
HD 159595				
Beam size (arcsec \times arcsec)	0.45 \times 0.39	0.42 \times 0.37
Beam PA (°)	-69.7	-73.9
rms noise ($\mu\text{Jy beam}^{-1} / \text{mJy beam}^{-1} \text{ch}^{-1}$)	19.5	5.0
HD 170116				
Beam size (arcsec \times arcsec)	0.49 \times 0.41	0.50 \times 0.41	0.52 \times 0.42	0.52 \times 0.42
Beam PA (°)	-70.3	-74.4	-74.0	-74.2
rms noise ($\mu\text{Jy beam}^{-1} / \text{mJy beam}^{-1} \text{ch}^{-1}$)	13.0	1.7	0.9	0.7
HD 176497				
Beam size (arcsec \times arcsec)	0.51 \times 0.32	0.49 \times 0.31
Beam PA (°)	81.7	82.5
rms noise ($\mu\text{Jy beam}^{-1} / \text{mJy beam}^{-1} \text{ch}^{-1}$)	13.0	1.7

Notes. For systems where we detected circumstellar CO gas (even around the companion star, as in the case of HD 31305), the imaging parameters (size and position angle of the synthesised beam, as well as 1 σ rms noise levels) are provided for all three CO isotopologs in addition to the continuum, while for the other objects the parameters are listed only for the continuum and ^{12}CO measurements. The quoted parameters refer to the naturally weighted data sets for HD 144277 and HD 176497, the tapered data for HD 131960 (Gaussian taper with a size of 1''), and Briggs weighted data (robust=0.5) for the rest of the sample. For the ^{12}CO measurements of HD 155853 and HD 159595, we consider the data cubes produced by neglecting the shortest baseline visibilities (see Sect. 5).

Appendix C: The circumstellar disk of HD 31305 B

The ALMA continuum observation of HD 31305 revealed a bright compact source (Fig. 1). To estimate its basic parameters we used `uvmultifit` as in Sect. 4.2, adopting both a point source and an elliptical Gaussian model for the surface brightness distribution, the latter being proven more suitable based on the BIC test. The derived position differs by ~ 580 mas from that of the primary A-type component of this binary system (the intended target of the measurement). Based on the S/N and the beam size, the nominal expected absolute astrometric accuracy of the measurement is ~ 25 mas, i.e., even if the actual absolute positional accuracy may be twice this value or even worse¹², this positional difference is well determined. However, the detected source coincides well with the position of HD 31305 B. For the latter star, the separation of the millimeter source is 70 mas or 40 mas depending on whether the system's proper motion is taken from the Gaia DR3 or UCAC4 catalog in the calculations. Figure 1 and C.1 display the UCAC-based position of the companion. The observed continuum emission thus probably comes from a disk around the companion. We obtained a flux density of 2.37 ± 0.24 mJy for the source, where the uncertainty is the quadratic sum of the measurement error (0.03 mJy) and the calibration error (assumed to be 10%). Assuming optically thin emission and that the temperature of the emitting grains is 20 K, then Eq. 1 yields a dust mass estimate of 1.42 ± 0.15 M_{\oplus} . Based on the FWHM of the major axis of the fitted Gaussian, we derived a characteristic disk size of 60 ± 15 mas, which corresponds to 8.6 ± 2.2 au at the distance of the system.

By examining the measured CO line data cubes, we found significant emission in the v_{LSR} interval from -10.4 to $+10.0$ km s $^{-1}$ for all three isotopologs. We used this velocity range to construct moment 0 maps for all three lines. As demonstrated by the ^{12}CO and ^{13}CO moment 0 maps shown in Fig. C.1 (left and middle panels), the line emission originate from a compact source, which coincides with the position of the continuum source. To estimate the integrated line fluxes we used the same method as for HD 145101 (Sect. 5.1). By using elliptical apertures of different sizes, whose shape is identical to the actual beam, we determined the minimum aperture size that includes all the CO emission associated with the source and measured the line flux. The uncertainty of the derived flux was estimated by placing this aperture at random positions outside the source and calculating the standard deviation of the flux values measured in them. This method yielded line fluxes of $F_{^{12}\text{CO}} = (30.6 \pm 3.3) \times 10^{-22}$ W m $^{-2}$, $F_{^{13}\text{CO}} = (7.6 \pm 1.3) \times 10^{-22}$ W m $^{-2}$, and $F_{\text{C}^{18}\text{O}} = (4.8 \pm 0.9) \times 10^{-22}$ W m $^{-2}$, where the quoted uncertainties are the quadratic sum of the measurement error and the calibration error. The spectra obtained using the given apertures for the three lines are shown in Fig. C.1 (right panel). Adopting abundance ratios typical of the local interstellar medium ($^{12}\text{C}/^{13}\text{C} = 77$ and $^{16}\text{O}/^{18}\text{O} = 560$, Wilson & Rood 1994), the measured fluxes indicate that both the ^{12}CO and the ^{13}CO lines are optically thick. Based on the C^{18}O measurement, assuming that the line is optically thin and taking into account the above abundance ratio, we obtained a CO disk mass of $2.05 \pm 0.42 \times 10^{-2} M_{\oplus}$.

Although we know of some debris disks with millimeter-sized dust content only slightly lower than that of HD 31305 B, in those systems the dust is located at > 50 au from the star (e.g. Matrà et al. 2025). Similar can be said for the gas component, as discussed in Sect. 6, in young debris disks with CO content similar to or even higher than that measured for HD 31305 B, the gas

is located at radial distances of several tens of au. Furthermore, all CO-rich debris disks have been found around A-type stars.

To further explore the nature of HD 31305 B, we examined the slope of its SED between 2 and 24 μm . As a first step, we color corrected the photometric data gathered from the 2MASS, AllWISE, IRC, and SEIP catalogs. Since HD 31305 A contributes to the measured emission in all photometric bands, we subtracted its stellar photosphere model from the measured flux densities. By fitting a line to the data points obtained this way, we then derived a mid-IR slope of $\alpha_{\text{IR}} = -0.94 \pm 0.03$. This slope value, between -1.6 and -0.3 , implies that HD 31305 B is probably a class II source (Lada 1987; Williams & Cieza 2011), i.e. its disk is protoplanetary in nature. This classification is further supported by the fact that the system belongs to the 2.5 Myr old L1517 subgroup of the Taurus star forming region, and that no such compact debris disk with such a high dust and gas content is known.

¹² <https://help.alma-science.org/kb/articles/what-is-the-absolute-astrometric-accuracy-of-alma>

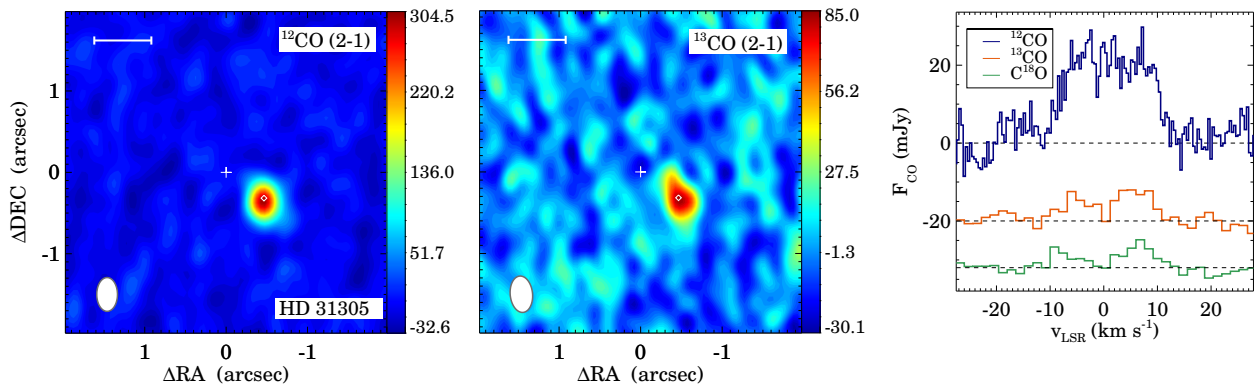


Fig. C.1: Left and middle panels: ^{12}CO and ^{13}CO $J=2-1$ moment 0 maps for HD 31305 B, respectively. At the bottom left of each panel a filled white ellipse shows the beam size. The length of the horizontal white bars correspond to 100 au. The white plus sign shows the position of HD 31305 A while the white diamond displays the position of HD 31305 B. The color bar units are $\text{mJy beam}^{-1} \text{ km s}^{-1}$. The right panel displays the obtained CO spectra in all three isotopologs. For clarity, the ^{13}CO and C^{18}O spectra have been shifted downward. The horizontal dashed lines show the zero flux levels of the spectra.

Appendix D: Comparison sample

Table D.1 presents the main properties of those young (<50 Myr) systems with dust-rich ($f_d > 5 \times 10^{-4}$) debris disks for which CO line observations are available in the literature.

Table D.1: Comparison sample.

Identifier	D (pc)	Group	Age (Myr)	SpT	L_* (L_\odot)	M_* (M_\odot)	T_d (K)	L_{disk} / L_*	R_{disk} (au)	W_{disk} (au)	$L_{12\text{CO}}$ (W m $^{-2}$)	M_{CO} (M_\oplus)	Refs.	Label
RZ Psc	184.7	...	30±10	G8V	0.80	1.10	500	7.0e-02	6.0	...	<3.23×10 ¹⁶	<1.0×10 ⁻⁵	43	...
49 Cet	57.1	ARG	48±10	A2V	15.61	1.95	155/56	2.0e-04/7.0e-04	136.0	147.0	1.16±0.12×10 ¹⁸	7.1 $^{+1.2}_{-1.1}$ ×10 ⁻³	2,22,26,30,48	a
HD 15115	48.7	THA	37±11	F4V	3.60	1.40	62	5.1e-04	93.0	21.0	<4.80×10 ¹⁵	<1.2×10 ⁻⁶	17,22,35,36,48	...
HD 15745	71.5	BPMG	21±4	F0V	4.20	1.40	147/81	3.5e-04/1.9e-03	65.0	<50.0	<4.71×10 ¹⁶	<1.2×10 ⁻⁵	10,22,24	...
HD 21997	69.6	COL	36±8	A4V	10.49	1.76	61	5.7e-04	94.0	52.0	9.15±0.93×10 ¹⁷	4.8 $^{+0.8}_{-0.9}$ ×10 ⁻²	2,22,26,48	b
HD 32297	129.3	...	<30	A7V	7.98	1.65	234/82	8.7e-04/6.2e-03	122.3	62.0	1.58±0.15×10 ¹⁸	5.0 $^{+1.6}_{-1.5}$ ×10 ⁻²	1,2,16,22,30,48	c
HD 36546	99.9	118TAU	10±3	A2V	13.86	1.86	570/135	.../4.0e-03	70.0	150.0	2.45±0.25×10 ¹⁸	3.2 $^{+1.2}_{-1.2}$ ×10 ⁻³	13,22,37,48	d
β Pic	19.4	BPMG	21±4	A6V	8.65	1.75	85	2.6e-03	105.0	92.0	1.58±0.18×10 ¹⁷	4.8 $^{+1.2}_{-1.4}$ ×10 ⁻⁵	2,4,11,21,22,38,47	e
HD 48370	35.9	COL	36±8	K0V	0.77	0.96	41	5.6e-04	88.3	37.1	<4.01×10 ¹⁶	<1.2×10 ⁻⁵	2,20,28,36	...
HD 61005	36.4	ARG	48±10	G8V _k	0.64	0.92	109/52	2.9e-04/3.0e-03	72.6	38.0	<1.05×10 ¹⁶	<4.0×10 ⁻⁶	1,2,22,36	...
HD 95086	86.4	CAR	28±11	A8V	6.55	1.58	184/54	1.5e-04/1.3e-03	206.0	180.0	<1.43×10 ¹⁶	<4.0×10 ⁻⁶	2,19,22,26,48	f
HD 98363	137.0	LCC	15±3	A4V	12.02	1.83	295/112	2.8e-04/6.4e-04	<6.22×10 ¹⁶	<9.5×10 ⁻⁶	3,29,48	...
HD 106906	102.2	LCC	15±3	F5V	7.02	2.71	108/53	1.5e-03/3.5e-04	100.0	80.0	<3.84×10 ¹⁶	<8.3×10 ⁻⁶	1,10,22,34,40,48	...
HR 4796	70.7	TWA	10±3	A0V	21.42	2.10	108	4.6e-03	77.8	14.8	<4.60×10 ¹⁶	<3.5×10 ⁻⁶	9,10,22,39,48	g _b
HD 109832	107.1	LCC	15±3	F1V	5.37	1.46	186/92	2.5e-04/5.1e-04	<3.49×10 ¹⁶	<6.4×10 ⁻⁶	1,19,29,48	...
HD 110058	129.7	LCC	15±3	A5V	8.71	1.67	499/112	2.4e-05/1.4e-03	30.9	48.9	1.41±0.18×10 ¹⁷	9.3 $^{+3.5}_{-2.2}$ ×10 ⁻³	2,3,6,48	h
HD 111161	109.2	LCC	15±3	A5V	9.05	1.68	142	7.2e-04	71.3	...	<4.61×10 ¹⁶	<1.2×10 ⁻⁵	8,12,48	i
HD 111520	107.8	LCC	15±3	F5/6V	2.66	1.32	107/45	1.4e-03/1.5e-03	76.0	50.0	<5.13×10 ¹⁶	<1.3×10 ⁻⁵	1,12,22,36,48	...
HD 112810	133.2	LCC	15±3	F3/5V	3.54	1.36	227/58	1.9e-04/1.1e-03	90.0	<200.0	<6.86×10 ¹⁶	<1.8×10 ⁻⁵	1,12,22,34,48	...
HD 113556	100.3	LCC	15±3	F2V	4.42	1.41	268/60	8.9e-05/4.4e-04	110.0	<400.0	<3.33×10 ¹⁶	<8.5×10 ⁻⁶	3,12,22,36,48	...
HD 113766	108.6	LCC	15±3	F3/5V	4.00	1.50	490/15	3.3e-02/7.0e-04	30.0	<60.0	<4.88×10 ¹⁶	<1.3×10 ⁻⁵	12,22,33,34,42,48	...
HD 114082	94.9	LCC	15±3	F3V	3.75	1.47	110	4.3e-03	38.0	<40.0	<1.66×10 ¹⁶	<4.9×10 ⁻⁶	1,10,22,36	...
HD 115600	108.9	LCC	15±3	F2V	4.75	1.48	109	2.5e-03	90.0	<200.0	<4.58×10 ¹⁶	<1.2×10 ⁻⁵	1,12,22,48	...
HD 117214	107.1	LCC	15±3	F6V	5.35	1.50	111	3.1e-03	42.0	<50.0	<2.11×10 ¹⁶	<5.2×10 ⁻⁶	1,10,22,48	...
HD 121191	131.9	LCC	15±3	A7V	7.58	1.62	555/118	2.1e-03/2.6e-03	55.0	54.0	3.43±0.34×10 ¹⁷	5.6 $^{+3.3}_{-2.8}$ ×10 ⁻³	2,10,22,29,44,48	j
HD 121617	117.5	UCL	16±2	A2V	14.51	1.90	105	4.8e-03	78.0	60.0	1.61±0.17×10 ¹⁸	2.6 $^{+0.5}_{-0.4}$ ×10 ⁻²	2,22,25,29,48	k
HD 129590	135.9	UCL	16±2	G3V	3.00	1.30	89	7.7e-03	79.0	70.0	9.51±2.38×10 ¹⁶	9.5 $^{+6.5}_{-6.5}$ ×10 ⁻⁵	1,10,22	x
HD 131488	151.4	UCL	16±2	A2V	13.64	1.87	570/94	2.8e-03/2.7e-03	92.0	46.0	1.64±0.17×10 ¹⁸	9.3 $^{+1.2}_{-1.2}$ ×10 ⁻²	22,29,44,48	l
HD 131835	129.1	UCL	16±2	A4V	9.81	1.72	176/71	8.2e-04/2.2e-03	83.7	87.0	1.22±0.13×10 ¹⁸	1.6 $^{+0.2}_{-0.3}$ ×10 ⁻²	2,12,22,27,48	m
HD 134888	111.8	UCL	16±2	F3/5V	3.27	1.36	166/67	3.0e-04/1.0e-03	<6.90×10 ¹⁶	<1.8×10 ⁻⁵	1,12,48	...
HD 135953	127.3	UCL	16±2	F5V	2.42	1.22	61	9.0e-04	<8.05×10 ¹⁶	<2.1×10 ⁻⁵	1,12,48	...
HD 138813	135.9	US	10±3	A1V	21.74	2.11	153/75	7.4e-04/7.4e-04	120.0	130.0	2.39±0.27×10 ¹⁸	2.0 $^{+0.4}_{-0.4}$ ×10 ⁻²	12,22,46,48	n
HD 141569	111.3	...	5.9 $^{+1.9}_{-0.6}$	A0Ve	21.88	2.06	...	9.0e-03	130.0	240.0	1.14±0.11×10 ¹⁹	1.0 $^{+0.5}_{-0.2}$ ×10 ⁻¹	5,23,45	o
HD 142446	135.0	UCL	16±2	F3V	3.73	1.39	239/65	1.8e-04/7.7e-04	110.0	80.0	<9.05×10 ¹⁶	<2.3×10 ⁻⁵	1,12,22,48	...
NO Lup	132.8	Lupus	1–3	K7	0.29	0.70	117 $^{+25}_{-120}$	3.4e-03/2.0e-07 $^{+2.0e-07}_{-4.0e-03}$	<56.0	...	7.06±1.70×10 ¹⁷	4.9 $^{+1.1}_{-1.1}$ ×10 ⁻⁵	7,14,15	...
HD 143675	135.0	UCL	16±2	A7V	8.40	1.67	374/127	1.8e-04/4.1e-04	52.4	...	<1.68×10 ¹⁶	<5.0×10 ⁻⁶	3,8,10,29,48	p
HD 145263	141.2	US	10±3	F2V	4.98	1.50	265	1.5e-02	<1.05×10 ¹⁷	<2.7×10 ⁻⁵	12,32,34,48	...
HD 145560	120.8	UCL	16±2	F5V	3.27	1.35	103/53	1.8e-03/2.1e-03	76.0	50.0	<4.43×10 ¹⁶	<1.1×10 ⁻⁵	1,12,22,48	...
HD 145880	123.0	UCL	16±2	A0V	19.74	2.06	196/70	2.9e-04/8.3e-04	<9.88×10 ¹⁶	<2.0×10 ⁻⁵	1,19,29,48	...
HD 146181	127.0	UCL	16±2	F6V	2.81	1.28	124/71	9.6e-04/2.0e-03	74.0	<90.0	<5.34×10 ¹⁶	<1.4×10 ⁻⁵	1,12,22,36,48	...

Table D.1: continued

Identifier	D (pc)	Group	Age (Myr)	SpT	L_* (L_\odot)	M_* (M_\odot)	T_d (K)	L_{disk} / L_*	R_{disk} (au)	W_{disk} (au)	$L_{^{12}\text{CO}}$ (W m $^{-2}$)	M_{CO} (M_\oplus)	Refs.	Label
HD 146897	131.6	US	10 ± 3	F2/3V	4.78	1.42	304/94	3.0e-04/5.3e-03	82.0	<90.0	$9.57 \pm 2.39 \times 10^{16}$	$4.0_{-1.5}^{+59.1} \times 10^{-5}$	2,3,12,22,48	y
HD 156623	108.0	UCL	16 ± 2	A2V	13.28	1.86	605/123	1.6e-03/3.4e-03	77.8	119.0	$1.27 \pm 0.13 \times 10^{18}$	$2.1_{-0.4}^{+0.4} \times 10^{-3}$	12,19,29,48	q
HD 172555	28.8	BPMG	21 ± 4	A7V	7.84	1.66	250	7.5e-04	7.5	...	$1.30 \pm 0.23 \times 10^{16}$	$8.3_{-3.8}^{+3.8} \times 10^{-6}$	41,42,48	r
HD 181327	47.7	BPMG	21 ± 4	F6V	2.83	1.41	78	2.6e-03	81.3	16.0	$6.49 \pm 1.13 \times 10^{15}$	$1.9_{-0.6}^{+1.9} \times 10^{-6}$	2,18,22,35,36	z
HD 191089	50.0	BPMG	21 ± 4	F5V	2.73	1.20	92	1.5e-03	44.8	16.0	$<1.15 \times 10^{16}$	$<2.9 \times 10^{-6}$	10,22,35,36	...
CP-72 2713	36.7	BPMG	21 ± 4	K7Ve	0.19	0.80	43	1.1e-03	130.0	100.0	$<2.68 \times 10^{16}$	$<6.9 \times 10^{-6}$	22,31,36,48	...

Notes. With the exception of β Pic, whose distance data are from the Hipparcos catalog (van Leeuwen 2007), the distance estimates are taken from Bailer-Jones et al. (2021) using their geometric approach that is based only on the Gaia EDR3 parallaxes. Group membership information is based on the BANYAN Σ model (Gagné et al. 2018) in most cases, while for HD 48370 and NO Lup are from Torres et al. (2008) and Lovell et al. (2021a), respectively. For stars known to be members of stellar associations, we have adopted the ages of the specific groups. The estimated ages of the TWA (TW Hya), 118TAU (118 Tau), US (Upper Scorpius), UCL (Upper Centaurus Lupus), and LCC (Lower Centaurus Crux) groups are from Gagné et al. (2018). For the BPMG (β Pic moving group), THA (Tucana-Horologium association), CAR (Carina), and COL (Columba) moving groups, the ages are taken from the recent work of Gratton et al. (2024). For HD 32297 and HD 141569 we have used their individual age estimates from Kalas (2005) and Wichittanakom et al. (2020), respectively. In the case of RZ Psc, the quoted age combines the results of Punzi et al. (2018) and Potravnov et al. (2019). The ^{12}CO line luminosities ($L_{^{12}\text{CO}}$) given in the 12th column refer to the J=2–1 rotational transition, except for NO Lup where the 3–2 line luminosity is quoted. The last column shows which label we use to mark the given object in Figs. 7–9. References to the stellar and disk parameters presented are summarized in the 14th column of the table.

References. 1. Ballering et al. (2013) - 2. Cataldi et al. (2023) - 3. Chen et al. (2014) - 4. Dent et al. (2014) - 5. Di Folco et al. (2020) - 6. Hales et al. (2022) - 7. Hardy et al. (2015) - 8. Hom et al. (2020) - 9. Kennedy et al. (2018) - 10. Kral et al. (2020b) - 11. Lacour et al. (2021) - 12. Lieman-Sifry et al. (2016) - 13. Lisse et al. (2017) - 14. Lovell et al. (2021b) - 15. Lovell et al. (2021a) - 16. MacGregor et al. (2018) - 17. MacGregor et al. (2019) - 18. Marino et al. (2016) - 19. Marino et al. (2020a) - 20. Marshall et al. (2021) - 21. Matrà et al. (2017a) - 22. Matrà et al. (2025) - 23. Meeus et al. (2012) - 24. Moór et al. (2011b) - 25. Moór et al. (2011a) - 26. Moór et al. (2015b) - 27. Moór et al. (2015a) - 28. Moór et al. (2016) - 29. Moór et al. (2017) - 30. Moór et al. (2019) - 31. Moór et al. (2020) - 32. Moór et al. (2021) - 33. Olofsson et al. (2013) - 34. Paegert et al. (2021) - 35. Pawellek et al. (2021) - 36. Pearce et al. (2022) - 37. Rebollido et al. (2022) - 38. Rhee et al. (2007) - 39. Riviere-Marichalar et al. (2014) - 40. Rodet et al. (2017) - 41. Schneiderman et al. (2021) - 42. Su et al. (2020) - 43. Su et al. (2023) - 44. Vican et al. (2016) - 45. Wichittanakom et al. (2020) - 46. Xiaoming et al. (in prep.) - 47. Zwintz et al. (2019) - 48. This work.